A COMPUTATIONAL MODEL FOR PYROLYSIS, HEAT TRANSFER, AND COMBUSTION IN A FIXED-BED WASTE GASIFIER

by

Chung-Yin Tsai

A dissertation submitted in partial fulfillment
of the requirements for the degree of
Doctor of Philosophy
(Mechanical Engineering)
in The University of Michigan
2011

Doctoral Committee:
Associate Professor Hong G. Im, Chair
Professor Arvind Atreya
Professor James F. Driscoll
Associate Professor Angela Violi
Professor Taig-Young Kim, Korean Polytechnic University

To my family and my grandparents

Acknowledgments

First of all, I would like to express my deepest gratitude to my advisor Dr. Hong G. Im for his constant inputs and involvements in my research. It is his insightful advises professional trainings that develop who I am today. I especially appreciate his patience and warm encouragements when I was depressed on the way toward my degree. His friendly personality creates an open atmosphere for all kinds of discussions, yet his consistent high standard and enthusiasm toward research has demonstrated me what the best attitude toward science should be.

I would like to thank my committee members: Prof. Taig-Young Kim, Prof. James Driscoll, Prof. Arvind Atreya and Prof. Angela Violi for providing me valuable inputs. Special thanks to my co-advisor Prof. Taig-Young Kim for his advice on numerical techniques. I appreciate his patience and kindness which help me resolve a lot of numerical issues.

I owe my loving thanks to my family – my parents and my younger brother. Your warm welcome each time I go back home always makes me feel fully charged and ready for further challenges. Although my parents still don't know quite well where Ann Arbor is and Ann Arbor actually is not a harbor city, they always give me continuous support and warm encouragements. It is all you that makes me become a mature and independent person today. I also would like to thank my fellow Taiwanese friends from Ann Arbor Taiwanese Association: Julia Liu, Chiping Liu, Sue Huang, Bernie Huang

and James Chen. I appreciate that they have taken care of me as a family member throughout these years.

I am thankful to my colleagues: Brian Peterson, Jason Martz, Paul Arias and Saurabh Gupta, Won-Chan Park, former lab members: Drs. Chun Sang Yoo, Songtao Tang, Jingjing Li, Gaurav Bansal, Mohit Sood and Vinit Shah for their advice and encouragements on my research. I am also thankful to my former students Louise Lu, Yuntao Chen, John Woolsey for their dedication on my research. Special thanks are due to my friends in Michigan Taiwanese Student Association: Drs. Hsien-Chang Lin, Shaun Ho, Ting-Wu Chuang, Pei-Hsin Wu, Hsing-Fang Hsieh, Isaac Chu, Hui-Chun Chang, Ming-Hsin Li, Wei-Chung Chiang, Bruce Tai, Hui-Wen Chuang, Chuang-Chung Hu, Wan-Chin Lee, Eugengen Wu, Yu-Han Huang, Jing-Yu Lee, Huai-Ning Chang and Claire Meng Yang. It is you that makes my life here splendid.

Table of Contents

List of Figures

List of Tables

List of Appendices

List of Abbreviations

A	Pre-exponential constant (s^{-1})
A_i	Heterogeneous interfacial area in i direction (m^2)
B_j	Hydrodynamic dispersion in j direction (kg / m^2-s)
C_F	Forchheimer coefficient
C_{stoc}	Stoichiometric ratio
D	Characteristic diameter (m)
D_{eff}	Mass diffusion coefficient
E_u	Activation energy (J / mol-K)
$\dot{f}$	Characteristic feeding velocity (m^3 / m^2 -s)
h	Convection coefficient (W / m^2)
h_{fg}	Latent heat (J / kg)
J	Jacobian
k	Turbulent kinetic energy (m^2 / s^2)
K	Permeability of the porous matrix (m^2)
K_e	Evaporation constant (m^2 / s)

$\dot{m}_F$	Mass flow rate of evaporated fuel (kg / s)
L	Half width of the gasifier chamber (m)
M	Mixture molecular weight
N	Number of characteristic spheres
p	Pressure (Pa / m^2)
q	Heat flux (J / m^2 -s)
R	Tunnel radius (m)
R_u	Universal gas constant (8.314 J / mol-K)
S	Source term
t	Time (s)
T	Temperature (K)
u	Velocity (m / s)
u_D	Darcy velocity (m / s)
U	Contravariant velocity
V	Volume (m^3)
V_{ref}	Characteristic volume
v_d	Characteristic feeding velocity (m / s)
x, y, z	Cartesian coordinates (m)

Y_i	i specie mass fraction

Greek Letters

δ	Kronecker delta function
ε	Turbulence kinetic energy dissipation rate (m^2 / s^3)
κ	Index of tunnel effect
λ	Thermal conductivity (W / m-K)
μ	Viscosity (kg / m-s)
ξ, η, ζ	Generalized coordinates
ρ	Density (kg / m^3)
φ	Porosity
ψ	Nondimensional feeding rate
$\acute{\omega}_{pyro}$	Pyrolysis rate (kg / m^3-s)
Ω	Degree of charring

Superscript

^	Properties in generalized coordinate

Subscript

$\alpha, \beta, \alpha\beta$	α phase, β phase, interface between α and β
φ	Equation index

i, j, k, l, m, n	Tensor notation index
eff	Effective
g	Gas phase
l	Laminar
o	Reference state (1atm, 298 K)
p	Product
pyro	Pyrolysis
s	Solid phase, surface
t	Turbulence

Nondimensional Numbers

Da	Darcy number; Domkohler number
Pr	Prandtl number
Pr_t	Turbulent Prandtl number
Re	Reynolds number
Re_t	Turbulent Reynolds number
Le	Lewis number
Sc	Schmidt number
Sc_t	Turbulent Schmidt number

Abstract

The overarching goal of the study presented in this dissertation is to develop a predictive computational model that can describe the detailed chemical and physical processes associated with pyrolysis, heat transfer and combustion for solid waste in a fixed bed gasifier. The work is applicable to optimization and prediction of the synthetic gas composition of solid waste gasifier operations. The dissertation is comprised of two main parts.

In the first part, a predictive three-dimensional model for municipal solid waste gasification process is developed. The multiphase flow field is described by a porous flow model using the SIMPLE algorithm with momentum interpolation. The governing equations are transformed into a generalized coordinate system to be applicable to realistic reactor geometry. A simplified global reaction mechanism is adapted for the gas-phase chemical reactions inside the gasifier. The pyrolysis process is described by a phenomenological Lagrangian pyrolysis model to determine the local porosity distribution and the corresponding pyrolysis rate of the waste material. The developed modeling approach allows a simplified description of the multiphase phenomena by using a single gas-phase governing equations in a porous medium. Polymethyl methacrylate (PMMA) is used as a test waste material for the simulation. Combustion behavior corresponding to the waste porosity, inlet conditions is studied for a range of operating conditions. Computational results show three-dimensional distribution of the flow field, temperature, species concentration, porosity and the morphology

of the waste stack under different parametric conditions. The effects of the inlet temperature and the feeding rate on the waste stack shape are studied. The results demonstrate that the model can properly capture the essential physical and chemical processes in the gasifier and thus can be used as a predictive simulation tool.

In the second part, the Lagrangian pyrolysis model is extended to consider a multiple characteristic diameter (MCD) pyrolysis submodel in order to independently determine the rate of the local devolatilization, drying and charring processes associated with realistic biomass fuels. The porosity distribution is determined by introducing the local characteristic diameter of the virtual solid spheres representing the biomass fuel. Global homogeneous (gas/gas) and heterogeneous (solid/gas) reactions were adapted for the chemical reactions inside the gasifier. Synthetic gas compositions from model prediction are validated experiments conducted by Korean Institute of Energy Research (KIER) with good agreement. Model predictions are also compared with the results calculated by the equilibrium model in order to demonstrate that the proposed model improves the predictive capability of the complex nonequilibrium processes inside the gasifier.

Chapter 1
Introduction

1.1 Background

About 97% of all transportation energy in the United States is derived from fossil fuels. Nonrenewable petroleum, and energy for transportation consumes 63% of all oil (Davis, 1998) and the combustion of fossil fuels accounts for two-thirds of global anthropogenic CO_2 emissions (Mohan *et al.*, 2006). Due to the concerns on the global warming and the increasing fuel price, new technologies in alternative energy has been emerging as active research subjects during the past decade. As shown in Figure 1-1a, renewable energy contributed 7% the total U.S. energy consumption in 2008 and, among the renewable energy resources, biomass alone contributed more than half of the total renewable energy consumption. Biomass provided nearly 3.62 quadrillion BTUs (quads) to the nation's energy supply in 2008, approximately 3.6% of total U.S. energy consumption (U.S. Energy Information Administration, 2010). Energy derived from biomass contributed 52% of the total renewable energy consumption and it even surpassed hydropower as an energy source in recent years. Among the total biomass energy consumption in 2008, 70.9% of biomass energy is provided by (1) wood and refuse-derived fuel (RDF) (53.1%) and (2) waste (17.8%) (U.S. Energy Information Administration, 2010). The biological potential of the forestlands of the United States is 29.1-34.6 billion cubic feet per year

(Spurr, 1976). For example, the commercial forest lands in east Texas provide 5 million tons of logging residues annually (Soltes, 1978). These data suggest that there is a tremendous potential to utilize gasification technology as a viable alternative energy source. As shown in Figure 1-1b, the demands of biomass energy continue to increase in recent years, thus clearly indicating that biomass utilization technologies are in high demand.

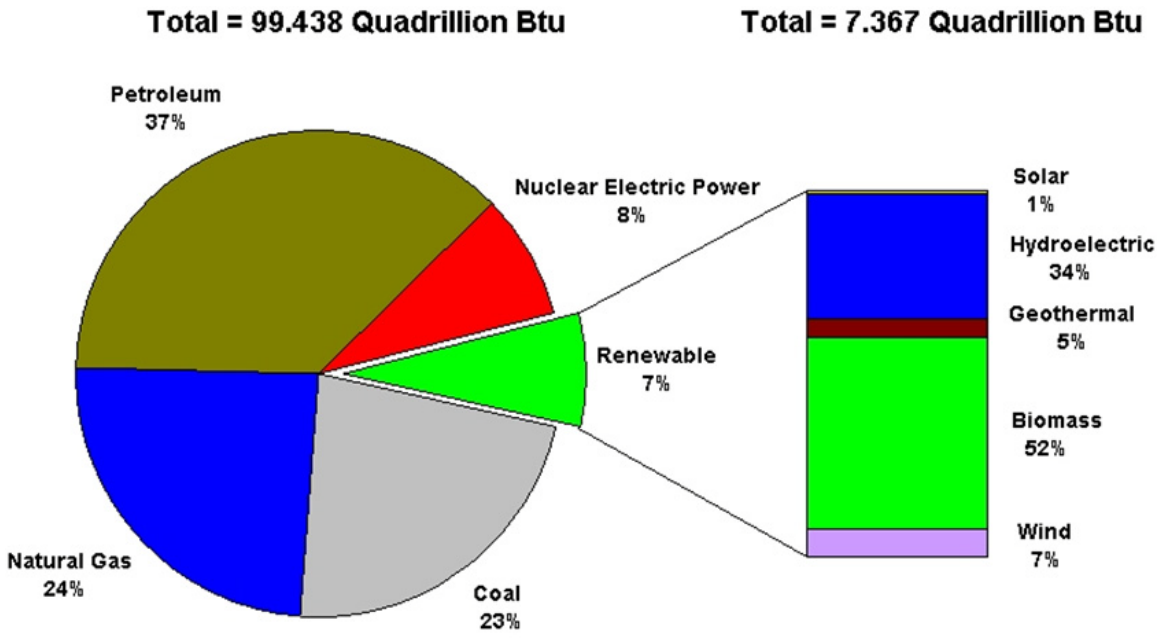

Figure 1-1a: 2008 USA energy consumption (U.S. Energy Information Administration, 2010).

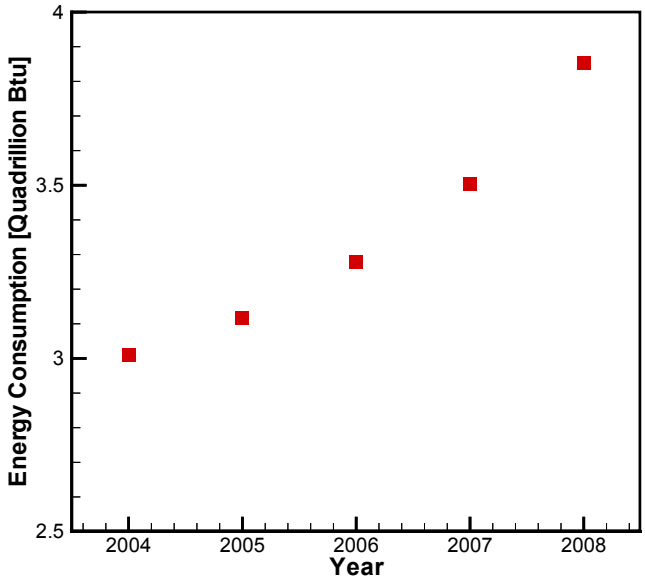

Figure 1-1b: USA biomass energy consumption in recent years (U.S. Energy Information Administration, 2010).

There are four major approaches to utilize biomass energy including direct combustion, co-firing, anaerobic digestion and gasification. Direct combustion has been applied for thousands of years that, like camp fire, biomass is burned directly. However, this is not a preferred approach because most of the energy is wasted in the air and there are potential pollution problems. For co-firing, which biomass is blended with coal, it still relies on nonrenewable fossil fuel. Anaerobic digestion, which is a relatively new technology, generates methane by algae. However, this technology is expensive due to the fact that it requires higher degree of operation and monitoring. Gasification, which biomass is burned in the presence of carefully controlled amount of oxygen, produces synthetic gas as gaseous fuel and it can also be further processed to make biodiesel or other chemical products. As a consequence, gasification has been the major approach to utilize biomass energy.

Unlike combustion, the gasification process involves the amount of oxidizer much less than the stoichiometric value. The system thus generates unsaturated products named synthetic gas (syn-gas), consisting primarily of CO, H_2 and CH_4, serving as gaseous energy carriers, allowing extraction of energy as needed via cleaner combustion. The syn-gas can also be burned in an internal combustion engine, a gas turbine or a reciprocating engine, and can be easily applied in combined cycles for power generation. In the past decades, different gasification technologies have been extensively studied and developed. Compared to incineration of waste matters, gasification is also environment-friendly and economically beneficial. Through gasification, fuel generation and waste management can be achieved simultaneously and it has been considered a high profit new energy approach.

Early applications on gasification can be traced back to the end of the eighteenth century when pyrolysis was used to produce gas from coal (Moore, 2002). Early research therefore had focused on solving problems of tar and byproducts in the gas, especially in the case of gasifications of lower quality fuels such as lignite and peat (Kutzbach, 1905). It was also found that the amount of water should be regulated to yield the highest percentage of desired synthetic gas through gasification (Voigt, 1909). The earliest attempts to gasify plant materials and solid wastes both happened in early 1920s. Gasification of tanbark waste, hemp stalks, cocoa-bean shells, olive-seed hulls and hulls of legumes were conducted and their corresponding analysis and thermal values of the resulting gas were studied (The Engineering Index, 1922). Wolff (1923) performed the first tests on gasification of refuse such as dust and garbage.

Gasification had been extensively studied from 1940 to early 1950 due to the shortage of gasoline caused by World War II. Engineers focused on converting synthetic gas into fuel suitable for internal combustion engines rather than on the gasification process itself. Chemical reactions that occur during gasification were studied and mathematical equations to calculate basic quantities for gasification reactions involving air and fuel with volatiles were proposed (Traustel, 1944). As an attempt to utilized pulverized coal as a fuel for gas producers, Lewis *et al.* (1949) performed experiments on the reaction of carbon powder with steam. During 1950s and 1960s, engineers experimented with new kinds of fuel bed in coal gas producers, such as fluidized and moving beds. There was also continued interest in understanding gasification chemistry. During this time, the primary goal of gasification was the production of synthetic hydrocarbon fuels from coal, and little attention was given to gasification of plant matter (Goring *et al.*, 1952; Shires, 1958; Stern *et al.*, 1965). Computer simulations started to be applied in the prediction of gas properties for different operation conditions of two-stage high-pressure coal gasification process (Donath *et al.*, 1967).

It was not until late 1970s that biomass gasification became an active research subject. Various experimental studies were conducted to identify the compositions of the synthetic gas generated from different materials. Basic chemical process and kinetics were also explored. Laboratory reactors were used to pyrolize and gasify bark, straw, peat, wood, and waste, and the composition of the synthetic gas was compared with that from coal gasification in similar reactors. The basic two-step processes for pyrolysis and gasification were first established during this period (Rensfelt et al,

1978), which is still accepted as a standard description of the complex process. Computational models for biomass gasification in a fluid-bed were proposed and the results were compared with experimental data. While good agreement was achieved, it was recognized that more advanced models were needed to describe more complex phenomena such as hydrocarbon cracking, as can now be seen in advanced pyrolysis model in recent studies (Raman *et al.*, 1981; Baker *et al*., 1984). At this time, it was commonly accepted that the biomass pyrolysis involves devolatilization, moisture evaporation, tar generation and charring, while tar subsequently undergoes secondary cracking. These fundamental processes are widely adopted in the development of advanced models.

Recently, more sophisticated mathematical models were developed due to the advances in computing power. A detailed mathematical model of biomass gasification in a fluidized bed based on mass balance with instantaneous oxidation, equilibrium devolatilization was proposed by Bilodeau *et al* (1993). Kinetics of solid-gas reactions and gaseseous phase reactions with heterogeneous mass transfer were also investigated. A chemical equilibriums model in biomass gasification reactions was proposed by Ruggiero *et al*. (1999). It is a simple model which considers the most common species encountered in biomass gasification. However, synthetic gas in gasification processes may not reach equilibrium because heterogeneous char+gas reactions are generally slow. As such, the model prediction may deviate from the experiment data and kinetic based models become the major trend in most of the advanced models proposed later.

1.2 General features of pyrolysis and gasification

Pyrolysis refers to a process to convert solid material into gaseous fuel by heating in an oxygen-deficient environment. Depending on the heating rate, heating temperature, and the residence time for pyrolized species, different products are delivered, such as charcoal, bio-oil, synthetic gas or other specific chemicals. Compared with traditional combustion (incineration), the amount of oxidizer supplied for gasification is less than the stoichiometric value. This fuel-rich condition yields synthetic gas consisting of unsaturated products such as hydrogen, carbon monoxide and methane which can provide extractable energy as a fuel via later combustion (Groveneveld *et al*., 1979; Van Swaaij, 1981; Breakman-Danheux *et al.*, 1998; Na *et al*., 2003; Kwak *et al*., 2006). Through the pyrolysis process, a certain amount of the calorific value contained in the solid material is transformed into gaseous energy carriers with a preferable form of chemical potential energy instead of sensible heat. Furthermore, the gas phase makes it easier to transport, mix and react with oxygen in later combustion.

Figure 1-2 shows a schematic of a typical downdraft gasifier that four overlapping zones are formed: drying, devolatilization, gasification and combustion (Hobbs *et al*. 1992). Solid mass is fed to the top of the gasifier and moves downward under gravity, counter-current to the rising gas stream supplied from the bottom and synthetic gas collected from the top. As the solid materials move downward, the hot gases produced in the gasification and combustion zones exchange energy with the colder solid. Water and subsequently volatile are released when the solid reaches a sufficient high temperature (i.e., pyrolysis temperature). After drying and devolatilization, the char enters the gasification zone where carbon reacts with steam, carbon

dioxide and hydrogen. Endothermic reactions in this section produce unsaturated products such as carbon monoxide and hydrogen. The slightly exothermic reaction of hydrogen with carbon also produces methane. Combustion and gasification reactions occur simultaneously in the combustion zone and the distinction between the two is based on the absence of free oxygen. In the combustion zone, the carbon monoxide, hydrogen and char produced from gasification may react with oxygen and provide necessary heat to sustain the system (Hobbs *et al*., 1992).

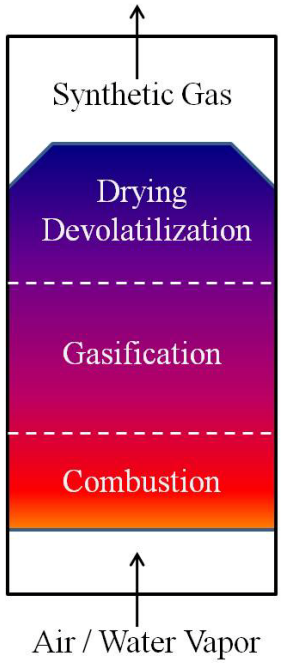

Figure 1-2: Typical atmospheric fixed-bed gasifier (Hobbs *et al.*, 1992).

1.3 Pyrolysis kinetics

Thermogravimetry analysis (TGA) is commonly applied to study the pyrolysis characteristics. It is based on continuous recording of mass changes of a sample of material, as a function of a combination of

temperature with time, as well as pressure and gas composition. To study biomass pyrolysis, TGA was conducted to study filter papers pyrolysis (Broido, 1976). Figure 1-3 shows a diagram for a typical TGA device in which solid samples are placed in the middle of the heating chamber, and carrier inert gas argon are blown into the chamber, carrying the pyrolized gas toward the chemical species analyzer. A typical TGA result is shown in Figure 1-3 in which the reduced weight percent of the material is plotted against the temperature. As the solid sample is heated up, volatiles are released from the solid material and the sample weight is hence reduced. The corresponding temperature T_{p1} is defined as the pyrolysis temperature. Multiple weight loss stages, two in Figure 1-3 for example, suggest there are multiple distinctive pyrolysis temperatures corresponding to distinctive sets of volatiles in the solid material. This multiple stages TGA trajectory is mostly observed in gasification of municipal solid waste consisting of a wide spectrum of waste materials. In most of the biomass pyrolysis, however, not many distinct stages are observed due to the simplicity of their contents (typically a combination of cellulose, hemicelluloses and lignin), resulting in a monotonic TGA trajectory with a unique pyrolysis temperature. The weight of ash and fixed carbon can be determined if the TGA result finally reaches a stable value and no further pyrolysis is observed. This is the common characteristic of charring materials. Otherwise, it is a non-charring material that the TGA trajectory reduces zero. Polymethylmethacrylate (PMMA) is an example of a non-charring material and studies on PMMA gasification will be elaborated in Chapter 2.

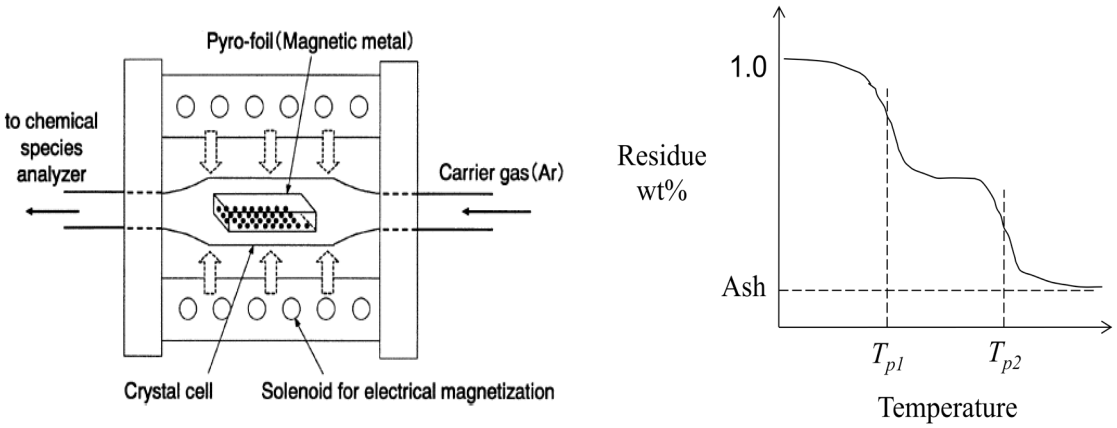

Figure 1-3: A diagram for a standard TGA device (left) and an example of TGA results showing the weight versus temperature (right) (Broido, 1976).

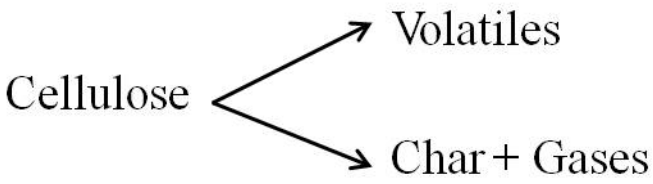

Figure 1-4: Proposed pyrolysis mechanism for cellulose (Broido, 1976).

Figure 1-4 is the Broido-Shafizadeh mechanism (Briodo, 1976) based on the TGA study. The mechanism postulates that cellulose undergoes two parallel processes during pyrolysis: one pathway is the formation of volatile and the other is the formation of char and gases due to secondary tar decomposition. During pyrolysis, the devolatilization rate is in general much faster than the charring rate and this is commonly observed in biomass pyrolysis. Conventional pyrolysis is fundamentally a thermally equilibrium process with a long residence time for the pyrolized species (generally about 5 to 30 minutes) and the pyrolized gases can interact with each other. For fast pyrolysis, it is a high-temperature process in which biomass is rapidly heated

up in the absence of oxygen and removed immediately, resulting in a very short residence time, typically between 0.5 to 5 seconds. After cooling and condensation of the vapors and aerosols, a dark brown mobile liquid is formed with a heating value about half that of conventional fuel oil (Mohan *et al*., 2006).

Current biomass pyrolysis research activities may be grouped into the following four categories (Mohan *et al*., 2006):

1. Biomass characterization
2. Biomass pyrolysis or devolatilization
3. Secondary gas phase reactions
4. Char gasification and combustion

Since biomass is a combination of cellulose, hemicelluloses and lignin, the composition mainly consists of C, H and O. Biomass characterizing can be resolved by TGA and chemical composition analysis. Detailed description of the biomass pyrolysis and devolatilization processes is a challenging research subject due to the complex chemical kinetics associated with the polymer materials. For example, Figure 1-5 shows a partial structure of lignin (Nimz, 1973), clearly demonstrating the complexity of the structure and the difficulties of determining the corresponding pyrolysis mechanism. Detail mechanisms for cellulose pyrolyis cellulose, hemicelluloses and lignin were proposed by Ranzi *et al*. (2008). However, the model is only for cellulose, hemicellulose and lignin monomers and the depolimerization step was assumed to be infinitely fast. This potentially reduces the formation rates of most high carbon number species in tar and the simulation results will only be accurate if the tar decomposition rate is fast. Nevertheless, the

proposed mechanism is too complex and it is not practical for industrial applications. A more conclusive but accurate kinetic model is still preferred for large scale simulations.

Secondary gas phase reactions are homogeneous reactions between pyrolized gases released from the solid materials such as $CO+H_2O$, CH_4+H_2O, CO_2+H_2, or $CO+H_2$. Secondary gas phase reactions become important if the species residence time is long and the gas phase temperature is high, which usually is the case in standard refuse-derived fuel or biomass gasifiers. Char gasification and combustion are heterogeneous reactions occur at the char+gas interface that char is oxidized by O_2, H_2O, CO_2 or H_2.

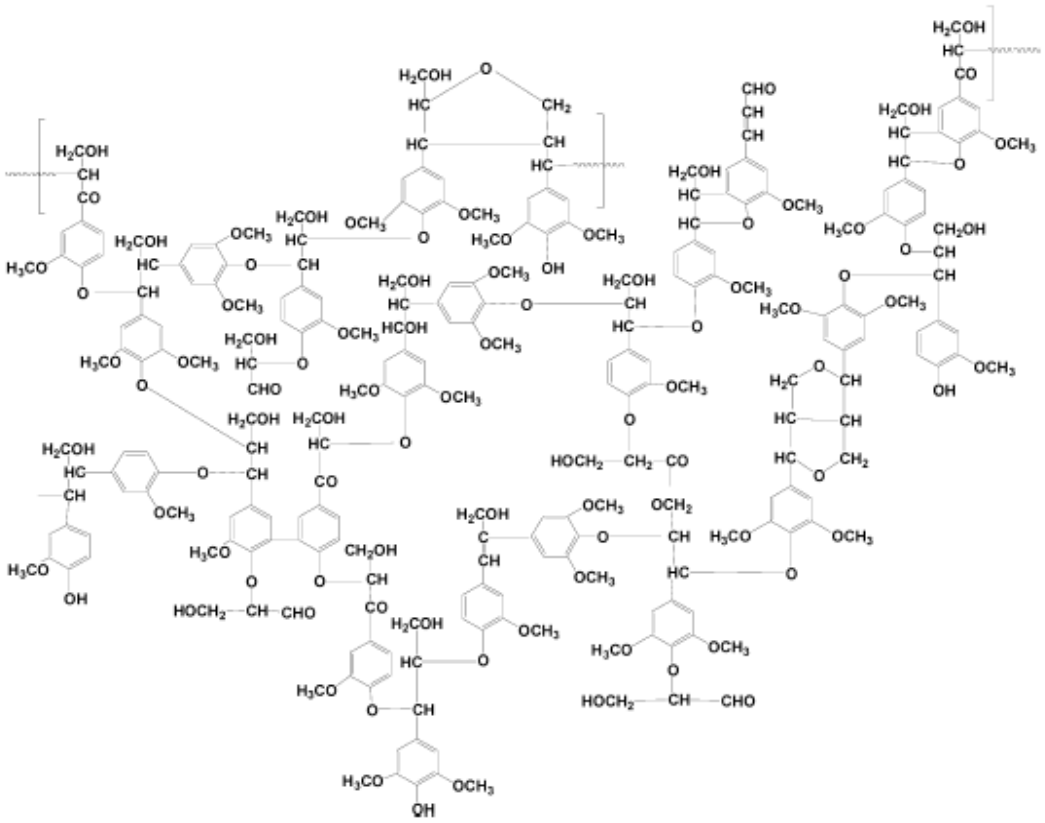

Figure 1-5: Partial structure of lignin (Nimz, 1973).

1.4 Gasification modeling

Gasification modeling involves multiphase flow physics and modeling the interfacial interactions become the most challenging part. The interfacial interactions include drags exerted by the fluid phase, the heat exchange, and the mass conversion from solid phase to gas phase due to pyrolysis. Depending on how the interfacial treatments are modeled, the gasification modeling can commonly be classified into four different methods: zone/cell models (Jennen *et al*., 1999; Shin *et al*., 2000; Hamel *et al*., 2001; Ross *et al*., 2005), equilibrium models (Li *et al*., 2004), Euler-Lagrange models (Rong *et al*., 1999; Kaneko *et al*., 1999; Zhou *et al*., 2004; Limtrakul *et al*., 2004; Gräbner *et al*., 2007; Oevermann *et al*., 2009) and Euler-Euler models (Lathouwers *et al*., 2000; Lathouwers *et al*., 2001; Agrawal *et al*., 2001; O'Brien *et al*., 2003; Xie *et al*., 2004; Yu *et al*., 2007; Xi *et al*., 2008; Deng *et al*., 2008).

The zone/cell models apply energy and mass balance on each cell, in which the fluid motion and chemical reactions are modeled by empirical correlations (Gerber *et al*., 2010). The zone/cell models require least computation effort and they can provide adequate general guidelines for design optimization to gasifier facilities in industrial level. However, limited information on fluid motion and chemistry reduces its potential application on detail investigations of gasification physics.

Equilibrium models assume chemical reactions in the gasifier reach a thermal equilibrium and the modeling of chemical reactions, which usually requires significant amount of computational effort, is greatly simplified. The equilibrium models are good candidates for parametric studies and, like

zone/cell models, they can provide adequate guidelines for design optimization to gasifier facilities. However, heterogeneous char+gas reactions in a gasifier are generally slow processes and the system requires a long time to reach equilibrium. This makes the equilibrium assumption inaccurate because, in some occasions, the synthetic gas and char/slug are removed from the gasifier before they reach equilibrium. These greatly affect the model accuracy on predicting synthetic gas compositions.

Euler-Lagrange models simulate the fluid phase in usual Eulerian schemes by solving the volume-averaged conservation equations. The solid phase, however, is simulated in a Lagrangian scheme as individual particles with independent properties such as diameter, temperature, density and composition. Interactions between solid particles usually are also considered and Euler-Lagrange models are capable for providing most detail information for gasification and it is commonly applied for simulations for bubbling and/or fludized bed gasifiers. However, Euler-Lagrange models are too computationally expensive to be applied in large scale simulations. For example, combustion and gasification of coal in a bubbling fludized bed by an Euler-Lagrange scheme were modeled by Zhou *et al*. (2004), in which there were only 20 reactive particles in the domain with 2000 nonreactive sand particles serve as inert solid, and the simulation was run only for 2 seconds in physical time which is far shorter than the common time scale for gasification operations. The state-of-the-art Euler-Lagrange models are based on discrete element method (DEM) and several simulation packages such as MFIX and Barracuda are based on DEM. Thought Euler-Lagrange models provides high fidelity simulations, to date, models exceeding one million particles are rare. A commercial fluid catalytic cracking (FCC) riser

would require trillions of particles. Thus, although DEM codes may be the most rigorous, but are still limited in industrial applications.

As a compromise between accuracy and computational cost, Euler-Euler models are considered the most common approach to simulate gasification. Similar to the Euler-Lagrange models, Euler-Euler models simulate both fluid and solid phases by volume-averaged conservation equations as interpenetrating continuum with properties varying locally. This, instead of tracking individual particles, provides an advantage that similar numerical algorithm can be applied to solve both phases and the multiphase structure can be easily combined into balance equations with different volume fractions. Euler-Euler models, however, require extensive empirical constants to determine solid phase properties. For example, Euler-Euler models are not able to determine the local porosity variation inherently and the porosity field is usually specified as an input which remains unchanged throughout the calculation.

The approach presented in this thesis combines the advantages of Lagrangian and Eulerian models by describing the solid pyrolysis process using a multiple-characteristic diameter pyrolysis model (MCD) and simulations in industrial-scale gasifiers were conducted. The solid phase is represented as a porous continuum (Eulerian) and the gas phase and solid phase are solved simultaneously throughout the domain. On the other hand, the solid phase is also represented by virtual spheres (i.e., the characteristic spheres) and they were tracked throughout their lifetime in the gasifier (Lagrangian) including devolatilization, drying and charring processes. The characteristic spheres connect necessary solid phase information between Eulerian and Lagrangian schemes and no extensive empirical constants are

required. Solid phase information which traditional Euler-Euler models are not able to resolve including the porosity field can be determined accordingly as a variable. The proposed model has been applied to simulate the steady gasification processes in an industrial scale gasifier which has been developed by Korea Institute of Energy Research (KIER) and the simulation results agree well with the experiment results.

1.5 Outline of the dissertation

The thesis includes a development of a three-dimensional numerical model for a RDF and biomass gasifier, and a validation work with experiments. The thesis is divided into two parts: (1) numerical studies for solid pyrolysis in a fixed-bed RDF gasifier (Tsai *et al*., 2010) and (2) theoretical Investigation of Charring Solid Gasification in a Fixed-Bed Gasifier (Tsai *et al*., 2010).

1.5.1 A Computational Model for Non-Charring Solid Pyrolysis in a Fixed-Bed RDF Gasifier

A predictive three-dimensional model for municipal solid waste gasification process has been developed. The multiphase flow field is described by a porous flow model using the SIMPLE algorithm with momentum interpolation. The governing equations are mapped into generalized coordinate in order to maximize the modeling capability for arbitrary geometries. A one-step global reaction was adapted for the chemical reactions inside the gasifier. The pyrolysis process is described by a nonlinear Lagrangian pyrolysis model to determine the local porosity profile

as well as the corresponding pyrolysis rate of the waste material. This generalized method simplifies the multiphase governing equations into gas phase equations. Polymethyl methacrylate (PMMA) was used as a test waste material for the simulation. Combustion behavior corresponding to the waste porosity, inlet conditions is studied for a range of operating conditions. Computational results produced three-dimensional distribution of the flow field, temperature, species concentration, porosity and the morphology of the waste stack under different operation conditions. The effects of the inlet temperature and the feeding rate on the waste stack shape are studied. The results demonstrated that the model can properly capture the essential physical and chemical processes in the gasifier and thus can be used as a predictive simulation tool.

1.5.2 Theoretical Investigation of Charring Solid Gasification in a Fixed-Bed Gasifier

The Lagrangian pyrolysis submodel has been extended into a multiple-characteristic diameter (MCD) pyrolysis submodel which can be applied to determine the local devolatilization rate, drying rate and charring rate due to biomass pyrolysis has been proposed. Local porosity field are simultaneously determined by introducing the local characteristic diameters of the virtual solid spheres representing the solid wood. One-step homogeneous (gas+gas) and heterogeneous (solid+gas) reactions were adapted for the chemical reactions inside the gasifier. Synthetic gas compositions from model prediction are further compared with experiments conducted by Korean Institute of Energy Research (KIER) and good

agreements are achieved. Model predictions are also compared with results calculated by equilibrium model (EQUIL) and the proposed model shows better capability as a predictive model.

Chapter 2

A Computational Model for Non-Charring Solid Pyrolysis in a Fixed-Bed RDF Gasifier

In this chapter, a steady three-dimensional computational model is developed to simulate the pyrolysis, combustion and heat transfer phenomena in a refuse-derived fuel (RDF) gasifier, allowing realistic description of the gasification physics inside a fixed-bed RDF gasifier. A Lagrangian pyrolysis submodel which can be applied to determine the local pyrolysis rate and porosity field by introducing the local characteristic diameter of the waste solid sphere is proposed. The complex two-phase flow model based on porous medium representation of the solid stack is solved by SIMPLE algorithm with momentum interpolation. A one-step global reaction was adapted for the chemical reactions inside the gasifier.

Computational results produced three-dimensional distribution of the flow field, temperature, species concentration, porosity and the morphology of the waste stack under different operation conditions. Parametric studies are also conducted to assess the effects of the inlet temperature and the feeding rate on the waste stack shape, which future can be applied to optimize operating conditions to achieve an even stack surface minimal the local oxidation (tunneling effect) in the waste stack. The results demonstrated that the model can properly capture the essential physical and chemical processes in the

gasifier and reproduce correct physical and chemical behavior inside the gasifier with adequate computational efficiency and accuracy. Thus the model can be used as a predictive simulation tool for industrial gasifier designs.

2.1 Introduction

The model development was initially motivated by the complementary experimental investigation led by Korea Institute of Energy Research (KIER) (Na *et al*., 2003) in the development and testing of pilot plant for commercial application. During the development of the prototype gasifier, a number of technical challenges were identified, such as highly localized oxidation (tunneling) due to the lack of oxidizer transport within the solid stack. Tackling these issues solely based on trial-and-error tests is expensive and time-consuming. Therefore, there is a strong need to develop high-fidelity computational simulation tool that can predict reaction and transport characteristics inside the gasifier. The present study summarizes our first attempt at a comprehensive computational fluid dynamics (CFD) model for a waste gasifier.

Accurate modeling of a waste gasification process is challenging due to the complexities associated with multi-phase fluid dynamics, homogeneous and heterogeneous chemical reactions of pyrolysis and combustion. Previous studies attempted to simulate the gas-phase and solid phase individually, which requires unnecessarily large computational cost considering that the primary interest of the present study is in the gas-phase flow characteristics. Therefore, a predictive simulation tool has been developed based on the

SIMPLE algorithm and a single-equation porous media model for solid phase representation. The proposed model features a phenomenological pyrolysis model based on the vaporization of representative lumped solid masses with a characteristic diameter. The developed model is implemented into the CFD model and test simulations were conducted to provide qualitiative trends in the basic gasifier performance metrics such as the temperature, concentration, and porosity distribution, waste stack morphology and height, and the overall gasifier yield. Details of the fluid dynamic, pyrolysis, and combustion models are described in the following.

2.2 Mathematical Formulation

Consider a representative volume V in a porous medium consisting of an α-phase and a β-phase, i.e.,

$$V = V_\alpha + V_\beta \tag{2-1}$$

If W is a quantity associated with the α-phase, an intrinsic phase average of W, which denoted as, $\langle W \rangle_\alpha$, is defined as (Whitaker *et al.*, 1967):

$$\langle W \rangle_\alpha = \frac{1}{V_\alpha} \int_{V_\alpha} W_\alpha dV \tag{2-2}$$

The relation on the volume average of a spatial derivative to the spatial derivative of a volume average is shown as

$$\begin{aligned} \frac{1}{V} \int_{V_\alpha} \frac{\partial W_\alpha}{\partial x_i} dV &= \frac{\partial}{\partial x_i} \left(\frac{1}{V} \int_{V_\alpha} W_\alpha dV \right) + \frac{1}{V} \int_{A_{\alpha\beta}} W_\alpha dA_i \\ &= \frac{\partial}{\partial x_i} \left(\varphi_\alpha \langle W \rangle_\alpha \right) + \frac{1}{V} \int_{A_{\alpha\beta}} W_\alpha dA_i \end{aligned} \tag{2-3}$$

where $A_{\alpha\beta}$ is the interface area between α-phase and a β-phase in V, dA_i is the infinitesimal area in normal to i-direction, and $\varphi_\alpha = V_\alpha / V$ is the volume fraction α-phase in V. W_α can be a scalar or a vector variable. This equation accounts that the volume average of a spatial derivative is equal to sum of the spatial derivative of a volume average and the volume average of area integral at the $\alpha\beta$ phase interface.

To derive the macroscopic conservation equations from the microscopic equations, the following relations for the second order gradient are also required.

$$\frac{1}{V}\int_{V_\alpha}\frac{\partial}{\partial x_i}\left(\gamma\frac{\partial W_\alpha}{\partial x_j}\right)dV = \frac{\partial}{\partial x_i}\left[\gamma\frac{\partial}{\partial x_j}\left(\varphi_\alpha\langle W\rangle_\alpha\right)+\frac{\gamma}{V}\int_{A_{\alpha\beta}}W_\alpha dA_j\right]+\frac{1}{V}\int_{A_{\alpha\beta}}\gamma\frac{\partial W_\alpha}{\partial x_j}dA_i \qquad (2\text{-}4a)$$

Expand the first term on RHS of (4a) yields

$$\begin{aligned}\frac{1}{V}\int_{V_\alpha}\frac{\partial}{\partial x_i}\left(\gamma\frac{\partial W_\alpha}{\partial x_j}\right)dV = &\frac{\partial}{\partial x_i}\left(\gamma\varphi_\alpha\frac{\partial\langle W\rangle_\alpha}{\partial x_j}\right)+\frac{\partial}{\partial x_i}\left(\gamma\langle W\rangle_\alpha\frac{\partial\varphi_\alpha}{\partial x_j}\right)\\ &+\frac{\partial}{\partial x_i}\left(\frac{\gamma}{V}\int_{A_{\alpha\beta}}W_\alpha dA_j\right)+\frac{1}{V}\int_{A_{\alpha\beta}}\gamma\frac{\partial W_\alpha}{\partial x_j}dA_i\end{aligned} \qquad (2\text{-}4b)$$

From (2-3), by setting $W = 1$, the spatial gradient of the volume fraction can be obtained as

$$0 = \frac{\partial\varphi_\alpha}{\partial x_i}+\frac{1}{V}\int_{A_{\alpha\beta}}dA_i \qquad (2\text{-}5)$$

Consequently, the microscopic variable can be decomposed with the volume-averaged and spatial dispersion terms as

$$W_\alpha = \langle W\rangle_\alpha + W'_\alpha \qquad (2\text{-}6)$$

Substituting (2-5) and (2-6) into (2-4b) yields

$$\frac{1}{V}\int_{V_\alpha}\frac{\partial}{\partial x_i}\left(\gamma\frac{\partial W_\alpha}{\partial x_j}\right)dV=\frac{\partial}{\partial x_i}\left(\gamma\varphi_\alpha\frac{\partial\langle W\rangle_\alpha}{\partial x_j}\right)+\frac{\partial}{\partial x_i}\left(\frac{\gamma}{V}\int_{A_{\alpha\beta}}W'_\alpha dA_j\right)+\frac{1}{V}\int_{A_{\alpha\beta}}\gamma\frac{\partial W_\alpha}{\partial x_j}dA_i \qquad (2\text{-}7)$$

Similar to W_α, given Y_α as another scalar or vector, the volume-averaged product of W_α and Y_α is determined by

$$\langle W_\alpha Y_\alpha\rangle=\left\langle\left(\langle W\rangle_\alpha+W'_\alpha\right)\left(\langle Y\rangle_\alpha+Y'_\alpha\right)\right\rangle=\langle W\rangle_\alpha\langle Y\rangle_\alpha+\langle W'_\alpha Y'_\alpha\rangle \qquad (2\text{-}8)$$

(2-4a), (2-7) and (2-8) are relations used to derived the following volume-averaged governing equations

2.2.1 Macroscopic steady gas phase continuity equation in a porous media

Microscopic steady continuity equation for gas phase is given by

$$\frac{\partial}{\partial x_i}(\rho u_i)=0 \qquad (2\text{-}9)$$

Where x_i, ρ and u_i are the spatial variable for the Cartesian coordinate, density and u_i is the intrinsic velocity vector. Apply (2-2) to (2-9) yields

$$\frac{\partial}{\partial x_i}\left(\varphi\langle\rho u_i\rangle\right)+\frac{1}{V}\int_{A_{gs}}(\rho u_i)dA_i=0 \qquad (2\text{-}10)$$

where $\varphi=V_g/V$ is the volume fraction of gas phase, i.e., porosity and $\langle u_k\rangle$ is volume-averaged intrinsic velocity. Note that the subscript g representing gas phase is dropped out for simplification. Assuming that the thermal dispersion effects on the gas density is negligible and therefore the macroscopic density is equal to microscopic density as $\langle\rho\rangle=\rho$. The second

term represented as the mass flow into the gas phase due to solid phase pyrolysis at all solid-gas interfaces. The surface integral can be replaced with the macroscopic rate of pyrolysis per unit volume, $\langle \dot{\omega}_{F,pyro} \rangle$, as

$$\frac{1}{V}\int_{A_{gs}} (\rho u_i)\, dA_i = -\dot{\omega}_{F,pyro} \tag{2-11}$$

In the current study, pyrolized fuel is the only specie generated from pyrolysis hence subscript *F* representing fuel is used. Neglecting the higher order dispersion terms, the macroscopic steady gas phase continuity equations in a porous media is

$$\frac{\partial}{\partial x_i}\left(\varphi\rho\langle u_i\rangle\right) = \langle \dot{\omega}_{F,pyro} \rangle \tag{2-12}$$

2.2.2 Macroscopic steady gas phase momentum equation in a porous media

Microscopic steady momentum equation for the gas phase is given by

$$\frac{\partial}{\partial x_i}\left(\rho u_i u_j\right) = -\frac{\partial p}{\partial x_j} - \frac{2}{3}\frac{\partial}{\partial x_j}\left(\mu\frac{\partial u_k}{\partial x_k}\right) + \frac{\partial}{\partial x_k}\left(\mu\left(\frac{\partial u_j}{\partial x_k} + \frac{\partial u_k}{\partial x_j}\right)\right) \tag{2-13}$$

where p and μ are pressure and viscosity, respectively. Apply (2-2), (2-4a), (2-7) and (2-8) to (2-13) yields

$$\begin{aligned}\frac{\partial}{\partial x_i}\left(\varphi\rho\langle u_i\rangle\langle u_j\rangle\right) &= -\frac{\partial\varphi\langle p\rangle}{\partial x_j} - \frac{2}{3}\frac{\partial}{\partial x_j}\left(\mu\frac{\partial\varphi\langle u_k\rangle}{\partial x_k}\right) \\ &+ \frac{\partial}{\partial x_k}\left[\mu\left(\frac{\partial\varphi\langle u_j\rangle}{\partial x_k} + \frac{\partial\varphi\langle u_k\rangle}{\partial x_j}\right)\right] + \frac{\langle p\rangle}{V}\int_{A_{\alpha\beta}} dA_j - \frac{1}{V}\int_{A_{\alpha\beta}} p dA_j + B_j + C_j\end{aligned} \tag{2-14}$$

where

$$B_j = -\frac{1}{V}\int_{A_{gs}} p dA_j + \frac{1}{V}\int_{A_{gs}} \left[\mu \left(\frac{\partial u_j}{\partial x_k} + \frac{\partial u_k}{\partial x_j} \right) \right] dA_k - \frac{2}{3}\frac{1}{V}\int_{A_{gs}} \left(\mu \frac{\partial u_k}{\partial x_k} \right) dA_j \tag{2-15}$$

$$\begin{aligned} C_j = & -\frac{\partial}{\partial x_i}\left(\varphi\rho \left\langle u_i' u_j' \right\rangle \right) - \frac{1}{V}\int_{A_{gs}} \left(\rho u_i u_j \right) dA_i \\ & + \frac{\partial}{\partial x_k}\left[\frac{\mu}{V}\left(\int_{A_{gs}} u_j dA_k + \int_{A_{gs}} u_k dA_j \right) \right] - \frac{2}{3}\frac{\partial}{\partial x_j}\left[\frac{\mu}{V}\int_{A_{gs}} u_k dA_k \right] \end{aligned} \tag{2-16}$$

The B_j represents hydrodynamic dispersion and it can be expressed as

$$B_j = -\left(\frac{\mu}{K} + \frac{\varphi\rho C_F \sqrt{\langle u_k \rangle \langle u_k \rangle}}{\sqrt{K}} \right) \varphi^2 \langle u_j \rangle \tag{2-17}$$

where $K = \varphi^3 D_s^2 / 150(1-\varphi)^2$ is the permeability and it is correlated with sphere diameter and porosity with the Carman-Kozeny equation. $C_F = 1.75/\sqrt{150}\varphi^{3/2}$ is the dimensionless form-drag number (also called Forchheimer coefficient or inertia factor). D_s is the diameter of the solid particle. When the solid phase and gas phase co-exist, additional drag forces (Darcy's and Forchheimer's drags) caused by the flow blockage within the porous medium must be accounted for (Nield *et al.*, 1998). These effects are represented by vector B_j in the momentum equation. As such, these additional forces only exist when solid phase and gas phase co-exist. The present study assumes that the waste material is an isotropic medium, such that K becomes a scalar instead of a second order tensor.

The first term in C_j represents the higher order hydrodynamic dispersion and it was neglected for the current study. The remaining terms are the additional momentum exchange and shear stress occurred at the solid-gas interface due to pyrolysis. If the pyrolized gas is spread out in an isotropic manner, which is assumed to be true in current study, the net momentum exchange becomes zero and the second term vanishes. The third and fourth

terms are small compared to the macroscopic viscous shear terms and can also be neglected. Therefore, C_j is set to be zero. Neglecting the higher order dispersion terms, the macroscopic steady momentum equations in a porous media is

$$\begin{aligned}\frac{\partial}{\partial x_i}\left(\varphi\rho\langle u_i\rangle\langle u_j\rangle\right) &= -\frac{\partial\varphi\langle p\rangle}{\partial x_j} - \frac{2}{3}\frac{\partial}{\partial x_j}\left(\mu\frac{\partial\varphi\langle u_k\rangle}{\partial x_k}\right) \\ &+ \frac{\partial}{\partial x_k}\left[\mu\left(\frac{\partial\varphi\langle u_j\rangle}{\partial x_k} + \frac{\partial\varphi\langle u_k\rangle}{\partial x_j}\right)\right] - \left(\frac{\mu}{K} + \frac{\varphi\rho C_F\sqrt{\langle u_k\rangle\langle u_k\rangle}}{\sqrt{K}}\right)\varphi^2\langle u_j\rangle\end{aligned} \tag{2-18}$$

2.2.3 Macroscopic steady gas phase energy equation

Microscopic steady energy equation for the gas phase is given by

$$\frac{\partial}{\partial x_i}\left(\rho C_p u_i T\right) = \frac{\partial}{\partial x_i}\left(\lambda\frac{\partial T}{\partial x_i}\right) + \dot{q}''' \tag{2-19}$$

where T, C_p, λ and $\dot{q}'''$ are temperature, constant-pressure heat capacity, thermal conductivity the heat generation due to gas phase chemical reactions. Apply (2-2), (2-4a), (2-7) and (2-8) to (2-19) yields

$$\begin{aligned}\frac{\partial}{\partial x_i}\left(\varphi\rho C_p\langle u_i\rangle\langle T\rangle\right) &= \frac{\partial}{\partial x_i}\left(\varphi\lambda\frac{\partial\langle T\rangle}{\partial x_i}\right) + \varphi\langle\dot{q}'''\rangle \\ &+ \left[\frac{1}{V}\int_{A_{gs}}\left(\lambda\frac{\partial T}{\partial x_i}\right)dA_i - \frac{1}{V}\int_{A_{gs}}\rho C_p u_i T dA_i\right] \\ &+ \left[\frac{\partial}{\partial x_i}\left(\frac{\lambda}{V}\int_{A_{gs}}T' dA_i\right) - \frac{\partial}{\partial x_i}\left(\varphi\rho C_p\langle u_i' T'\rangle\right)\right]\end{aligned} \tag{2-20}$$

The third term of RHS represents the heat transferred from solid to gas phases and can be rewritten with the convection heat transfer.

$$\frac{1}{V}\int_{A_{gs}}\left(\lambda\frac{\partial T}{\partial x_i}\right)dA_i = -\frac{hA_s}{V}(\langle T\rangle - T_s) \tag{21}$$

where h, A_s, V and T_s are macroscopic convection heat transfer coefficient at the solid-gas interface, surface area of the solid-gas interface, characteristic volume and solid phase temperature, respectively.

The forth term of RHS in (2-20) represents the enthalpy released into the gas phase from the solid-gas interface due to pyrolysis. Due to pyrolysis, the pyrolized fuel is released under the pyrolysis temperature, T_{pyro} and thus additional heat is required to heat up the pyrolized fuel to the surrounding temperature, $\langle T\rangle$. Like pyrolysis rate, $\langle\dot{\omega}_{F,pyro}\rangle$, this term vanishes when the surrounding temperature is lower than the critical pyrolysis temperature, T_{pyro}. It therefore can be expressed as

$$-\frac{1}{V}\int_{A_{gs}}\rho C_p u_i T dA_i = \langle\dot{\omega}_{F,pyro}\rangle h_{fg} \tag{2-22}$$

where h_{fg} is the latent heat of pyrolysis.

The last bracket in the RHS of (2-20) represents the thermal dispersion effects and these are neglected in this study.

The final form of the macroscopic energy equation for gas phase is shown as

$$\frac{\partial}{\partial x_i}\left(\varphi\rho C_p\langle u_i\rangle\langle T\rangle\right) = \frac{\partial}{\partial x_i}\left(\varphi\lambda\frac{\partial\langle T\rangle}{\partial x_i}\right) + \varphi\langle\dot{q}'''\rangle - \frac{hA_s}{V}(\langle T\rangle - T_s) + \langle\dot{\omega}_{F,pyro}\rangle h_{fg} \tag{2-23}$$

2.2.4 Macroscopic steady specie equation

Microscopic steady specie equation for specie *m* is

$$\frac{\partial}{\partial x_i}\left(\rho u_i Y_m\right)=\frac{\partial}{\partial x_k}\left(\rho D\frac{\partial Y_m}{\partial x_k}\right)+\dot{\omega}_m''' \tag{2-24}$$

where the Y_m, D and $\dot{\omega}_m'''$ are the mass fraction of specie m, diffusivity and the gas phase reaction rate of specie m. Apply (2-2), (2-4a), (2-7) and (2-8) to (2-24) yields

$$\begin{aligned}&\frac{\partial}{\partial x_i}\left(\varphi\rho\left\langle u_i\right\rangle\left\langle Y_m\right\rangle\right)=\frac{\partial}{\partial x_i}\left(\varphi\rho D\frac{\partial\left\langle Y_m\right\rangle}{\partial x_i}\right)+\varphi\left\langle\dot{\omega}_m'''\right\rangle\\&+\frac{1}{V}\int_{A_{gs}}\left[\left(\rho D\frac{\partial Y_m}{\partial x_i}-\rho u_i Y_m\right)\right]dA_i+\left[\frac{\partial}{\partial x_i}\left(\frac{\rho D}{V}\int_{A_{gs}}Y_m' dA_i\right)-\frac{\partial}{\partial x_i}\left(\varphi\rho\left\langle u_i' Y_m'\right\rangle\right)\right]\end{aligned} \tag{2-25}$$

The third term on RHS is the solid interface boundary condition shown as

$$\frac{1}{V}\int_{A_{gs}}\left[\left(\rho D\frac{\partial Y_m}{\partial x_i}-\rho u_i Y_m\right)\right]dA_i=\frac{1}{V}\int_{A_{gs}}\left(\rho u_{i,m}\right)dA_i \tag{2-26}$$

where $u_{i,m}$ is the gas phase velocity of specie m travels across the solid-gas phase interface due to pyrolysis. (2-26) simply states that, during pyrolysis, the total mass flow rate of specie m traveling across the solid-gas interface is equal to the sum of its convection and diffusion. (2-26) is zero except for m = pyrolized fuel since the pyrolysis gas only consists of fuel. Therefore,

$$\frac{1}{V}\int_{A_{gs}}\left[\left(\rho D\frac{\partial Y_m}{\partial x_i}-\rho u_i Y_m\right)\right]dA_i=\begin{cases}\left\langle\dot{\omega}_{F,pyro}\right\rangle, & m=\textit{fuel}\\ 0, & m=\text{otherwise}\end{cases} \tag{2-27}$$

The fourth and fifth terms in the bracket represent the higher order dispersion effects and they are neglected in current study. Therefore, the final form of the macroscopic steady specie equation for gas phase is shown as

$$\frac{\partial}{\partial x_i}\left(\varphi\rho\langle u_i\rangle\langle Y_m\rangle\right)=\frac{\partial}{\partial x_i}\left(\varphi\rho D\frac{\partial\langle Y_m\rangle}{\partial x_i}\right)+\varphi\langle\dot{\omega}_m'''\rangle+\begin{cases}\langle\dot{\omega}_{F,pyro}\rangle, & m=\text{ fuel}\\ 0, & m=\text{otherwise}\end{cases} \quad (2\text{-}28)$$

The above conservation equations describe the flow field throughout the entire domain within the gasifier. In the present model, the solid stack region is treated as a porous medium, where solid and fluid co-exist. For the region outside the stack, where the pure fluid region is, the porosity is set to 1 and Eqs. (2-12), (2-18) (2-23) and (2-28) degenerate to the conventional gas-phase flow equations. Within the stack, the porosity varies from the initial value (typically 0.7 at the top of the stack) to 1 at the bottom where all the solid waste is completely pyrolyzed. As for the species transport equations (2-28), five reactive species are considered: pyrolyzed fuel, oxygen, carbon dioxide, water and inert. In this study, PMMA ($C_5H_8O_2$) is chosen as a model fuel representing the solid waste because its thermodynamics data are well understood and the pyrolysis does not form charring material. For the gas-phase reaction source terms appearing in Eq. (2-23), a one-step global reaction mechanism for the oxidation of pyrolyzed fuel is used (Amos *et al.*, 1988):

$$C_3H_8O_2+6O_2\rightarrow 5CO_2+4H_2O+\Delta h_F \quad (2\text{-}29)$$

where $\Delta h_F = 2.6\times10^7$ [J/kg] is the lower heating value. The reaction rate is given in the Arrhenius form:

$$\dot{\omega}_F=-A_F Y_F Y_O T^{-2}\exp\left(-\frac{E_F}{R_u T}\right) \quad (2\text{-}30)$$

with $A_F = 1.6\times10^{15}$ [kg·K^2/(m^3·s)] and $E_F = 1.8\times10^8$ [J/kmol]. The reaction source terms for the rest of the species equations are scaled accordingly based on the stoichiometric ratio.

The equation of state for porous and pure gas region is represented as follows:

$$p = \rho\left(\frac{R_u}{M}\right)T \tag{2-31}$$

where R_u is the universal gas constant and M is the molecular weight of the mixture.

By introducing the Darcy velocity, $u_{Di} = \varphi u_i$, governing equations above can be written in the Darcian form as

$$\frac{\partial}{\partial x_i}\left(\rho\left\langle u_{Di}\right\rangle\right) = \left\langle \dot{\omega}_{F,pyro}\right\rangle \tag{2-32}$$

$$\begin{aligned}\frac{\partial}{\partial x_i}\left(\frac{\rho}{\varphi}\left\langle u_{Di}\right\rangle\left\langle u_{Dj}\right\rangle\right) &= -\frac{\partial \varphi\left\langle p\right\rangle}{\partial x_j} - \frac{2}{3}\frac{\partial}{\partial x_j}\left(\mu\frac{\partial\left\langle u_{Dk}\right\rangle}{\partial x_k}\right) \\ &+ \frac{\partial}{\partial x_k}\left[\mu\left(\frac{\partial\left\langle u_{Dj}\right\rangle}{\partial x_k} + \frac{\partial\left\langle u_{Dk}\right\rangle}{\partial x_j}\right)\right] - \varphi\left(\frac{\mu}{K} + \frac{\rho C_F\sqrt{\left\langle u_{Dk}\right\rangle\left\langle u_{Dk}\right\rangle}}{\sqrt{K}}\right)\left\langle u_{Dj}\right\rangle\end{aligned} \tag{2-33}$$

$$\frac{\partial}{\partial x_i}\left(\rho C_p\left\langle u_{Di}\right\rangle\left\langle T\right\rangle\right) = \frac{\partial}{\partial x_i}\left(\varphi\lambda\frac{\partial\left\langle T\right\rangle}{\partial x_i}\right) + \varphi\left\langle \dot{q}'''\right\rangle - \frac{hA_s}{V}\left(\left\langle T\right\rangle - T_s\right) + \left\langle \dot{\omega}_{F,pyro}\right\rangle h_{fg} \tag{2-34}$$

$$\frac{\partial}{\partial x_i}\left(\rho\left\langle u_{Di}\right\rangle\left\langle Y_m\right\rangle\right) = \frac{\partial}{\partial x_i}\left(\varphi\rho D\frac{\partial\left\langle Y_m\right\rangle}{\partial x_i}\right) + \varphi\left\langle \dot{\omega}_m'''\right\rangle + \begin{cases}\left\langle \dot{\omega}_{F,pyro}\right\rangle, & m = fuel \\ 0, & m = \text{otherwise}\end{cases} \tag{2-35}$$

In order to apply the proposed model to a gasifier with an arbitrary geometry, the above steady system was generalized into a generalized coordinate system and solved using the SIMPLE algorithm (Patankar *et al.*, 1980) with pressure-weighted interpolation method (PWIM) (Rhie *et al.*, 1983). Detail derivations are listed in appendix A and B.

2.3 Lagrangian Pyrolysis Model

Modeling the process of the solid stack pyrolysis is one of the key developments in the present study. Here, the stack of solid pellets inside the gasifier is represented by a porous medium at a given porosity. Considering that the pellet size and the heat transfer rate from the gas phase to the solid phase, the time scale for conduction within the solid pellet is much faster than the lifetime of the solid pellet through the pyrolysis process. Therefore, the temperature variation within the individual solid pellets is negligible and the local temperature of the solid stack is assumed to the identical to the gas temperature, provided the gas temperature is lower than the pyrolysis temperature, i.e., $T_s = T_{pyro}$. If the local gas temperature becomes higher, the solid temperature, Ts, is then fixed at T_{pyro} and all the heat transfer from gas phase is used to provide the latent heat for pyrolysis of the solid material. Under these assumptions, the local pyrolysis rate in the solid region is determined based the Lagrangian pyrolysis model as described in the following.

The Lagrangian pyrolysis model starts from recognizing that the waste pellets decreases in size through the pyrolysis process as they move down in the stack. In describing this process, the following simplifying assumptions are made:

1. The waste stack is described by a porous medium, where the local porosity roughly represents the relative size of the individual waste pellets provided from the input feed. Therefore, the average size of the waste pellet at any spatial location is represented by the characteristic

diameter, D, which starts from the initial value at the top stack surface and decreases as the waste pellets sink down to the bottom.

2. The local pyrolysis rate is determined by the heat transfer between the characteristic waste sphere with diameter D and the surrounding gas flow.

Following this model, the initial characteristic diameter, D_0, can be correlated with the given initial porosity, φ_0, of the solid stack by

$$\varphi_0 = 1 - \frac{N\pi}{6V_{ref}} D_0^3 \tag{2-36}$$

where V_{ref} is the volume of the local cell assuming that the spherical pellets are uniformly distributed on the top surface of the stack. N is the number of spheres inside V_{ref}, and N can be computed accordingly by (2-36). In present study, $D_0 = 2$cm which is the standard size of a waste pellet (Na *et al.*, 2003). If the solid temperature increases to T_{pyro}, pyrolysis starts to occur at the rate proportional to the amount of heat transfer rate, given by the relation:

$$\dot{m}_F h_{fg} = hA_s(T - T_{pyro}) \tag{2-37}$$

A_s is the surface area of the solid-gas phase interface and it equals to the surface area of the characteristic waste sphere. Similar to the droplet evaporation problem (Law, 2006), the evaporation constant, K_e, can be determined by the d^2-law:

$$\frac{dD^2}{dt} = -\left(\frac{4\mathrm{Nu}\lambda}{\rho_s h_{fg}}\right)(T - T_{pyro}) = -K_e \tag{2-38}$$

where λ is the conductivity [W/m·K] of the gas, D is the characteristic diameter of the solid pellet, ρ_s and V_s are the density and volume of the solid

pellet, respectively. For spherical particles, the solid-gas interfacial Nusselt number, Nu, can be determined via the following relation (Wakao *et al.*)

$$\mathrm{Nu} = 2 + 1.1\,\mathrm{Re}^{0.6}\,\mathrm{Pr}^{1/3} \tag{2-39}$$

In (2-38), t represents the Lagrangian time following the solid pellet. Assuming that the solid pellets starts from the top of the stack and vertically moves down, the time derivative can be translated into the spatial derivative in the vertical direction by $t = z / v_d$, where $v_d(x,y)$ [$\mathrm{m^3/s \cdot m^2}$] is the *volumetric feeding rate per unit area*, or simply the *characteristic feeding velocity*. In general, the feeding velocity is allowed to vary in x and y direction on the cross-sectional area at the top inlet. Equation (2-38) can then be written as:

$$\frac{dD^2}{dz} = -\frac{K_e}{v_d} \tag{2-40}$$

which allows us to determine the vertical variation in the characteristic diameter by:

$$D^2 = D_0^2 - \frac{1}{v_d}\int_0^z K_e dz \tag{2-41}$$

Considering that the solid sphere is completely pyrolyzed at the bottom of the stack, $D = 0$ at $z = 0$ and $D = D_0$ at $z = H$, where $H(x,y)$ is the local solid stack height, such that

$$D_0^2 = \frac{1}{v_d}\int_0^H K_e dz \tag{2-42}$$

serves as an implicit relation to determine $H(x,y)$ and thereby the morphology of the waste stack. Furthermore, the local pyrolysis rate per unit volume can be determined consequently as

$$\dot{\omega}_{F,pyro} = \frac{\dot{m}_F}{V_{ref}} = \frac{N\pi Nu\lambda}{V_{ref}} D(T - T_{pyro}) \tag{2-43}$$

Assuming a cubic relation between characteristic diameter and porosity, the local porosity can be determined by the local characteristic diameter as

$$\varphi = 1 - \frac{N\pi}{6V_{ref}} D^3 \tag{2-44}$$

In summary, the Lagrangian pyrolysis model determines the characteristic diameter, local porosity, local stack height, and local pyrolysis rate using Eqs. (2-32) - (2-45).

2.4 Computational Configurations

The computational configuration of the preliminary calculations is a rectangular domain as shown in Figure 1. The dimension of the gasifier is 0.2m x 0.2m x 0.4m with 31 x 31 x 171 grid points used respectively. Preheated oxygen at different temperature is supplied from the bottom of the burner and the solid waste material is supplied at different feeding rate from the top. The solid stack is shown in shaded color, with its height *h* compared against the total gasifier height, H_c. The bottom of the stack is located at the inlet. As described in Section 3, the bed morphology is determined as part of the solution process. The fuel generated by the pyrolysis leaves the outlet port with a dimension in 0.1m x 0.1m locating at the center of the top.

The multiphase reacting flow with solid-phase pyrolysis is mathematically modeled and numerically solved in a three-dimensional collocated grid structure under Cartesian coordinates, with a boundary-fitted coordinate

transformation to describe various gasifier geometries. Our previous work (Tsai *et al.*, 2007 and 2008) showed symmetric flow fields when the outlet port was located at the center. Hence the proposed simulations were done in a quarter of the gasifier, indicated by the dash lines in Figure 2-1.

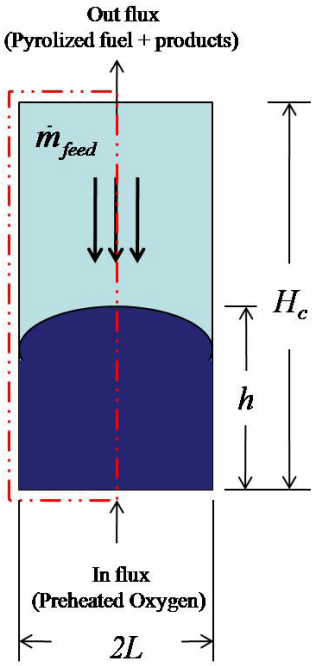

Figure 2-1. Schematic of the computational configuration.

The characteristic feeding velocity in the quarter of the gasifier for the simulation is given in the following Laplace equation and the corresponding boundary conditions:

$$\frac{\partial v_d}{\partial x^2}+\frac{\partial v_d}{\partial y^2}=0$$

$$v_d(x=0,y)=\frac{\gamma A}{\sqrt{2\pi\sigma^2}}\exp\left(-\frac{L^2}{2\sigma^2}\right)$$

$$v_d(x,y=0)=\frac{\gamma A}{\sqrt{2\pi\sigma^2}}\exp\left(-\frac{L^2}{2\sigma^2}\right) \qquad (2\text{-}45)$$

$$v_d(x=L,y)=\frac{\gamma A}{\sqrt{2\pi\sigma^2}}\exp\left(-\frac{(y-L)^2}{2\sigma^2}\right)$$

$$v_d(x,y=L)=\frac{\gamma A}{\sqrt{2\pi\sigma^2}}\exp\left(-\frac{(x-L)^2}{2\sigma^2}\right)$$

where A = 2.12E-5 [m/s], σ/L = 2.5 [1/m], L = 0.1 [m] and γ is a variable used to control the characteristic feeding velocity and it ranges from 0.04 to 1.64 in current study. This two-dimensional boundary-fitted feeding velocity profile which peaks at the center and reduces near the burner wall represents the actual waste material feeding situation. Furthermore, the prescribed distribution profile is practically appropriate in order to prevent excessive stack-up of waste material near the wall whenever there is heat loss at the wall.

A non-dimensional feeding rate is defined as

$$\psi \equiv \frac{\dot{m}_{feed}}{\dot{m}_{inlet}} \qquad (2\text{-}46)$$

where $\dot{m}_{feed}$ is the mass flow rate of the waste material from the top and $\dot{m}_{inlet}$ is the mass flow rate of the oxygen from the inlet. From (2-29), the stoichiometric feeding rate, ψ_{st}, can be determined as 0.091. The flow Reynolds number is defined as

$$Re_{H_c} \equiv \frac{\rho_{ref} V_{inlet} H_c}{\mu_{ref}} \tag{2-47}$$

where subscript *ref* denotes oxygen at reference state, which is at 298K and 1 atm. For all simulations presented in this study, the Reynolds number was set at 332. The initial porosity, φ_0, of the waste material is 0.7 and the pyrolysis temperature, T_{pyro}, sets to be 633 K (Amos *et al.*, 1988). As for the boundary condition at the burner side walls, no-slip boundary conditions as well as the adiabatic wall were imposed.

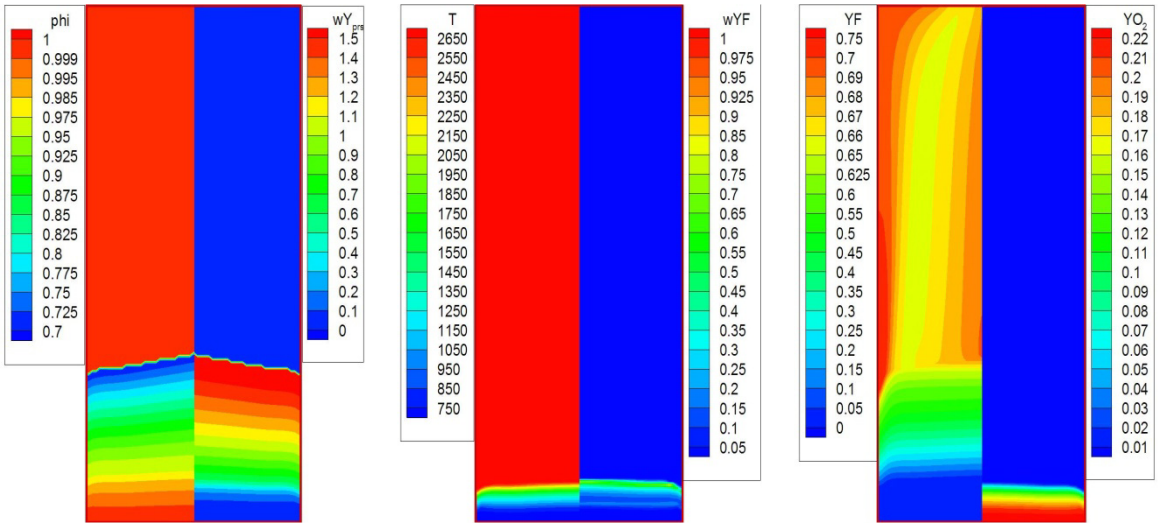

Figure 2-2: Typical solution profiles from a steady state calculation at the inlet temperature of 950K and ψ = 8.07. From left to right: porosity (ϕ), pyrolysis rate, temperature, reaction rate of the fuel, fuel and oxygen mass fractions.

2.5 Results and Discussion

Figure 2-2 shows a steady state solution for a case in which preheated air is supplied from the bottom inlet at 950K at a mass flow rate of 6.16E-4 kg/s. The waste feeding rate ψ = 8.07. The porosity iso-contours (the first column)

shows the morphology of the waste stack which is slightly increased near the centerline due to the higher characteristic feeding velocity. The solid waste pyrolysis rate (the second column) shows that the higher pyrolysis reaction occurs at the top part of the waste stack. This is because the characteristic diameter, which represents the size of the solid waste material, is larger at the top of the stack and decreases as the solid waste approaches the bottom due to pyrolysis. The corresponding temperature and reaction rate profile of the pyrolized fuel is shown in the third and forth columns. The preheated air actuates the solid fuel pyrolysis and generates pyrolyzed fuel (the fifth column) which subsequently reacts with the oxygen (the sixth column) and forms a combustion zone at the bottom part of the stack (the forth column). From column second and column sixth, it shows that this exothermic combustion process consumes all the oxygen which is deficient, shuts down the combustion, and a pure endothermic pyrolysis follows in the stack above the combustion zone. These results demonstrate that the present numerical model can successfully predict the steady state morphology of the waste stack for given parametric conditions.

2.5.1 Parametric studies on inlet temperature and feeding rate

A parametic study was conducted to investigate the effect of different inlet condition on the stack morphology and subsequent gasifier yield. Figure 2-3 show the stack morphology at different inlet temperature at ψ = 8.07. The stack height decreases as the inlet temperature increases due to the higher heat transfer rate from gas phase to solid phase, which leads to a higher pyrolysis rate. Furthermore, the shape of the stack surface varied when the inlet temperature increased. To quantify these properties, two non-

dimensional parameters, *Bed Height* and *Height Variation*, were introduced as following:

$$Bed\ Height \equiv \frac{h_{\max}}{H_c} \tag{2-48}$$

$$Height\ Variation\ = \frac{h_{\max} - h_{\min}}{H_C} \tag{2-49}$$

where $h_{\max}$ and $h_{\min}$ are the maximum minimum values of the height of the solid stack.

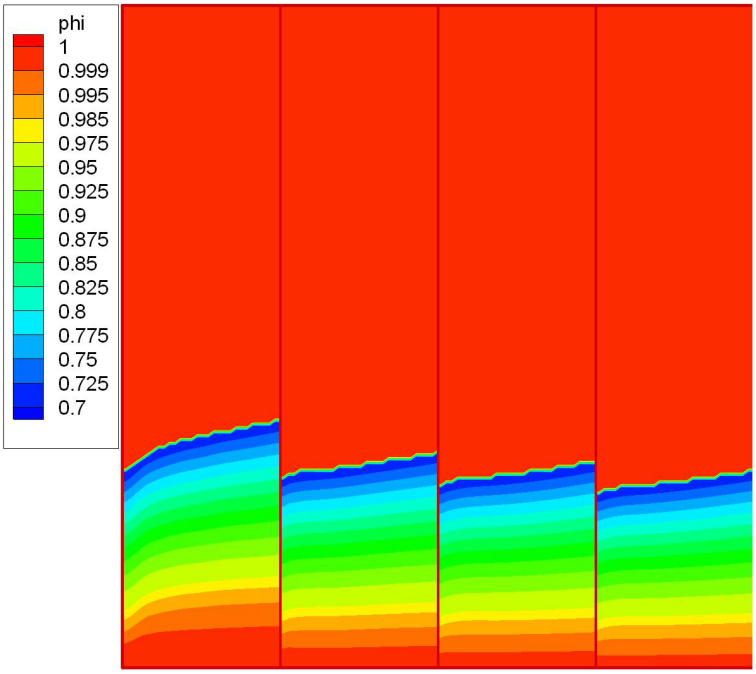

Figure 2-3: Stack morphology in different inlet temperatures at ψ = 8.07. From left to right: 850K, 950K, 1050K and 1150K. There is an overflow in the 750K case hence it is not shown.

Figure 2-4 shows the relation between the bed height and the height variation. It is clearly seen that the bed height decreases monotonically as the inlet temperature increases. The same trend was observed in the height

variation except that the height variation levels off when the inlet temperature above 950K because, as the stack height reduces, the bed surface shape is more dominant by the shape of the reaction zone instead of the fully-developed parabolic velocity profile. A flat flame sheet structure is shown in Figure 2-2 was observed hence the Height Variation for the, For the case with inlet temperature as 750K, the corresponding *Bed Height* and *Height Variation* is 1 and 0, respectively. This is due to the fact that an overflow occurred and no stack surface is formed inside the gasifier.

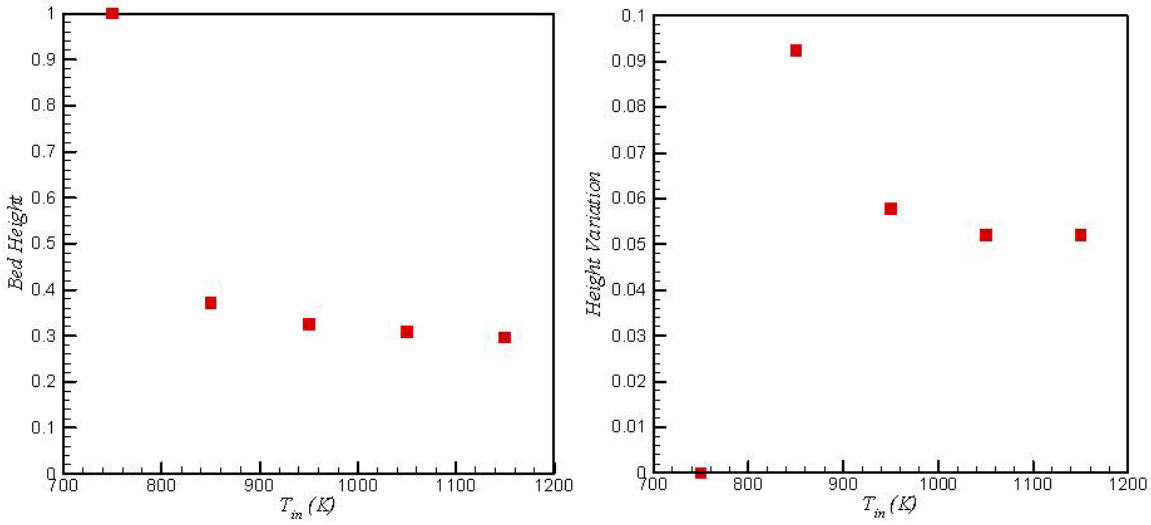

Figure 2-4: Inlet temperature versus bed height (left) and height variation (right) at $\psi = 8.07$.

A variable of practical interest is the overall gasifier yield, which is defined as

$$Yield \equiv \frac{\dot{m}_{fuel,outlet}}{\dot{m}_{feed}} = \frac{\dot{m}_{fuel,outlet}}{\psi \dot{m}_{oxygen,inlet}} \tag{2-50}$$

which is the ratio of the total fuel gas flow rate exiting the gasifier to the fuel supply rate. Figure 2-5 shows the inlet temperature versus yield at $\psi = 8.07$.

It shows that the yield decreases when the inlet temperature is increased. This is due to the fact that, at higher inlet temperature, the reaction rate of the pyrolized fuel is higher which leaves less pyrolized fuel as a yield. Considering Figures 2-4 and 2-5, for ψ = 8.07, it may be suggested that the optimal operation condition for the inlet temperature is at 950K for uniform bed height and higher yield.

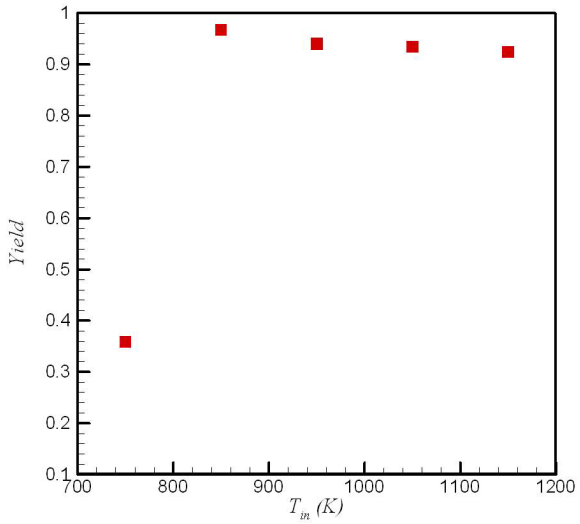

Figure 2-5: Inlet temperature versus yield at ψ = 8.07

As the next parametric study, the effect of the waste feed rate was investigated. Figure 2-6 shows the stack morphology (iso-contours of porosity, φ) as a function of the normalized feed rate, ψ. As the feeding rate increases, the solid stack height increases with a larger height variation. The corresponding *Bed Height* and *Height Variation* are shown in Figure 2-7. Unlike the response to the inlet temperature variation shown in Figure 2-5, both the bed height and the height variation increase monotonically with the feeding rate.

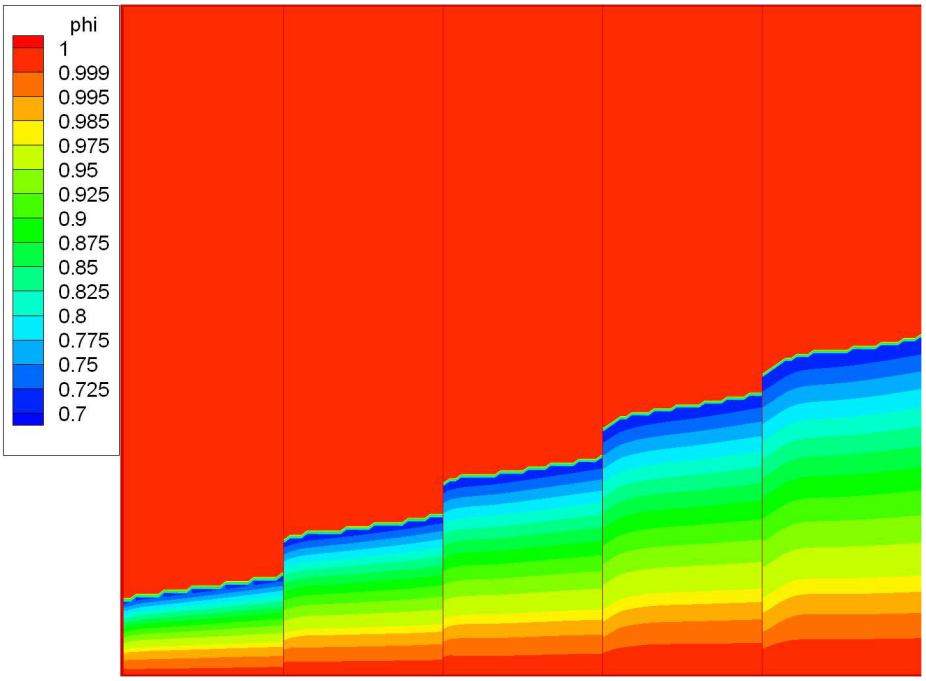

Figure 2-6: Stack morphology in different waste Feeding rate at inlet temperature equals to 950K. From left to right: ψ = 3.03, 5.58, 8.07, 10.70 and 13.20.

Figure 2-8 shows the correlations of feeding rate and the corresponding yield. Again, at very small feeding rate (ψ = 3.03), the solid waste was converted into pyrolyzed fuel immediately. The gaseous fuel further reacts with oxygen and oxygen is fully consumed, thereby leading to the lower yield. Otherwise, the yield increase as the feeding rate increases. This is due to the fact that the more solid waste is supplied to the gasifier, the more pyrolyzed fuel was converted, while the mass flow rate as well as the temperature of the oxygen from the inlet remains unchanged. Hence the consumption of the pyrolyzed fuel is constrained and a higher yield results as the feeding rate increases. Considering the minimized height variation and the yield generation, for the conditions studied here, the optimal operation condition at inlet temperature equals to 950K is ψ = 8.07.

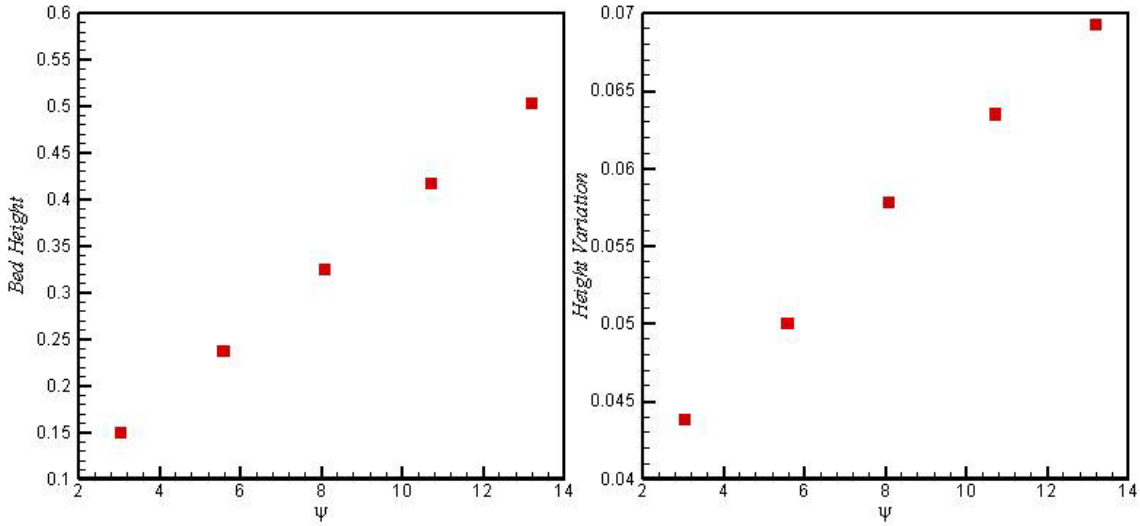

Figure 2-7: Feeding rate versus bed height (left) and height variation (right) at inlet temperature sets to 950K.

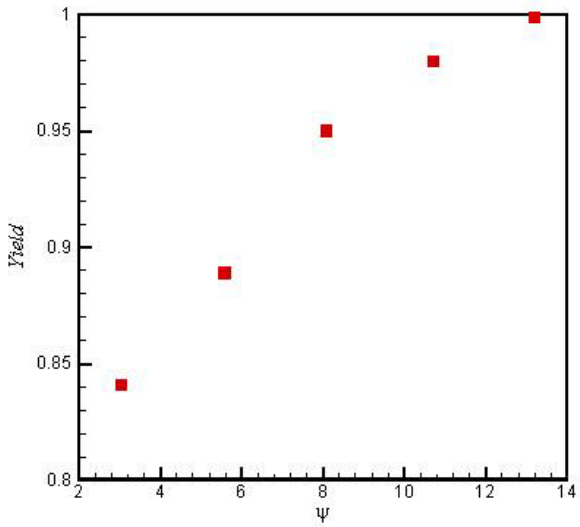

Figure 2-8: Feeding rate versus yield at inlet temperature equals to 950K

2.5.2 Stack surface morphology

The Gaussian feeding rate profile was introduced in (2-45) and Figure 2-9 shows the feeding rate profile showing that the feeding rate is higher at the center of the gasifier.

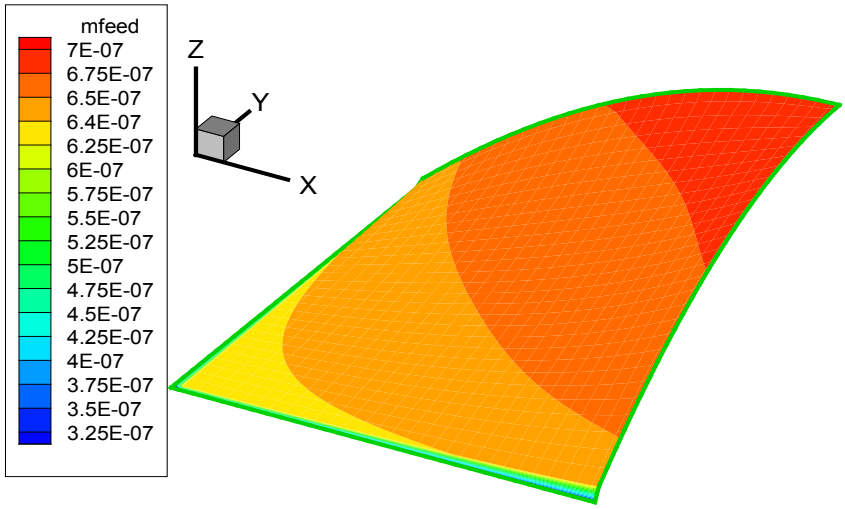

Figure 2-9: Feeding rate profile.

Figure 2-10 shows the stack surface morphology under different inlet temperatures. The stack height decreases as the inlet temperature increases due to the higher heat transfer rate from gas phase to solid phase. Figure 2-11 shows the stack surface morphology under different feeding rates. The stack height increases as the feeding rate increases due to a larger solid fuel accumulation at a higher feeding rate.

Note that, in all cases, a concave area is observed on the stack surface which is amplified as the stack height increases - known as the tunneling effect. The tunneling effect is mainly caused by two factors: (1) a higher feeding rate results in a higher stack (at the center line in current operation condition) and the corresponding porous drag increases accordingly; (2) a higher shear stress near the wall due to the no-slip condition reduces the momentum of the flow. The combination of the two effects causes the flow to experience a higher resistance and, as a consequence, the flow field is modified to the direction of minimal resistance. Therefore, the concave area becomes the major pathway of the flow passing the stack. Along this pathway, pyrolysis,

oxidation and gasification are more active, resulting in a shorter stack height (i.e., the tunnel). The tunneling effect can be alleviated by a higher inlet temperature and a lower feeding rate.

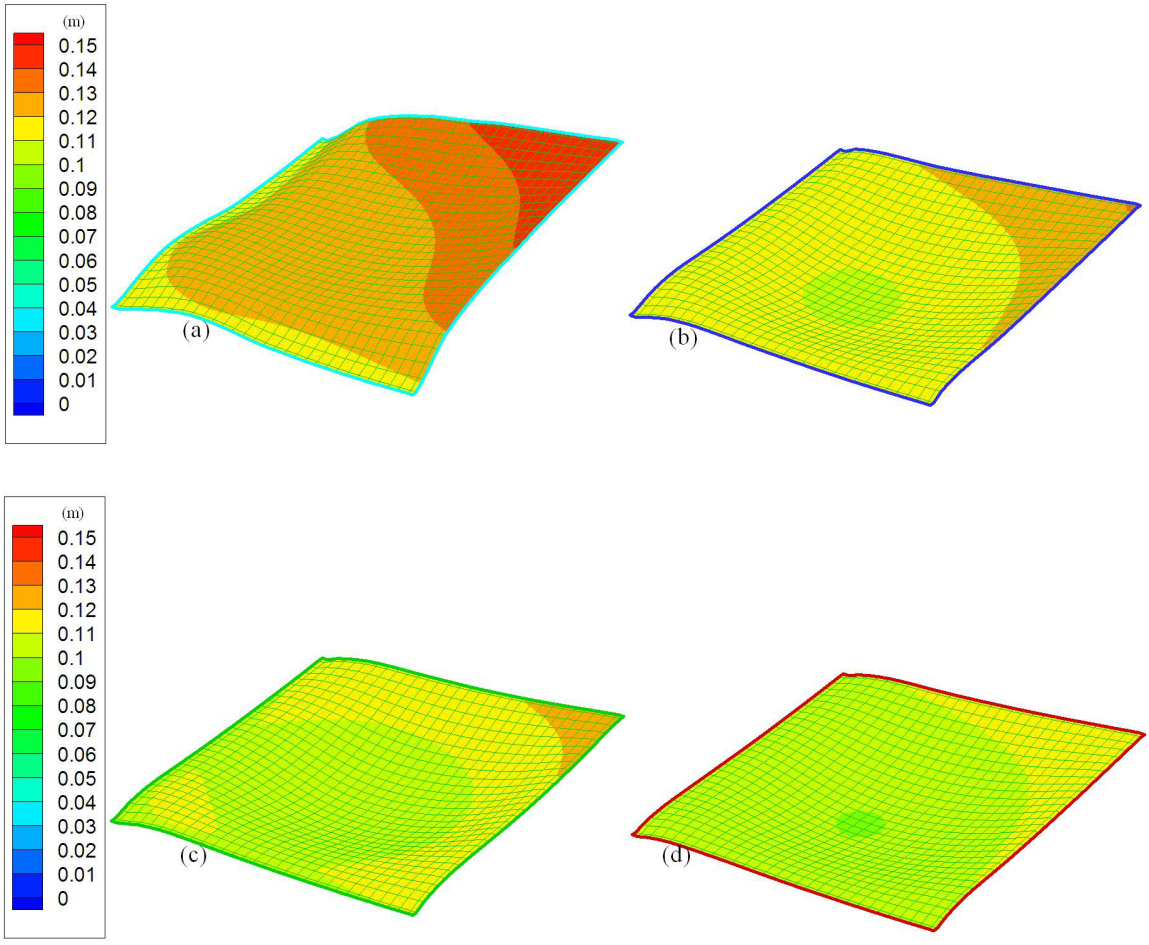

Figure 2-10: Stack surface morphology with different inlet temperature at feeding rate equals to 8.07. (a) T_{in} = 850K, (b) T_{in} = 950K, (c) T_{in} = 1050K and (d) T_{in} =1150K.

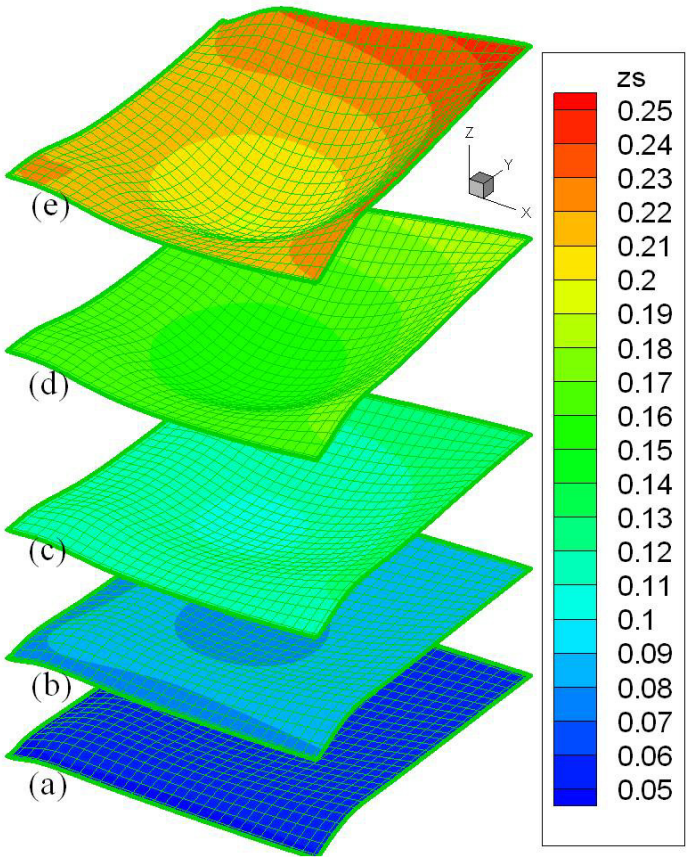

Figure 2-11: Stack surface morphology with different feeding rate at inlet temperature equals to 950K. (a) ψ = 3.03, (b) ψ = 5.58, (c) ψ = 8.07, (d) ψ = 10.70 and (e) ψ = 13.20.

Figure 2-12 shows how the flow is affected by the tunnel under the operation condition of ψ = 10.70, T_{in} = 950K. From the porosity field, it shows that a tunnel is formed and the velocity of flow near the tunnel is approximately 25% higher than the velocity elsewhere. To alleviate this problem, several key quantities to identify the stack morphology are examined for various parametric conditions.

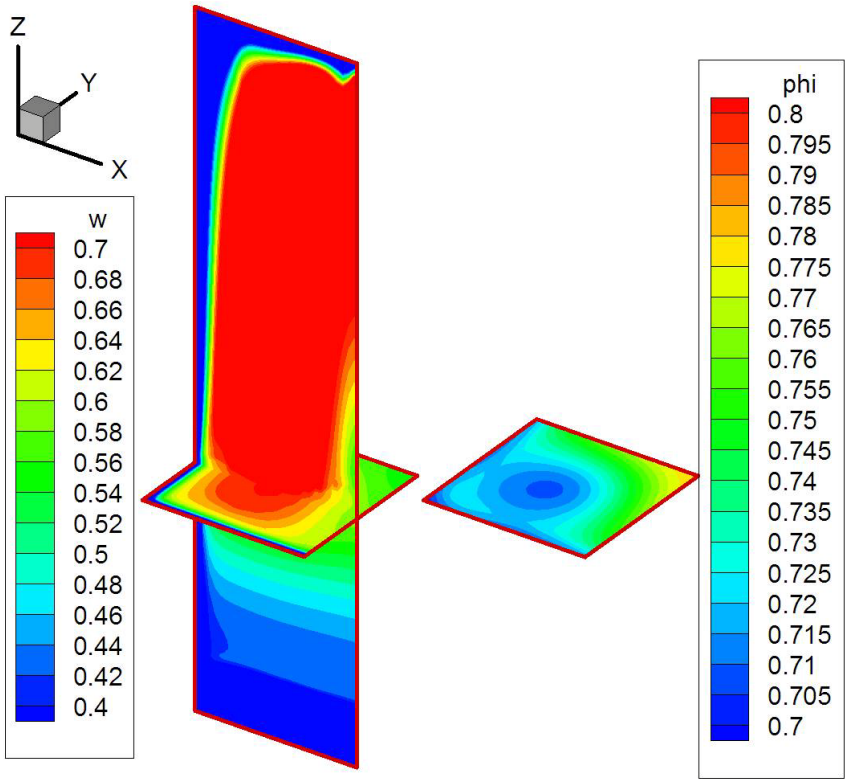

Figure 2-12: Flow is concentrated due to the tunnel effect at ψ = 10.70, T_{in} = 950K.

Figure 2-13 shows a top view of the porosity contour on the stack surface for various loading conditions. The lower left quadrant is shown here, such that the upper right corner corresponds to the center of the stack. In each case, the black solid circle indicates the iso-contour of 6% height reduction with respect to the tunnel center. Therefore, the size of the circle approximately represents the severity of the tunneling effect. As the feeding rate increases from ψ = 3.03 to 13.20, the 6% height reduction region is more concentrated, indicating that the tunneling effect becomes more severe.

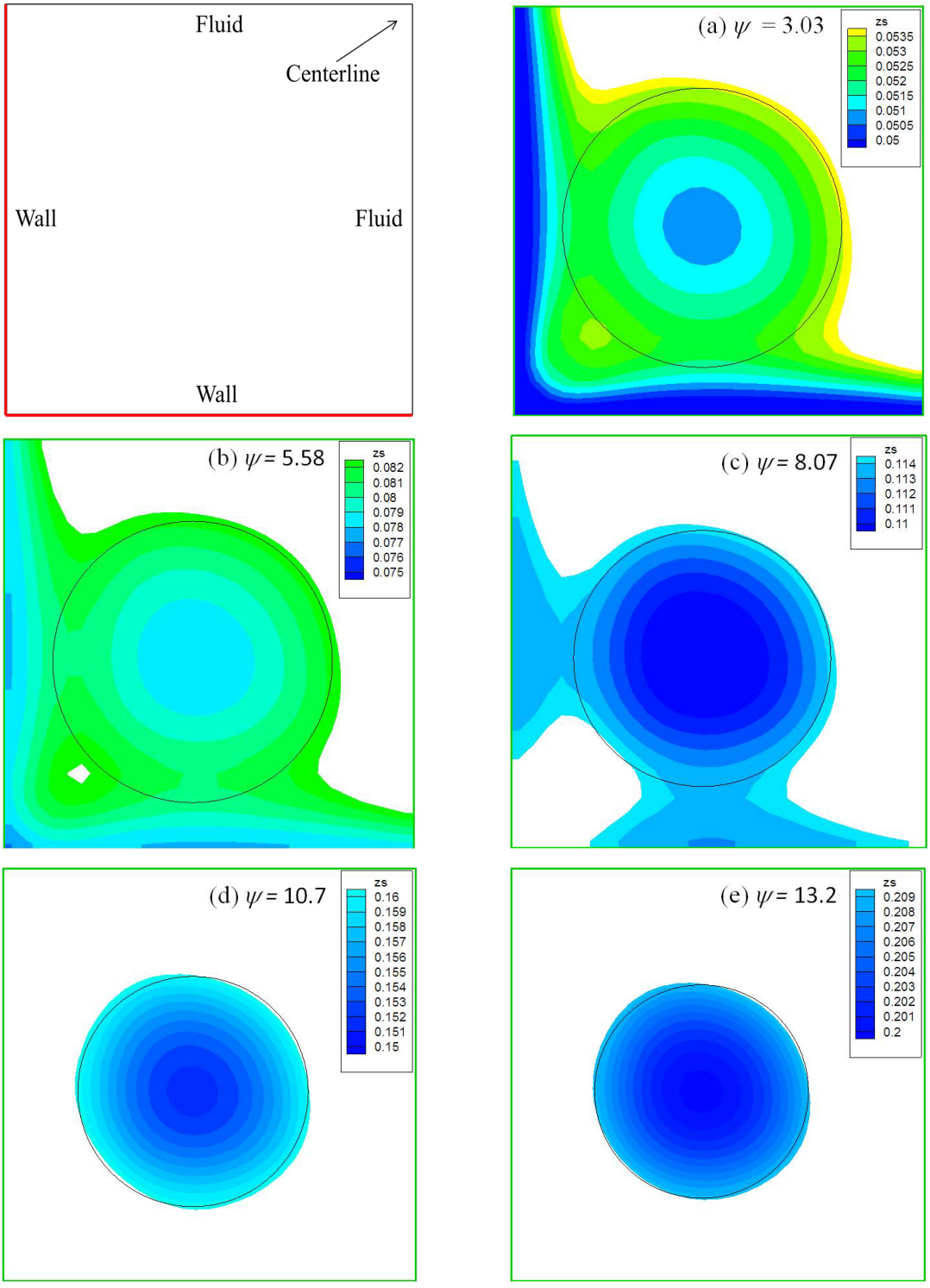

Figure 2-13: 6% height variation showing the tunnel structure in the stack 950K with a feeding rate of (a) $\psi = 3.03$, (b) $\psi = 5.58$, (c) $\psi = 8.07$, (d) $\psi = 10.70$ (e) $\psi = 13.20$.

Index of tunnel effect, κ, is proposed as a quantitative measure of the tunnel effect severity:

$$\kappa = \frac{L}{R} \tag{2-50}$$

where R and L is the radius of the tunnel and the half width of the gasifier, respectively. Figure 2-14 shows the variation in κ as a function of the feeding rate. Considering that the two low feeding rate cases (ψ = 3.03 and ψ = 5.58) as the reference conditions, κ increases by 11.5%, 20%, and 30% as the feeding rate increases from 8.07, 10.70 to 13.20, respectively, indicating tunnel effect becomes significant.

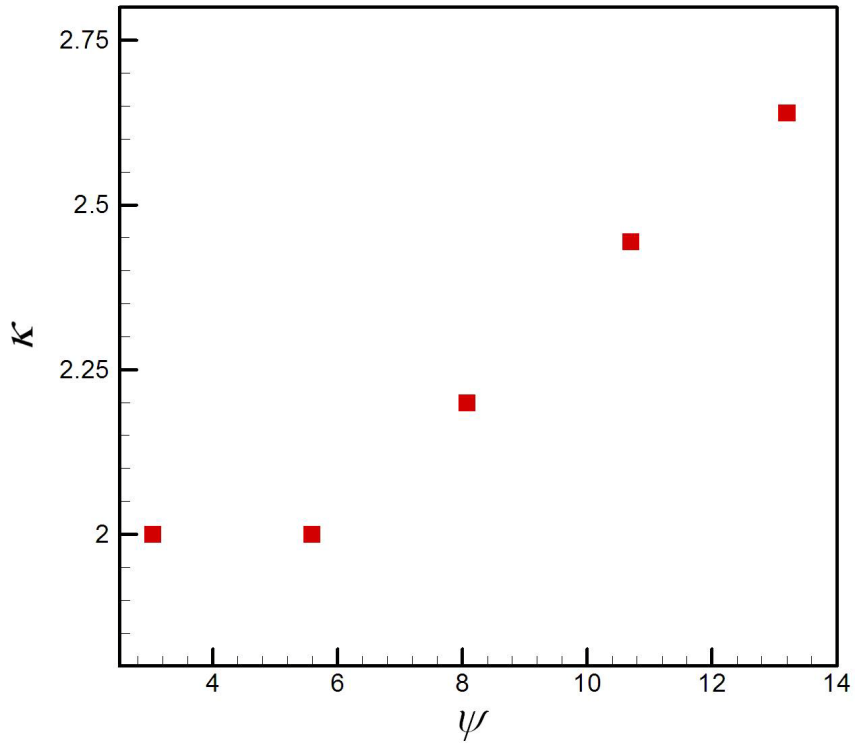

Figure 2-14: Index of tunnel effect versus the feeding rate, indicating that the tunnel effect is enhanced as the feeding rate increases.

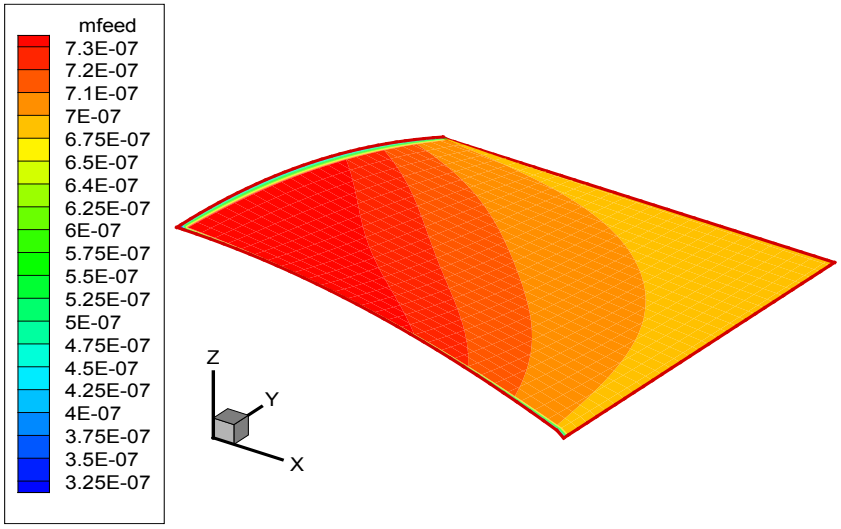

Figure 2-15: Reverse feeding profile.

The effects of the feeding rate profile are also examined while maintaining the total feeding rate at ψ = 8.07. Figure 2-15 shows the reverse feeding profile (feeding rate is higher near the wall and lower near the centerline) and Figure 2-16 shows the stack surface of a case of T_{in} = 950K and ψ = 8.07 when the feeding profile is reversed. The stack near the wall becomes higher due to the high feeding rate. Compared to Figure 2-12 (c), the tunnel effect is reduced and the corresponding κ reduces from 2.24 to 2.16. Figure 2-17 shows the stack surface profile for a uniform feeding rate profile with the constant feeding rate throughout. For this feeding profile, the 6% height reduction zone is significantly reduced and κ becomes close to unity, suggesting that the tunneling effect is almost vanished. The results suggest that an optimal combination of the feeding rate and feeding profile is desired in order to minimize the tunneling effect.

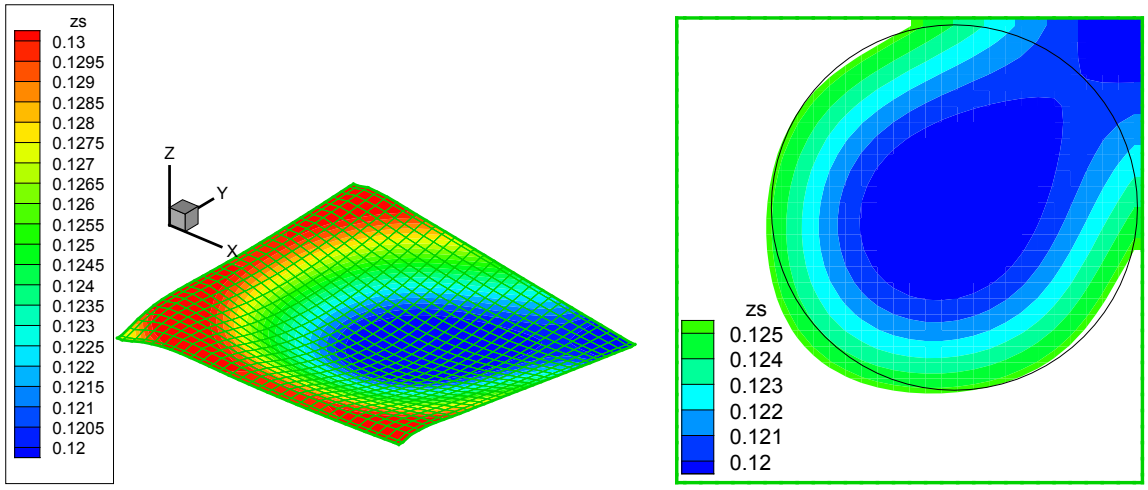

Figure 2-16: Stack surface and the corresponding 6% height reduction zone for a reverse feeding profile with T_{in} = 950K and ψ = 8.07.

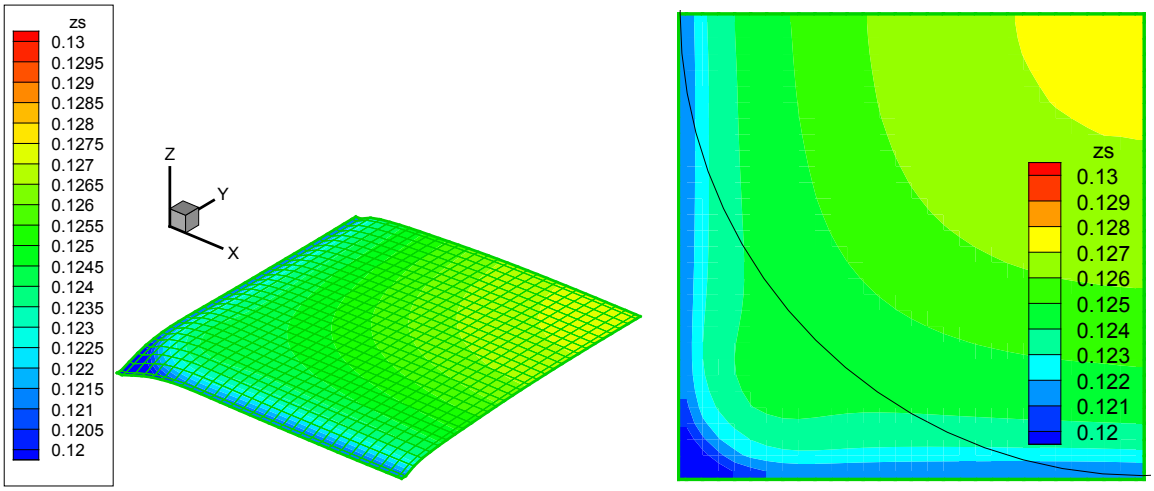

Figure 2-17: Stack surface and the corresponding 6% height reduction zone for a uniform feeding profile with T_{in} = 950K and ψ = 8.07.

2.6 Summary

A three-dimensional computational model was developed to simulate gasification processes inside a fixed-bed waste. The solid-phase waste materials were described by a porous medium and the multiphase flow is incorporated as a single continuum. The Lagrangian pyrolysis model was

proposed, which was described based on a phenomenological vaporization model following the energy balance between gas phase and a solid waste pellet, in which the rate of pyrolysis depends on the effective size of the characteristic waste sphere and the neighboring gas temperature.

The stack morphologies with different inlet temperature and feeding rate at steady state were studied. Simulations show that, as the inlet temperature increases, the stack height decreases. As the stack height decreases and the bed surface approaches the reaction zone, the bed surface shape is more dominant by the shape of the reaction zone instead of the fully-developed parabolic velocity profile. Hence the height variation also decreases and ends up with a more uniform bed surface. Likewise, the stack height and the height variation both reduce as the feeding rate decreases because less amount of solid waste is provided and a shorter stack is formed. Small height variation represents a more uniform bed surface which is preferred because the tunneling effect can be minimized. However, a lower yield was observed because the gaseous fuel was fully consumed via combustion immediately after solid fuel pyrolysis.

Under adiabatic wall condition, fixed inlet temperature and total feeding rate, the tunnel effect can be alleviated by reducing total feeding rate near the centerline. However, if the feeding rate near the centerline is lower than the feeding rate near the wall, the tunnel effect will not be resolved as desired. A uniform feeding profile is preferred for the conditions under consideration.

As a conclusion, the optimal operation condition at inlet temperature equals to 950K is ψ = 8.07 under a uniform feeding profile. The results

demonstrated that the model can be used for identifying optimal operating conditions of the gasifier at a given design conditions.

Chapter 3

Theoretical Investigation of Charring Solid Gasification in a Fixed-Bed Gasifier

In this chapter, the Lagrangian pyrolysis model is extended to describe the gasification of a more complex biomass material. A multiple-characteristic diameter (MCD) pyrolysis submodel is proposed in order to determine the rates of local devolatilization, evaporation and charring processes. The local porosity distribution is simultaneously determined by introducing the local characteristic diameters of the virtual solid spheres representing the solid wood. The flow field is described by a single-continuum three-dimensional model by introducing local porosity. Equations are solved by using the SIMPLE algorithm with momentum interpolation. One-step homogeneous (gas/gas) and heterogeneous (solid/gas) reactions are adopted for the chemical reactions inside the gasifier. Synthetic gas compositions from model prediction are compared with experiments conducted by Korean Institute of Energy Research (KIER) and good agreements are found. Model predictions are also compared with results calculated by equilibrium model (EQUIL) and the proposed model shows superior capability on accurate predictions. The results demonstrate that the model can properly capture the essential physical and chemical processes in the wood gasification process and thus can be used as a predictive simulation tool with adequate computational efficiency and accuracy.

3.1 Introduction

Active research on wood chip gasification has been led by Korea Institute of Energy Research (KIER) in the development and testing of pilot plant for commercial application (Lee *et al.*, 2009). Due to the complexity of biomass gasification processes, which generally involve multiphase flow, heat transfer, solid pyrolysis, heterogeneous and homogeneous reactions, the pyrolysis model developed in the previous chapter needs to be modified in order to account for variable volatility of different components in the solid material. The basic formulation and computational algorithm have been discussed in our previous studies (Im *et al*., 2004; Tsai *et al*., 2008; Tsai *et al*., 2010). The present study stems from authors' previous work, features a phenomenological pyrolsyis model based on wood drying, devolatilization and charring, and summarizes at a multi-characteristic diameter (MCD) model for a biomass gasifier. Synthetic gas compositions from model prediction are compared with experiments with good agreements. The validity of the model further justified by comparing with the results based on the equilibrium model, thereby demonstrating that the present model properly captures the non-equilibrium effects for accurate prediction of the syn-gas products.

3.2 Mathematical Formulations

The basic formulation and computational algorithm have been discussed in chapter 2. Considering the operation conditions for industrial gasifiers are mostly turbulent, a low Reynolds number turbulent k-ε has been applied and more detail discussion is available in Appendix C. The following

conservation equations describe the flow field as a single continuum with different porosity throughout the entire domain inside the gasifier. The steady system of equations (3-1)-(3-4) was solved using the SIMPLE algorithm (Patankar *et al.*, 1980) with pressure-weighted interpolation method (PWIM) (Rhie *et al.*, 1983).

Macroscopic steady gas phase continuity equation

$$\frac{\partial}{\partial x_i}\left(\rho u_{Di}\right) = \sum_j \dot{\omega}_{j,pyro} \tag{3-1}$$

where φ is the volume fraction of gas phase, i.e., porosity and u_{Dk} is volume-averaged Darcian velocity. The source term on the RHS accounts for the mass generation due to pyrolysis from solid phase to gas phase.

Macroscopic steady turbulent kinetic energy equation

$$\frac{\partial}{\partial x_k}\left(\rho u_k k\right) = \frac{\partial}{\partial x_j}\left[\left(\mu + \mu_t\right)\frac{\partial k}{\partial x_j}\right] + \mu_t \frac{\partial u_i}{\partial x_j}\left(\frac{\partial u_i}{\partial x_j} + \frac{\partial u_j}{\partial x_i}\right) - \rho\varepsilon - 2\mu\left(\frac{\partial \sqrt{k}}{\partial x_j}\right)\left(\frac{\partial \sqrt{k}}{\partial x_j}\right) \tag{3-2}$$

where k, ε are the turbulent kinetic energy and turbulent dissipation [m^2/s^3] rate [m^2/s^2]. μ_t is the turbulent viscosity defined as

$$\mu_t = C_\mu \rho \frac{k^2}{\varepsilon} \tag{3-3}$$

where $C_\mu = C_{\mu\infty} \exp\left[-2.5/(1.0 + \mathrm{Re}_t/50)\right]$ and constant $C_{\mu\infty} = 0.09$. Re_t is the turbulent Reynolds number and it is defined as

$$\mathrm{Re}_t = \frac{k^2}{\nu\varepsilon} \tag{3-4}$$

where v is the dynamics viscosity. The turbulent kinetic energy equation is similar to the standard high Reynolds number once except the last term on the RHS. The purpose for this additional sterm serves as a correction source which accords the model prediction to the experiment (Jones *et al*., 1972).

Macroscopic steady turbulent dissipation rate equation

$$\frac{\partial}{\partial x_k}\left(\rho u_k \varepsilon\right) = \frac{\partial}{\partial x_j}\left[\left(\frac{\mu_t}{\sigma_\varepsilon}+\mu\right)\frac{\partial \varepsilon}{\partial x_j}\right] + \frac{\varepsilon}{k}\left[C_{\varepsilon 1}\mu_t \frac{\partial u_i}{\partial x_j}\left(\frac{\partial u_i}{\partial x_j}+\frac{\partial u_j}{\partial x_i}\right) - C_{\varepsilon 2}\rho\varepsilon\right] + 2\frac{\mu\mu_t}{\rho}\left(\frac{\partial^2 u_i}{\partial x_j \partial x_l}\right)\left(\frac{\partial^2 u_i}{\partial x_j \partial x_l}\right) \tag{3-5}$$

where

$$\begin{aligned} \sigma_\varepsilon &= 1.3 \\ C_{\varepsilon 1} &= 1.44 \\ C_{\varepsilon 2} &= C_{\varepsilon 2\infty}\left[1.0 - 0.3\exp(-\mathrm{Re}_t^2)\right] \\ C_{\varepsilon 2\infty} &= 1.92 \end{aligned} \tag{3-6}$$

The turbulent energy dissipation equation is also similar to the standard high Reynolds number one except the last term on the RHS. The last term on the RHS has computational advantages from letting ε go to zero at the wall and ε may therefore be interpreted as the isotropic part of the energy dissipation (Jones *et al*., 1972). The last term become insignificant in the flow away from the wall due to the homogeneous turbulent flow structure and the velocity gradient in space is much less.

Macroscopic steady gas phase momentum equation

$$\frac{\partial}{\partial x_i}\left(\frac{\rho}{\varphi}u_{Di}u_{Dj}\right)=-\frac{\partial \varphi p}{\partial x_j}-\frac{2}{3}\frac{\partial}{\partial x_j}\left(\left(\mu+\mu_t\right)\frac{\partial u_{Dk}}{\partial x_k}\right)$$
$$+\frac{\partial}{\partial x_k}\left[\left(\mu+\mu_t\right)\left(\frac{\partial u_{Dj}}{\partial x_k}+\frac{\partial u_{Dk}}{\partial x_j}\right)\right]-\varphi\left(\frac{\mu}{K}+\frac{\rho C_F\sqrt{u_{Dk}u_{Dk}}}{\sqrt{K}}\right)u_{Dj} \quad (3\text{-}7)$$

Assuming that the thermal dispersion effects on the gas density is negligible and therefore the macroscopic density is equal to microscopic. $K=\varphi^3 D_s^2/150(1-\varphi)^2$ is the permeability and it is correlated with sphere diameter and porosity with the Carman-Kozeny equation. $C_F=1.75/\sqrt{150}\varphi^{3/2}$ is the dimensionless form-drag number (also called Forchheimer coefficient or inertia factor). D_s is the diameter of the solid particle.

Macroscopic steady gas phase energy equation

$$\frac{\partial}{\partial x_i}\left(\rho C_p u_{Di}T\right)=\frac{\partial}{\partial x_i}\left(\lambda_{eff}\frac{\partial T}{\partial x_i}\right)+\varphi\dot{q}'''-\frac{hA_s}{V}(T-T_s)+\dot{\omega}_{F,pyro}h_{fg} \quad (3\text{-}8)$$

where

$$\lambda_{eff}=\begin{cases}\varphi\left(\lambda+\lambda_t\right)=\varphi\left(\lambda+\dfrac{c_p\mu_t}{\mathrm{Pr}_t}\right) & \text{if } T\geq T_{pyro}\\ \varphi\left(\lambda+\lambda_t\right)+\left(1-\varphi\right)\lambda_s=\varphi\left(\lambda+\dfrac{c_p\mu_t}{\mathrm{Pr}_t}\right)+\left(1-\varphi\right)\lambda_s & \text{if } T<T_{pyro}\end{cases} \quad (3\text{-}9)$$

and $\mathrm{Pr}_t=\dfrac{\mu_t/\rho}{\lambda_t/\rho c_p}=\dfrac{\mu_t c_p}{\lambda_t}\approx 1$.

The present study assumes that the wood chip is an isotropic medium, such that K becomes a scalar instead of a second order tensor. T, C_p, λ and $\dot{q}'''$ are temperature, constant-pressure heat capacity, thermal conductivity the heat

generation due to gas phase chemical reactions. (3-9) suggests that, if the gas phase temperature is lower than the pyrolysis temperature, the solid and gas phase are under thermal equilibrium where the energy equation is for both solid and gas phase. On the contrary, if the gas phase temperature is higher than the pyrolysis temperature, the energy equation will be exclusively for gas phase temperature while the heat transfer on the solid will be calculated by the proposed pyrolysis model.

Macroscopic steady species equation

$$\frac{\partial}{\partial x_i}\left(\rho u_{Di} Y_m\right) = \frac{\partial}{\partial x_i}\left(\varphi \rho D_{eff} \frac{\partial Y_m}{\partial x_i}\right) + \sum\left(\varphi \dot{\omega}_m''' + \dot{\omega}_{m,pyro}\right) \qquad (3\text{-}10)$$

where

$$\rho D_{eff} = \rho\left(D + D_t\right) = \mathrm{Le}\left(\frac{\lambda}{c_p}\right) + \frac{\mu_t}{\mathrm{Sc}_t} \qquad (3\text{-}11)$$

and $\mathrm{Le} = \frac{\mathrm{Sc}}{\mathrm{Pr}} \approx 1$, $\mathrm{Sc}_t = \frac{\mu_t}{\rho \mathrm{Pr}_t} \approx 1$. Y_m, D and $\dot{\omega}_m'''$ are the mass fraction of species m, diffusivity and the gas phase reaction rate of species m.

The present model treats the solid stack region as a porous medium where solid and fluid co-exist. For the region outside the stack, where the pure fluid region is, the porosity is set to 1 and Eqs. (3-1), (3-2), (3-5), (3-7), (3-8) and (3-10) degenerate to the conventional gas-phase flow equations. Within the stack, the porosity varies from the initial value (typically 0.7 at the top of the stack) to the final value depending on the char removal rate (specified as 0.96 in present study). At the bottom, the wood chip is completely dried, pyrolyzed and left as char. As for the species transport equations (3-8), seven reactive species are considered: carbon monoxide, oxygen, carbon

dioxide, water, hydrogen, methane and inert which typically are the major species in biomass gasification processes.

The equation of state for porous and pure gas region is represented as follows:

$$P = \rho\left(\frac{R_u}{M}\right)T \tag{3-12}$$

where P is the thermodynamic pressure, R_u is the universal gas constant and M is the molecular weight of the mixture.

3.3 Multiple Characteristic Diameter (MCD) Pyrolysis Model

Extensive research toward biomass pyrolysis mechanisms has been conducted in the past five decades and recently biomass pyrolysis modeling become more and more important because of the increasing demand of bio-related fuels. Biomass pyrolysis modeling can typically be classified into three categories: analytical model (Atreya *et al.*, 2002; Baum *et al.*, 2007; Staggs, 2003), integral model (stags, 2000; Spearpoint*et al.*, 2000; Galgano *et al.*, 2004) and partial differential equation model (Bryden *et al.*, 2002; Bellais *et al.*, 2003). Because analytical solutions are not always available and partial differential equation models require excessive computational efforts, integral models show advantages over others as a balance between the computation cost and the accuracy. Integral models usually assume a temperature profile inside the solid and infinite rate kinetics are adopted. The proposed pyrolysis model stems from the concept of integral model and it can be summarized as follows:

1. Based on one dimensional mass and energy conservations.
2. Assume local thermal equilibrium inside the solid due to the fact that biomass are usually resized into small pieces to enhance its pyrolysis rate and prevent local oxidation.
3. Biomass accounts as a mixture of volatiles, moisture and char. The mass fractions are based on proximate analysis of the wood samples.

It is generally believed that the wood pyrolysis involves three processes: devolatilization, evaporation and charring which generate volatiles, moisture and intermediate solid. As volatile and moisture are released from the virgin wood, the intermediate solid is also gradually converted into char through the charring process.

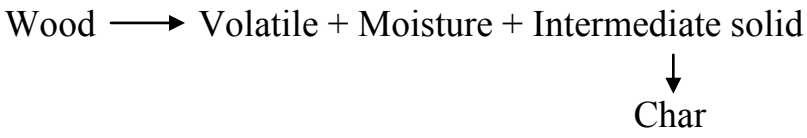

Usually wood pyrolysis would have generated tar which will subsequently result in secondary tar decomposition and form CO, CO_2, H_2, CH_4 and the undecomposed remainder will be left as high carbon number species such as benzene. Tar initially appears in a vapor form and it will condense on the surface of pipe lines or devices once the surrounding temperature is reduced. Tar is highly undesired due to its highly viscous nature. A synthetic gas would not be able to operate in an internal combustion engine properly if the tar concentration exceeds $1g/Nm^3$ (Beenackers, 1999). It is also suggested that, for sufficient tar decomposition, the optimal operation temperature is 1500K with at least 0.5 second of residence time for tar (Han, 2006). Therefore, a downdraft biomass gasifier is preferred due to its nature of higher gasification temperature and longer residence time. Considering the

current study is associated with a downdraft gasifier, it has been assumed that the tar has been fully decomposed into synthetic gas via devolatilization process. As the three parallel processes are single step and competing, MCD pyrolysis model includes three characteristic diameters representing volatile, $\overline{d}_v$, moisture, $\overline{d}_m$, and intermediate solid/char, $\overline{d}_c$, and three virtual spheres are formed accordingly. When the pyrolysis temperature is reached, as Figure 3-1 shows, three shrinking trajectories form simultaneously.

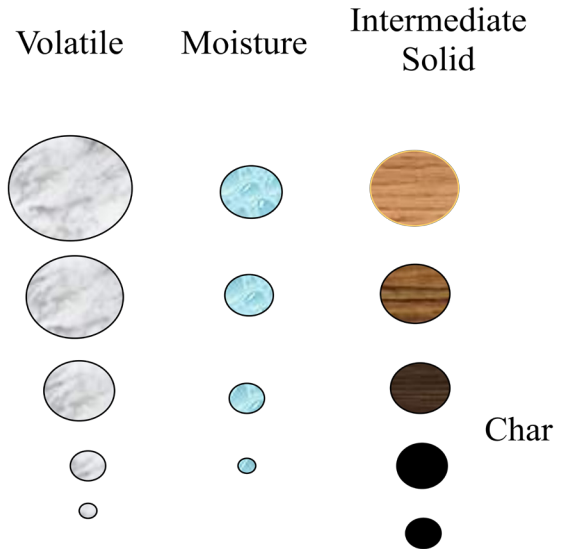

Figure 3-1: Characteristic diameters of volatile, moisture and intermediate solid/char.

The characteristic diameters of the three virtual spheres representing volatiles, moisture and char can be determined from

$$\frac{\rho_v \overline{d}_{v,0}^3}{\rho_w d_0^3} = V\% \qquad \frac{\rho_m \overline{d}_{m,0}^3}{\rho_w d_0^3} = M\% \qquad \frac{\rho_c \overline{d}_{c,0}^3}{\rho_w d_0^3} = C\% \tag{3-13}$$

where V, M and C are the mass fractions of volatiles, moisture and intermediate solid/char, respectively. ρ_v, ρ_m, ρ_c, ρ_w, $\overline{d}_{v,0}$, $\overline{d}_{m,0}$, $\overline{d}_{c,0}$, and d_0

are density of volatile, density of water, density of char, density of virgin wood and the initial characteristic diameter of the virtual sphere formed by volatile, moisture, char and virgin wood, respectively. According to Lee *et al.* (2009), *V*, *M* and *C* are 84.55, 0.17 and 15.28, respectively. Material properties are listed in Table 3-1.

Table 3-1: Known material properties.

Property	Value	Source	Property	Value	Source
ρ_w	676.0 kg/m^3	Atreya, 1983	d_0	2.18 x 10^{-3} m	KIER
ρ_V	1.553 kg/m^3	Calculated	$\overline{d}_{v,0}$	0.1521 m	Calculated
ρ_M	998.0 kg/m^3		$\overline{d}_{m,0}$	2.223 x 10^{-3} m	Calculated
ρ_C	162.24 kg/m^3	Atreya, 1983	$\overline{d}_{c,0}$	1.823 x 10^{-2} m	Calculated

The average characteristic diameter, $\overline{d}$, is the volume sum of all the individual characteristic diameters as

$$\overline{d}^3 = \sum_i \overline{d}_i^3 \tag{3-14}$$

which is applied to determine the local porosity and the local heat transfer rate.

When the hot gas flows through the solid bed, the size of virtual spheres of volatile and moisture start to decrease and generate volatile, moisture to the gas phase due to heat transfer. The characteristic diameter of virtual sphere of char also decreases due to heterogeneous reactions.

The heterogeneous reactions on char surface determine the height of the stack due to the slow reaction rates. Depends on the residence time of the

char inside the gasifier, the bed height can be determined accordingly. Starting from the stack surface and going downward, the characteristic diameters of volatile, $d_{v,0}$, char, $d_{c,0}$, and moisture, $d_{m,0}$, are shrinking from their initial values until they are fully converted into gas phase due to pyrolysis except the characteristic diameter of char. The final value of the characteristic diameter for char is pre-specified which implies that the remaining char has to be removed from the gasfier. This is common in most industrial gasifiers for charring materials such as municipal solid wastes, medical wastes and biomass.

3.3.1 Pyrolysis Temperature

Pyrolysis temperature is the temperature where heat flux balances the mass generation (i.e., the pyrolysis front) due to pyrolysis and it is used to determine the drying rate, devolatilization rate and, the heterogeneous reactions rates. For integrated model, pyrolysis temperature needs to be specified as a parameter. A general relation between the pyrolysis temperature, T_{pyro}, the heat flux, $\dot{q}''$, and the sample size, L', was proposed by Park *et al.* (2009). Figure 3-2 shows the Non-dimensional correlation of finite-rate pyrolysis-front models for a wood slab, cylinder and sphere for estimating the mass-and-energy-balanced T_{pyro}, and the correlation is shown as follows

$$\frac{T_{pyro}}{T_R} = 0.0416\left[\frac{E}{RT_R} - \ln\left(\frac{A\Delta h L'\rho_w}{\dot{q}''}\right)\right] + 0.9874 \qquad (3\text{-}15)$$

where T_R, E, R, A, Δh, L', ρ_w, and $\dot{q}''$ are reference temperature (298K), activation energy (125.58 kJ/mol), universal gas constant, pre-exponential constant(2.5E+8 s^{-1}), heat of pyrolyisis (2260.0 kJ/kg), characteristic length

(volume/surface area, i.e., $d/6$ in current study where d is the characteristic diameter), virgin wood density (633 kg/m^3) and external heat flux.

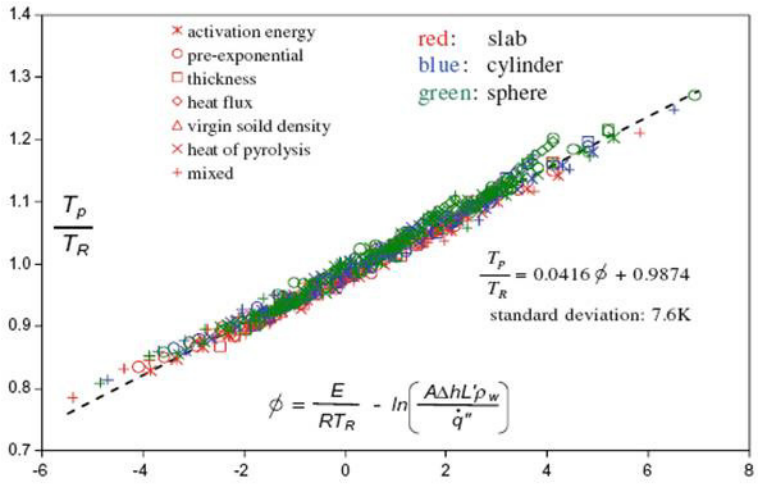

Figure 3-2: Non-dimensional correlation of finite-rate pyrolysis-front models for a wood slab, cylinder and sphere for estimating the mass-and-energy-balanced T_{pyro}. (Park *et al.*, 2009)

As (3-15) shows, the pyrolysis temperature varies with the external heat flux and the characteristic length. Figure 3-3 shows the pyrolysis temperature calculated from (3-8) based on different external heat fluxes and characteristic lengths. At gas phase temperature lower than 600K, the pyrolysis temperature is less dependent to characteristic lengths because the heat flux is small and the pyrolysis front locates close to the material surface. This cause the pyrolysis temperature close to the gas phase temperature and the pyrolsyis is insignificant due to the low heat flux. On the contrary, the bifurcation appears when gas phase temperature increases due to the fact that smaller characteristic length results in higher heat flux, which consequently results in a higher pyrolysis temperature.

In a gasifier, the gasification process usually takes place close to a combustion zone and the corresponding gas phase temperature can range

from 800K to 2500K depending on the operation conditions. The initial sample diameter used for the current study is 2cm hence the pyrolysis temperature has been assumed to be a constant at 625K.

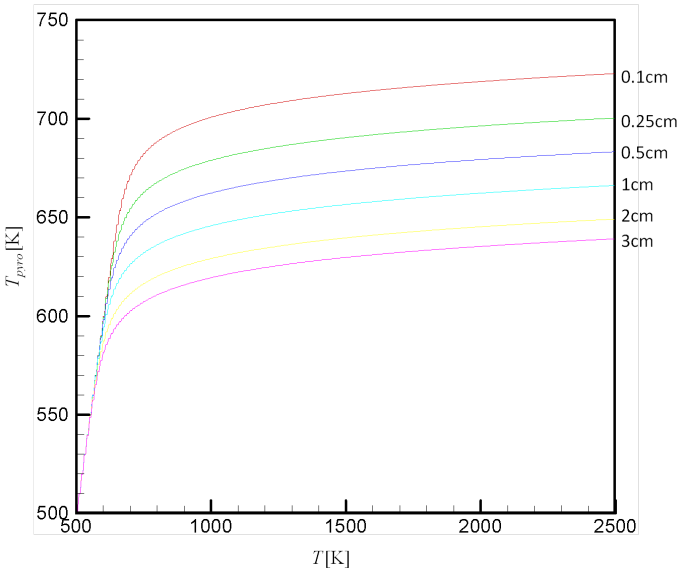

Figure 3-3: Pyrolysis temperature of wood at different characteristic diameters and gas phase temperatures.

3.3.2 Devolatilization

Early studies (Shin *et al*., 2000; Choi *et al*., 2001; Di Blasi *et al*., 2001; GrØnli, *et al*., 2002) suggest that the devolatilization rate is proportional to the instantaneous volatile concentration and the external heat transfer. Therefore, MCD model suggests the devolatilization rate can be expressed as

$$\frac{dm_v}{dt} = -\left(\frac{m_v}{m_{total}}\right)\frac{h\overline{A_s}\left(T - T_{pyro}\right)}{h_{p,v}} \tag{3-16}$$

where m_v, m_{total}, h, $\overline{A_s}$ are instantaneous mass of volatile in the sample, instantaneous mass of the sample, convection heat transfer coefficient and

the surface area of the interface formed by the characteristic sphere. $h_{p,v}$, like latent heat, is a retarding force to the external heat transfer which include the energy required for C-C bond breaking, ring opening and reforming (Liao *et al.*, 2004) of the fiber structure of the biomass to release volatile and it can be determined based on the given experiment data.

By introducing the pre-specified specific feeding velocity, v_d [m/s], the trajectory in space of the characteristic diameter for volatile, $\overline{d}_v$, can be can be expressed as

$$\frac{d\overline{d}_v^2}{dz} = -\left(\frac{4\mathrm{Nu}\lambda}{\rho_v h_{p,v}}\right)\left(\frac{\rho_v \overline{d}_v^3}{\sum_i \rho_i \overline{d}_i^3}\right)\left(\frac{\overline{d}}{\overline{d}_v}\right)\left(\frac{T - T_{pyro}}{v_d}\right) \tag{3-17}$$

where Nu, λ and ρ_v are solid-gas interfacial Nusselt number, the conductivity [W/m·K] of the gas, and the density of volatile, respectively. For spherical particles, the solid-gas interfacial Nusselt number can be determined from the following relation (Wakao *et al.*, 1976):

$$\mathrm{Nu} = 2 + 1.1\,\mathrm{Re}^{0.6}\,\mathrm{Pr}^{1/3} \tag{3-18}$$

Introducing the cell volume, J, and the total number of characteristic spheres in the cell, η, the devolatilization rate per unit volume, $\dot{\omega}_{pv}$ [kg/m^3-s], can be determined as

$$\dot{\omega}_{pv} = \frac{\eta}{J}\left(\frac{\pi\mathrm{Nu}\lambda}{h_{p,v}}\right)\left(\frac{\rho_v \overline{d}_v^3}{\sum_i \rho_i \overline{d}_i^3}\right)\overline{d}\left(\frac{T - T_{pyro}}{v_d}\right) \tag{3-19}$$

The generated products from devolatilization are CO and CO_2 and the generation rates for CO is half of the rate of CO_2. Trace amounts of acetic

acid, formaic acid and methanol are also observed and they are neglected in current study (Pan *et al.*, 1990).

3.3.3 Evaporation

Evaporation process has been modeled by applying the energy balance at the interface of gas and sphere constituted by water and water vapor is the product generated by the drying process.

$$\dot{m}_m h_{fg} = h\overline{A_s}(T - T_{boil}) \tag{3-20}$$

where $\dot{m}_m$, h_{fg}, h, $\overline{A_s}$ and T_{boil} are the mass flow rate of moisture due to evaporation, the latent heat of water, the convection heat transfer coefficient, the surface area of the interface formed by the characteristic sphere and the boiling temperature of water (i.e., 398K), respectively. Similar to the droplet evaporation problem (Law, 2006), the evaporation constant, K_e, can be determined by the d^2-law:

$$\frac{dd_m^2}{dt} = -\left(\frac{4\mathrm{Nu}\lambda}{\rho_m h_{fg}}\right)\left(\frac{\overline{d}}{\overline{d}_m}\right)(T - T_{pyro}) = -K_e \tag{3-21}$$

where Nu, λ and ρ_m are solid-gas interfacial Nusselt number, the conductivity [W/m·K] of the gas, and the density of water, respectively. Similar to (3-19), the evaporation rate per unit volume, $\dot{\omega}_{pm}$ [kg/m^3-s], can be determined consequently as

$$\dot{\omega}_{pm} = \frac{\eta}{J}\left(\frac{\pi\mathrm{Nu}\lambda}{h_{fg}}\right)\overline{d}\left(\frac{T - T_{boil}}{\nu_d}\right) \tag{3-22}$$

3.3.4 Validation

Wood pellet with different diameters was pyrolized under 1123K and the weight loss history was measured (Sreekanth *et al.*, 2010). As mentioned in 3.3.2, $h_{p,v}$ can be calculated based on the experiment data as 1.2 MJ/kg.

Figure 3-4 shows an excellent agreement of model prediction and the experiment. It takes about four minutes to complete the pyrolysis with a volatile content less than 1% and 99% of the remainder has converted into char.

The weight loss during pyrolysis is majorly contributed by devolatilization due to the fact that (1) char reactions are generally much slower and their contributions on weight loss are insignificant; and (2) the moisture content in biomass is usually 5% ~ 20% in weight and the evaporation process usually is faster due to the fact that the boiling temperature is much lower than the pyrolysis temperature. The evaporation process completes from the first 40 seconds to two minutes, respectively, with a sample diameter less than 3cm - which is usually the dimension for waste gasifiers.

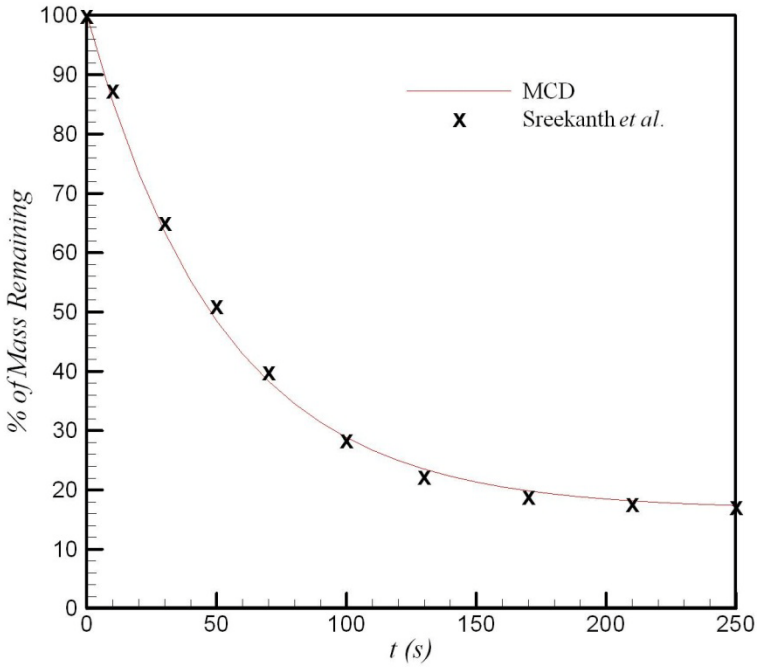

Figure 3-4: Weight loss history due to pyrolsyis with a sample diameter 2.0cm and the gas temperature is 1123K.

Figure 3-5 shows the weight loss history under different initial sample diameters and, again, excellent agreements are seen. The devolatilization is defined completed as the remaining volatile content in the sample is less than 1% and the time required to complete the devolatiliztion process for initial diameter of 1.5cm, 2.0cm and 3.0cm are 90 seconds, 230 seconds and 400 seconds, respectively. As shown in Figure 3-5, the devolatilization completes faster if the initial sample diameter is reduced. This is due to the fact that a smaller sample contents less volatile and the energy required to release the volatile is less. Although the total heat transfer rate varies as the sample diameter varies $\left(\propto \overline{d} / \overline{d}_v\right)$, the devolatililization rate is more affected by the volatile concentration inside the sample since it is proportional to $\left(\overline{d}_v^3 / \sum_i \rho_i \overline{d}_i^3\right)$ which is shown in (3-17). As a consequence, the devolatilization rate increases as the initial sample size decreases.

Figure 3-6 shows the weight loss history under surrounding gas temperature ranging from 1023K to 1223K with the same initial sample diameter as 2.0cm. The devolalitlization rate increases as the surrounding gas temperature increases due to a higher external heat transfer rate. Again, the model predictions agree with experiments.

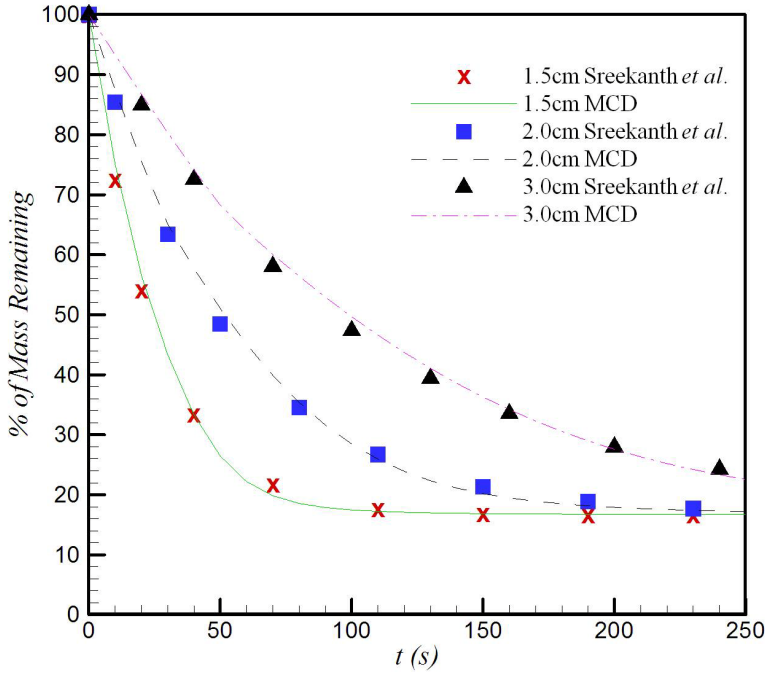

Figure 3-5: Weight loss history due to pyrolysis with sample diameter ranging from 1.5cm to 3cm and the gas temperature is 1123K.

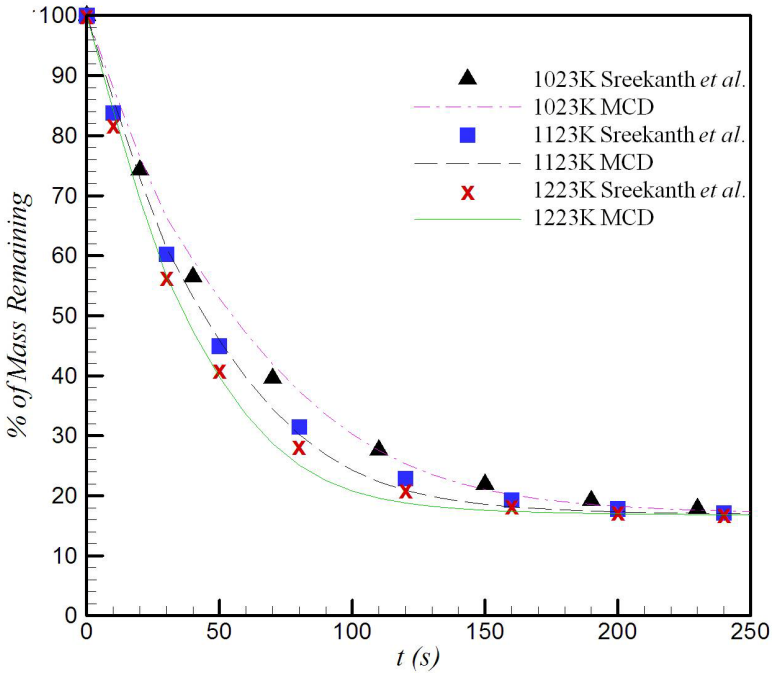

Figure 3-6: Weight loss history due to pyrolysis with the gas temperature ranging from 1023K to 1223K and the sample diameter is 2.0cm.

3.3.5 Heterogeneous Reactions (Char+Gas Reactions)

Unreacted-core shrinking model (Wen, 1968) was adopted to determine the heterogeneous reaction rates. The model includes the effects of ash layer diffusion, gas film diffusion and chemical kinetics. In current study, the ash layer diffusion is neglected since there is no temperature gradient inside the entire solid phase and the solid phase temperature is assumed to remain at the pyrolysis temperature (i.e., 625K) when it is exposed to the hot surrounding air and the pyrolysis occurs. Therefore, all heterogeneous reactions listed in Table 3-3 are determined by gas film diffusion chemical kinetics and

$$Rate_{overall} = \Omega k_{diff} \left(P_i - P_i^* \right) \quad [\,\mathrm{g/cm^2\text{-}s}\,] \tag{3-23}$$

where Ω, k_{diff} and $P_i - P_i^*$ are degree of charring, gas film diffusion constant and the effective partial pressure of gas specie *i* taking account of the reverse reaction. As shown in Table 3-2, four global one-step heterogeneous reactions suggested by Liu *et al.* (2001) are adopted to model heterogeneous char+gas reactions: Char+O_2, Char+H_2O, Char+CO_2 and Char+H_2 reactions where T_s, K_{eq} and P_{total} are solid temperature, equilibrium constants and total pressure, respectively.

The degree of charring, Ω, accounts for the effect that the reactivity increases as the wood converting from virgin wood to intermediate solid, and from intermediate solid to char. In current study, the degree of charring is assumed to be

$$\Omega \models -\left(\frac{\overline{d}_v}{\overline{d}_{v0}} \right)^3 \tag{3-18}$$

Table 3-2: Rate expressions for char+gas heterogeneous reactions.

Process	Reaction	Coefficients
Char+O_2 (Wen *et al.*, 1979)	$C+\frac{1}{2}O_2 \rightleftharpoons CO$ $Q_{C/O2}$ = -7831 kcal/kg	$k_{diff} = 0.584\left(\frac{4.26}{T}\right)\left(\frac{T}{1800}\right)^{1.75} / P_{total}d$ $P_i - P_i^* = P_{O_2}$
Char+H_2O (Dobner, 1976)	$C+H_2O \rightleftharpoons CO+H_2$ $Q_{C/H2O}$ = +2705 kcal/kg	$k_{diff} = 10^{-3}\left(\frac{T}{2000}\right)^{0.75} / P_{total}d$ $P_i - P_i^* = P_{H_2O} - \left(P_{H_2} - P_{CO}\right)/K_{eq}$ $K_{eq} = \exp\left[17644 - 30260/\left(1.8T_s\right)\right]$
Char+CO_2 (Dutta *et al.*, 1977)	$C+CO_2 \rightleftharpoons 2CO$ $Q_{C/CO2}$ = +3382 kcal/kg	$k_{diff} = 7.45 \text{ x } 10^{-4}\left(\frac{T}{2000}\right)^{0.75} / P_{total}d$ $P_i - P_i^* = P_{CO_2}$
Char+H_2 (Wen, 1968)	$C+H_2 \rightleftharpoons CH_4$ $Q_{C/O2}$ = -1798 kcal/kg	$k_{diff} = 1.33 \text{ x } 10^{-3}\left(\frac{T}{2000}\right)^{0.75} / P_{total}d$ $P_i - P_i^* = P_{H_2} - \sqrt{P_{CH_4}/K_{eq}}$ $K_{eq} = 5.04 \text{ x } 10^{-6}\exp\left[18400/\left(1.8T_s\right)\right]$

indicating that the charring process will be completed as the devolatilization process is completed. The overall reaction rate for char, $\dot{\omega}_C$ [kg/m^3-s], can be summarized as the sum of individual reaction rates as

$$\dot{\omega}_C = \sum_i \dot{\omega}_{C_i} \tag{3-19}$$

Through mass conservation, the mass loss due to heterogeneous reactions is correlated with the volume variation of the virtual char sphere

$$\dot{\omega}_C = \frac{1}{J}\frac{dm_c}{dt} = \frac{\rho_c \pi}{6J}\frac{dd_C^3}{dt} = \frac{v_d \rho_c \pi d_C}{4J}\frac{\partial d_C}{\partial z} \tag{3-20}$$

where m_c and ρ_C are the mass of the virtual char sphere and char density.

3.3.6 Homogeneous Reactions (Gas+Gas reactions)

As shown in Table 3-3, five global one-step homogeneous reactions suggested by Liu *et al.* (2001) are adopted: fuel oxidations (H_2+O_2, CO+O_2, CH_4+O_2), water-gas shift (WGS) and methane-stream reforming reactions where MW_i, X_i are molecular weight and molar concentration for specie i, respectively.

Table 3-3: Rate expressions for gas+gas homogeneous reactions.

Process	Reaction	Reaction rates
Fuel Oxidations (Siminski *et al.*, 1972)	$H_2 + \frac{1}{2}O_2 \rightarrow H_2O$ $CO + \frac{1}{2}O_2 \rightarrow CO_2$ $CH_4 + 2O_2 \rightarrow CO_2 + H_2$ $Q_{H2/O2}$ = -28619 kcal/kg $Q_{CO/O2}$ = -2415 kcal/kg $Q_{CH4/O2}$ = -11934 kcal/kg	$Rate_i = -59.8 P_{total}^{0.3} TMW_i X_i^{0.5} X_{O_2}$ x $\exp(-12200/T)$ i = H_2, CO or CH_4
Water-Gas Shift (Singh *et al.*, 1977)	$CO + H_2O \rightleftharpoons CO_2 + H_2$ $Q_{CO/H2O}$ = +351 kcal/kg	$Rate_{CO} = 5.54 \text{ x } 10^4 \left(P_{CO} - \frac{P_{CO_2} P_{H_2}}{K_{eq} P_{H_2O}} \right)$ x $\exp[-27760/(1.987T)]$ x $P_{total}^{-(P_{total}/250+0.5)}$ x $\exp[-8.91+5553/T]$ $K_{eq} = \exp[(9998.22/T - 10.213 + 2.7465\text{E-}3T$ $-0.453\text{E-}6T^2 - 0.201\ln T)/1.987T]$

Methane-Steam Reforming (Zahradnik *et al.*, 1974)	$CH_4 + H_2O \rightleftharpoons CO + 3H_2$ $Q_{C/O2}$ = -3079 kcal/kg	$Rate_{CH_4} = 312\exp\left[-30000/(1.98T)\right]$

The homogeneous reaction rates are characterized by two distinct time scales: chemical reaction rate and the turbulent mixing rate. The temperature inside the gasifier is usually high and the corresponding homogeneous reaction rates are generally fast compared with turbulent mixing rate. Therefore, the local homogeneous reaction rates are restricted by the local turbulent mixing limit. Spalding (1971) proposed eddy break up model to account for the mixing effect on turbulent combustion as:

$$Rate_{i,mixing} = \frac{C_{mix}\rho\varepsilon}{k} Y_i \tag{3-21}$$

where C_{mix} = 3.0 and Y_i are the constant of eddy break up model and the species concentration on reaction i. In each homogeneous reaction, the smaller one is taken to represent the effective reaction rate. The eddy breakup models assume that the chemical reaction rates are limited by mixing and this approach is valid for Damkohler number » 1. The characteristic flow time in a gasifier is usually large due to the nature of gasification processes so the mass flow rate of the oxidizer supplied form the inlet is small; On the other hand, the operation temperature of a gasifier is usually high and most homogeneous and heterogeneous reactions occur at the combustion and gasification zone are fast. Therefore, the standard Damkohler number for a gasifier system can range from 10^2 to 10^4. Hence

eddy breakup models provide a computationally efficient way to simulate the combustion with turbulent mixing. A future improvement will be apply the prescribed PDF model because it accounts for the turbulent mixing in a more statistically sophisticated manner than the eddy breakup type models.

3.4 Surrogate Fuel Model and Equilibrium Tests

Considering the stoichiometric reaction of the wood, $CH_{1.65}O_{0.69}$ (Gupta *et al.*, 2007):

$$CH_{1.65}O_{0.69} + 1.0675O_2 \rightarrow CO_2 + 0.825H_2O \qquad (3\text{-}22)$$

CHEMKIN, however, does not allow an arbitrary species like $CH_{1.65}O_{0.69}$ as an input, hence a thermodynamically equivalent surrogate fuel is defined as a linear combination of C_2H_2, H_2, CO_2 and O_2 and the corresponding stoichiometric balance equation for the surrogate fuel reaction can be expressed as

$$[aC_2H_2 + bCO_2 + cO_2 + dH_2] + .0675O_2 \rightarrow CO_2 + 0.825H_2O \qquad (3\text{-}23)$$

The surrogate fuel yields (1) the identical product composition and (2) heat of formation as those obtained from the wood (-578068.125 kJ/kmol-surrogate fuel). This leads to the following element and enthalpy balance equations:

$$\text{C: } 2a + b = 1 \qquad (3\text{-}24a)$$

$$\text{H: } 2a + 2d = 1.65 \qquad (3\text{-}24b)$$

$$\text{O: } 2b + 2c = 1.515 \qquad (3\text{-}24c)$$

Enthalpy: $a\bar{h}^0_{f,\mathrm{C2H2}} + b\bar{h}^0_{f,\mathrm{CO2}} - \bar{h}^0_{f,\mathrm{CO2}} - 0.825\ \bar{h}^0_{f,\mathrm{H2O}}$

$$= -578068.125 \text{ kJ/kmol-fuel} \qquad (3\text{-}24d)$$

where $\bar{h}^0_{f,i}$ denotes the standard heat of formation at 298.15K for species *i*. Solving the above equations for the four unknowns yields

$$a = 0.373378,\ b = 0.253243,\ c = 0.504257,\ d = 0.451622 \qquad (3\text{-}25)$$

The practical range for gasification is commonly in a fuel-rich condition, and the surrogate fuel can be adopted for the parametric studies without causing a difficulty in the equilibrium calculation. The non-dimensional feeding rate, ψ, is defined as

$$\psi = \frac{\dot{m}_s}{\dot{m}_{O_2}} \qquad (3\text{-}26)$$

where $\dot{m}_s$ and $\dot{m}_{O_2}$ are the mass flow rate of wood and oxygen, respectively. ψ =10.58 in the experiment conducted by KIER.

3.5 Experiment and Numerical Configurations

Figure 3-7 shows the picture and the schematic drawing of a prototype gasifier developed at KIER. In this fixed-bed type design, biomass prepared in pellet form is supplied from the top with an average mass flow rate of 0.02 kg/s, while preheated air (at 625K) is supplied from the bottom with an average mass flow rate of 8.22 x 10^{-3} kg/s with 70% relative humidity. The preheated air further reacts with the synthetic gas and generated sufficient heat to sustain the system. The products of gasification are a mixture of gas

(synthetic gas, steam and CO_2) and solid phase (slag, char and ash), such that proper devices are required to separate and collect them. For gas products and ash, they are collected from the top. A cyclone and a filter are used to separate gas products and ash. For slag and char, they are gathered from the very bottom for post-processing and disposal. The operation temperature of the combustion zone and gasification zone ranges from 1050K to 1300K.

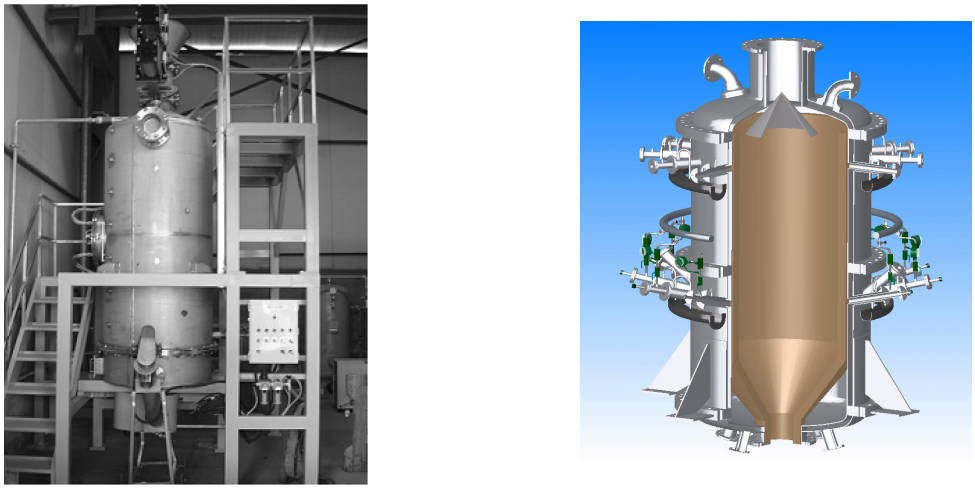

Figure 3-7: Gasification facility developed by KIER (left), and diagram of the gasifier under study by KIER (right) (Lee *et al.*, 2009).

As the schematic plots shown in Figure 3-7, the gasifier consists of three parts: inlet duct, neck and chamber, from bottom to top respectively. The diameter and height of the inlet duct are both 0.2m. The diameter and height of the chamber are 0.6m and 2.4m, respectively. Inlet duct and chamber are connected by the neck with a height of 0.56m. On the right is the grid used for the simulation based on Cartesian coordinate system and 20.5k grid points were deployed.

Table 3-4: Synthetic gas compositions reported by KIER experiment.

Mass Fraction	H_2	CO	CH_4	CO_2	N_2
Maximum	0.007	0.397	0.011	0.214	0.237
Minimum	0.011	0.514	0.024	0.299	0.318
Average	0.0085	0.4518	0.0195	0.2575	0.2627
Standard Deviation	0.0010	0.0249	0.0024	0.0209	0.0222

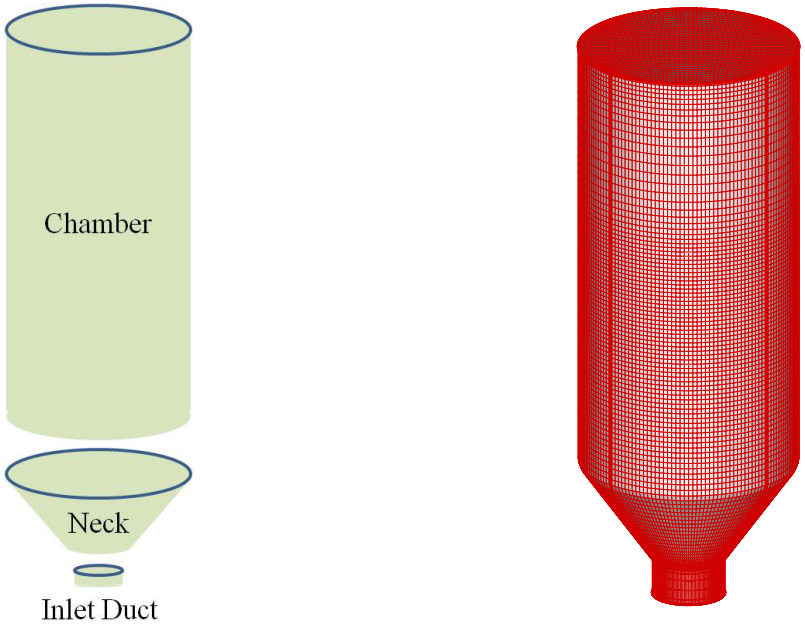

Figure 3-8: The schematic plot of the gasifier configuration (left) and grid used for the simulation (right).

Table 3-4 is the experiment data reported by KIER. The steady state is reached after 500 minutes of operation and the data is measure for the following 500 minutes. The experiment suggests that the major species for gas products are H_2, CO, CH_4, CO_2 and N_2. The maximum, minimum, averaged values and standard deviation of the major species are shown accordingly.

3.6 Results and Discussion

As shown in Chapter 2, a uniform feeding profile is preferred to minimized the tunneling effect and the uniform feeding profile is applied to the proposed study at a feeding rate equals to 0.02 kg/s hence the characteristic feeding velocity is 6.0 x 10^{-3} m/s as a constant. Figure 3-9 shows the porosity, overall heat release rate and the temperature fields and Figure 3-10 shows the heterogeneous Char+O_2, Char+CO_2, Char+H_2O and Char+H_2 reaction rates, respectively. Due to a uniform feeding profile, a uniform stack surface is observed which tunnel effect is minimized. The overall heat release rate contour shows a standard combined exothermic/endothermic structure of a gasifier. Figure 3-11a and 3-11b show the semi-global heterogeneous and homogeneous reactions, respectively along the centerline of the gasifier. The porosity profile indicates the location of the stack and, as shown in Figure 3.11a and 3.11b, the combustion zone is formed at the bottom part of the stack where oxygen is sufficient. The combustion zone is contributed majorly by the exothermic heterogeneous Char+O_2, Char+H_2 reactions and exothermic homogeneous CO+O_2 reaction providing sufficient amount of heat to sustain the gasification. On the top of the combustion zone, an endothermic gasification zone is majorly contributed by the endothermic heterogeneous Char+CO_2 and Char+H_2O reactions.

Figure 3-12 shows the overall oxygen reaction rate, devolatilization rate, overall CO and CO_2 reaction rates. As shown in the figure, the maximum devolatilization rate occurs at the top of the stack due to a larger averaged characteristic diameter proving that the model is capable of reproducing the combustion zone, gasification zone and drying/devolatilization zone in a correct order. In the combustion zone, the oxygen is quickly consumed

majorly due to Char+O_2 and CO+O_2 reactions in the combustion zone. At the same location, although CO+O_2 forms CO_2 leading to a high CO_2 generation rate, CO_2 is quickly consumed by the endothermic Char+CO_2 reaction which generates CO. Together with Char+O_2 reaction, this explains the reason why the overall CO generation rate is maximized while the overall CO_2 generation rate is minimized at the gasification zone. On the top of the gasification zone, the CO_2 generation rate increases again due to the devolatilization process which its contour is shown on the right.

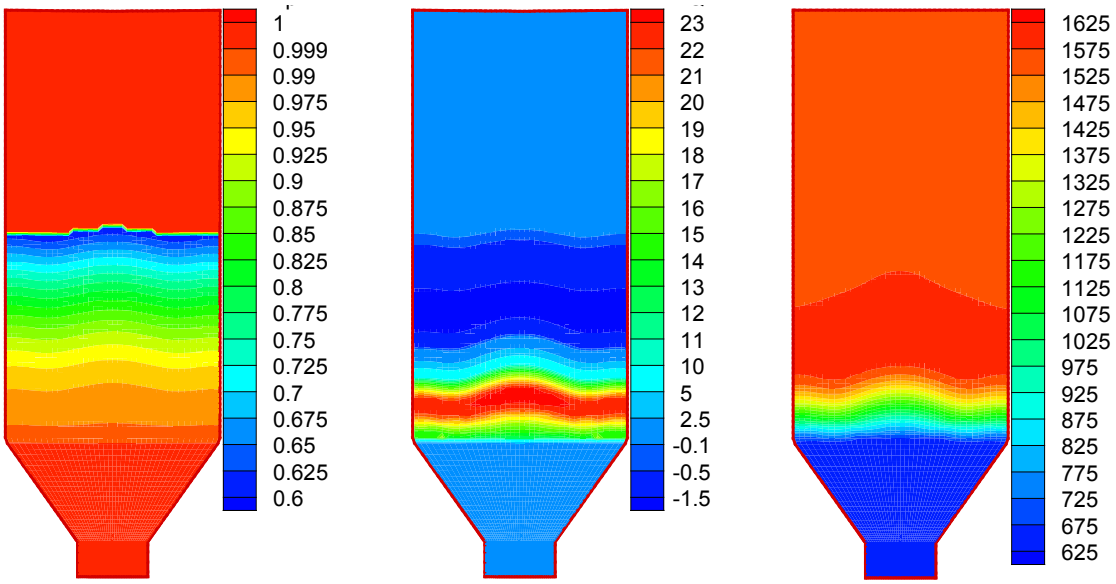

Figure 3-9: Porosity (left), heat release rate [kJ/m^3-s] (middle) and temperature [K] (right).

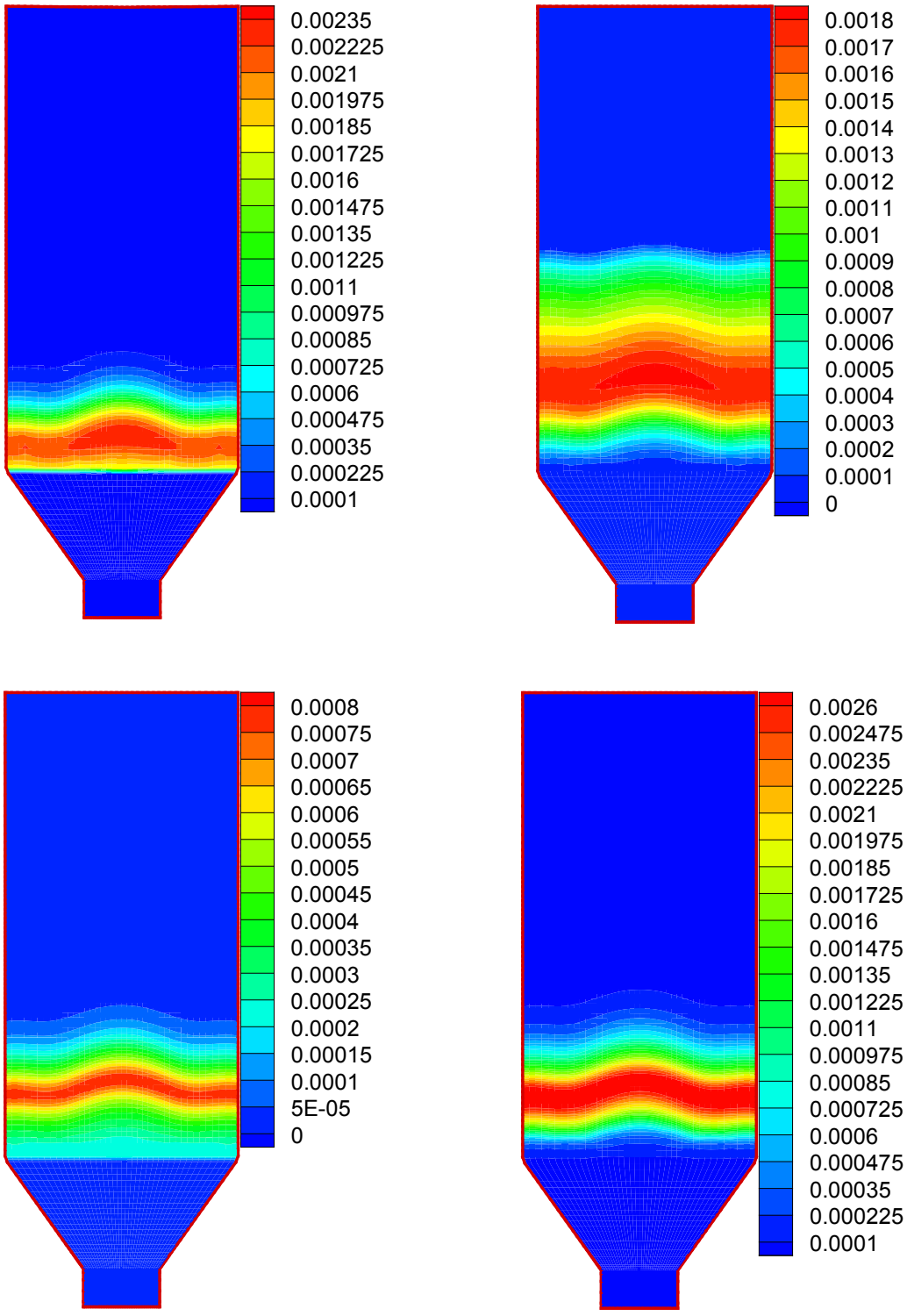

Figure 3-10: Exothermic heterogeneous Char+O_2 reaction rate [kg/m^3-s] (upper left), endothermic heterogeneous Char+CO_2 reaction rate [kg/m^3-s] (upper right), endothermic heterogeneous Char+H_2O reaction rate [kg/m^3-s] (lower left) and exothermic heterogeneous Char+H_2 reaction rate [kg/m^3-s] (lower right).

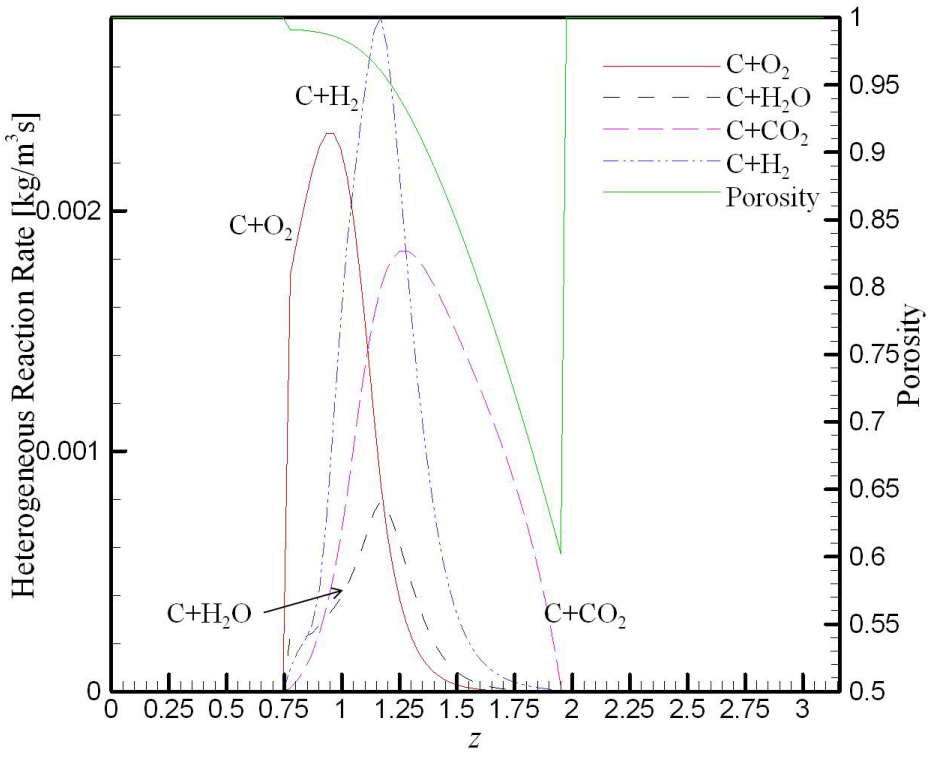

Figure 3-11a: Heterogeneous reaction rates at the centerline of the gasifier.

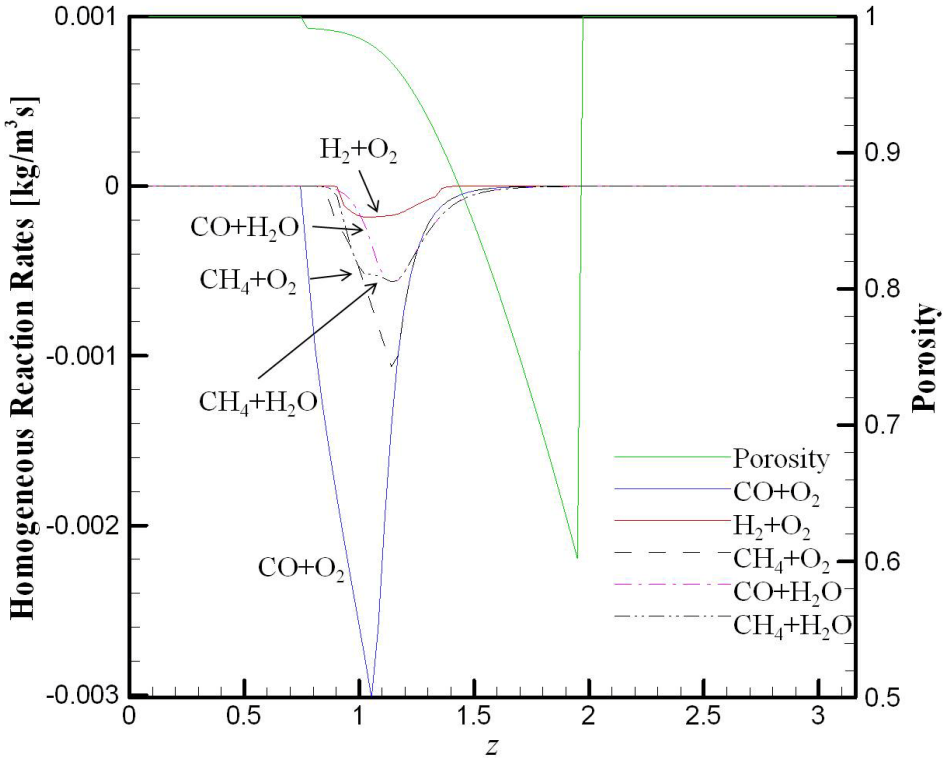

Figure 3-11b: Homogeneous reaction rates at the centerline of the gasifier

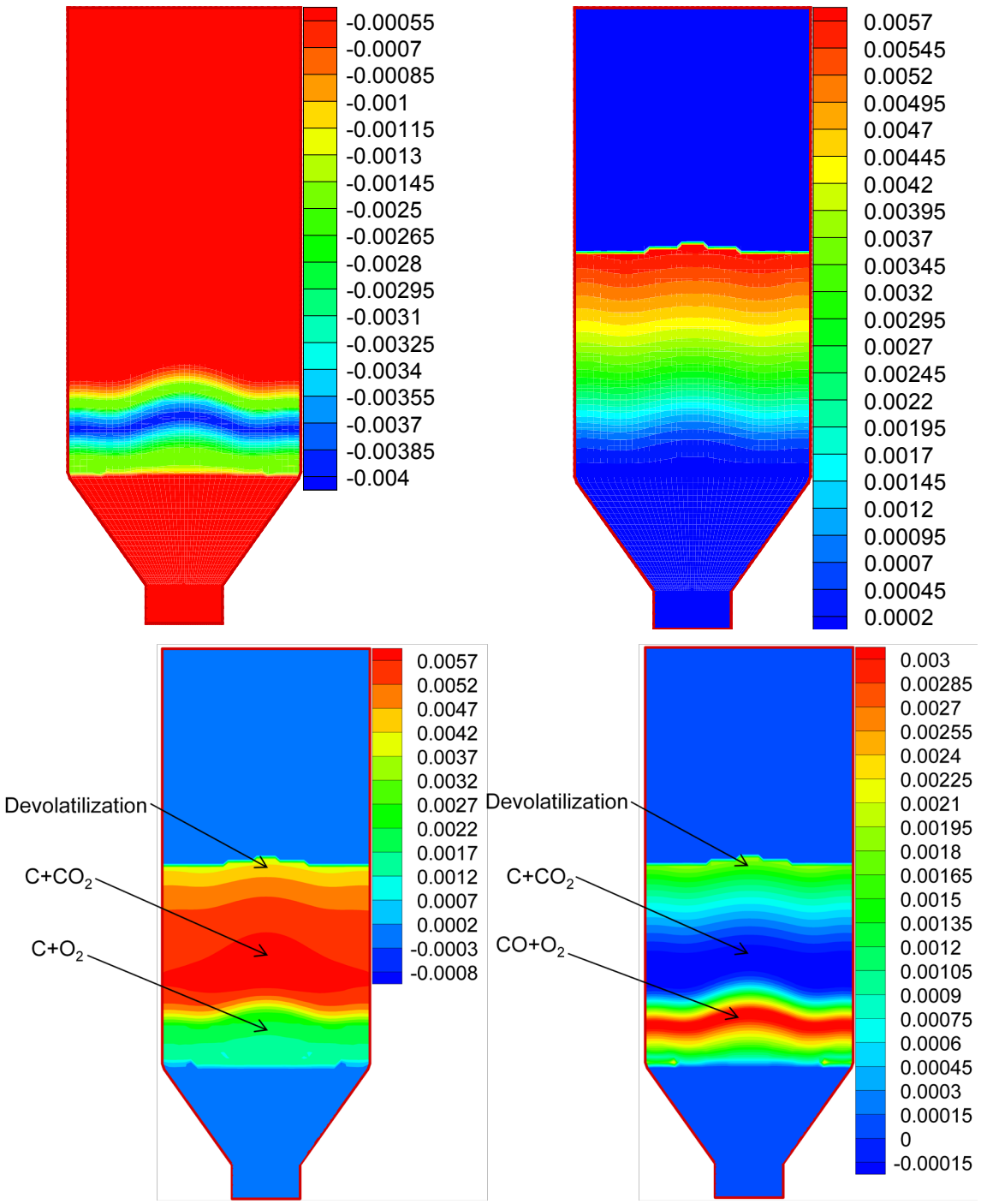

Figure 3-12: Overall oxygen reaction rate [kg/m^3-s] (upper left), devolatilization rate [kg/m^3-s] (upper right), overall CO reaction rate [kg/m^3-s] (lower left) and overall CO_2 reaction rate [kg/m^3-s] (lower right).

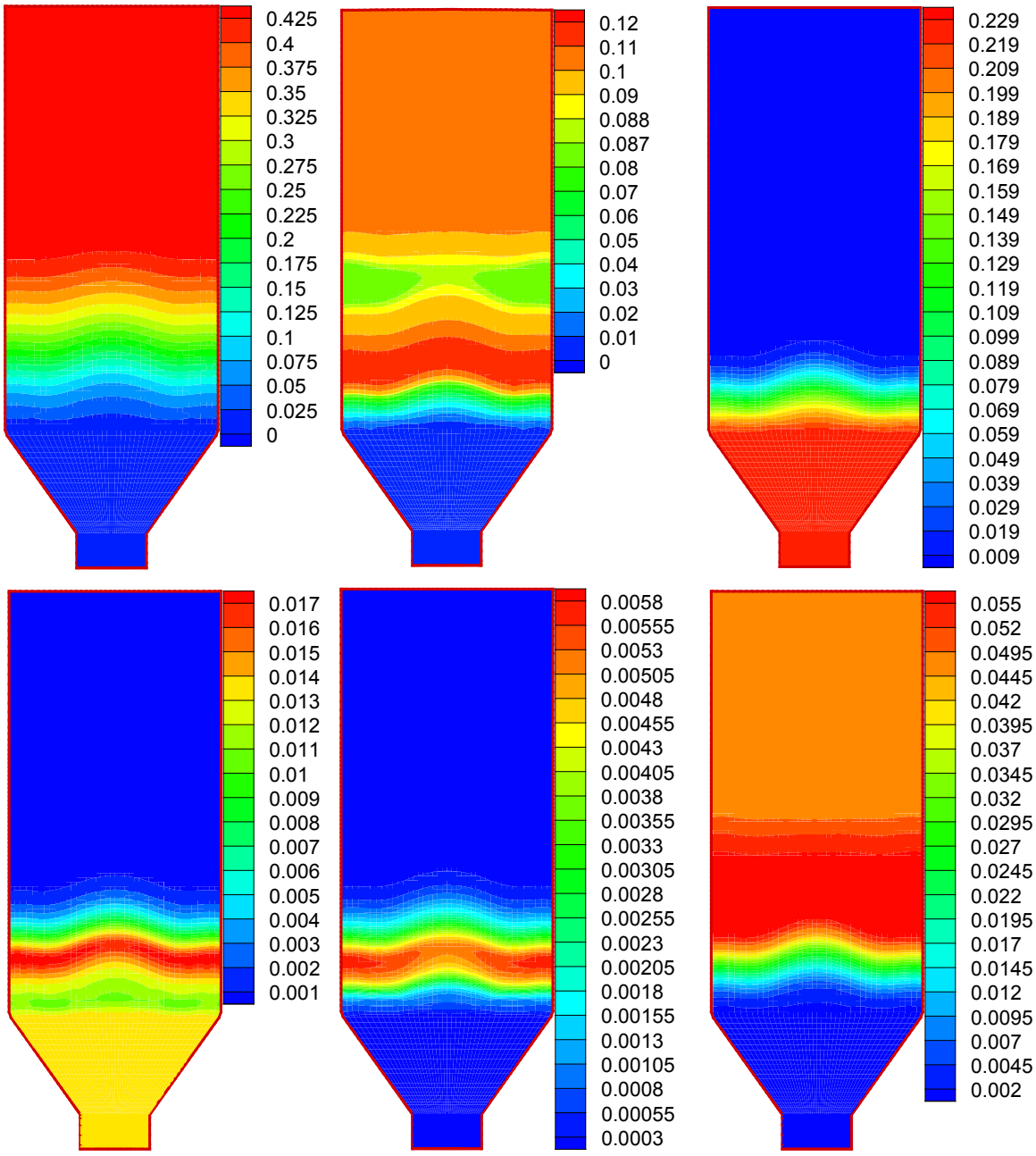

Figure 3-13: CO mass fraction (upper left), CO_2 mass fraction (upper middle) and O_2 mass fraction (upper right), H_2O mass fraction (lower left), H_2 mass fraction (lower middle) and CH_4 mass fraction (lower right).

H_2 and CH_4 are only formed when moisture exists through the following initiating sequence:

(a) $C + H_2O \rightleftharpoons CO + H_2$

(b) $C + 2H_2 \rightleftharpoons CH_4$

Then water gas shift, CH_4+O_2 and H_2+O_2 reactions will subsequently generate more H_2O and H_2 for (a) and (b). Figure 3-13 shows the concentration of CO, CO_2, O_2, H_2O, H_2 and CH_4, respectively. CO increases monotonically from the bottom part of the stack due to the heterogeneous/homogeneous reaction and devolatilization processes. On the other hand, starting from the bottom of the stack, CO_2 increases due to the homogeneous CO+O_2 combustion followed by a decreasing caused by the Char+CO_2 reaction and increases again due to the devolatilization. It is worth noting that, as shown in Figure 3-10, the Char+H_2 reaction is the major production source for CH_4 in the synthetic gas.

Figure 3-14 shows the synthetic gas composition at the center line from inlet to outlet predicted by MCD pyrolysis model. MCD pyrolysis model shows that CO, CO_2, N_2, CH_4 are major species and H_2 and H_2O are only in trace amounts (denoted as T/A). Table 3-5 compares the experiment data with MCD pyrolysis model and EQUAL model (at 1500K) and the prediction made by MCD pyrolysis model has a better agreement with the experiment. The CO_2 prediction by MCD is less and, with the proposed reactions, this may due to two possible reasons: (1) the mixing is enhanced due to the complex and tortuous structure inside the porous media and the eddy breakup model underestimated the mixing rate in the porous media and limited the CO+O_2 reaction rate resulting a lower CO_2 production; (2)

although under a high temperature, CO and CO_2 balance generally move toward the CO side (Arthur, 1951), the heterogeneous Char+O_2 reaction may still generate CO_2 yielding a higher CO_2 concentration. These studies can be regarded as future work.

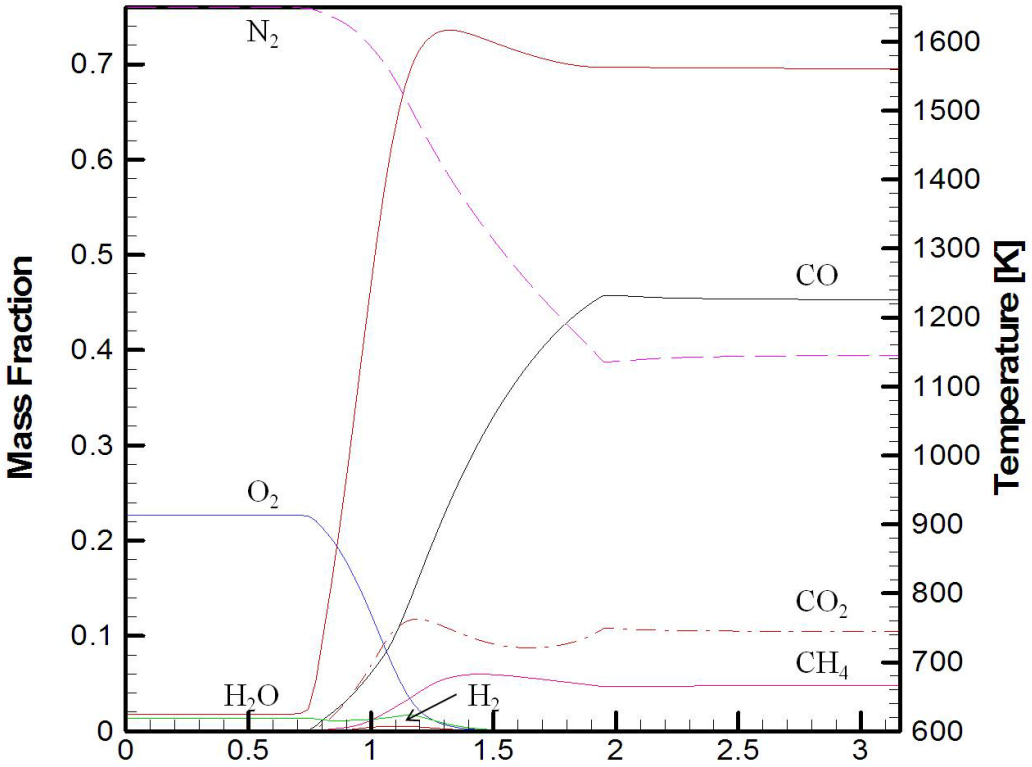

Figure 3-14: Synthetic gas composition predicted by MCD pyrolysis model.

Table 3-5: Synthetic gas compositions Comparisons.

Mass Fraction	H_2	CO	CH_4	CO_2	N_2	O_2	H_2O
KIER Experiment	0.01	0.45	0.02	0.26	0.26	T/A	T/A
MCD Pyrolysis Model	T/A	0.45	0.05	0.12	0.38	T/A	T/A
EQUIL (at 1500K)	0.02	0.35	T/A	0.28	0.23	T/A	0.14

The prediction made by EQUIL is quite different than the experiment result. This may due to the fact that the species residence times in the gasifier are limited and the system has not reached a fully equilibrium state. To verify

this, as shown in Figure 3-15, two equilibrium tests were conducted in different locations inside the gasifier and the species concentrations under equilibrium are plotted on the top of the result predicted by MCD pyrolysis model. It shows, for both locations A and B, are not in an equilibrium state. It doesn't show the trend that the MCD results will asymptotically collapse with the equilibrium results. This may due to the fact that equilibrium models didn't simulate the pyrolysis part correctly because devolatilization rate will greatly be reduced as the volatile content decreases.

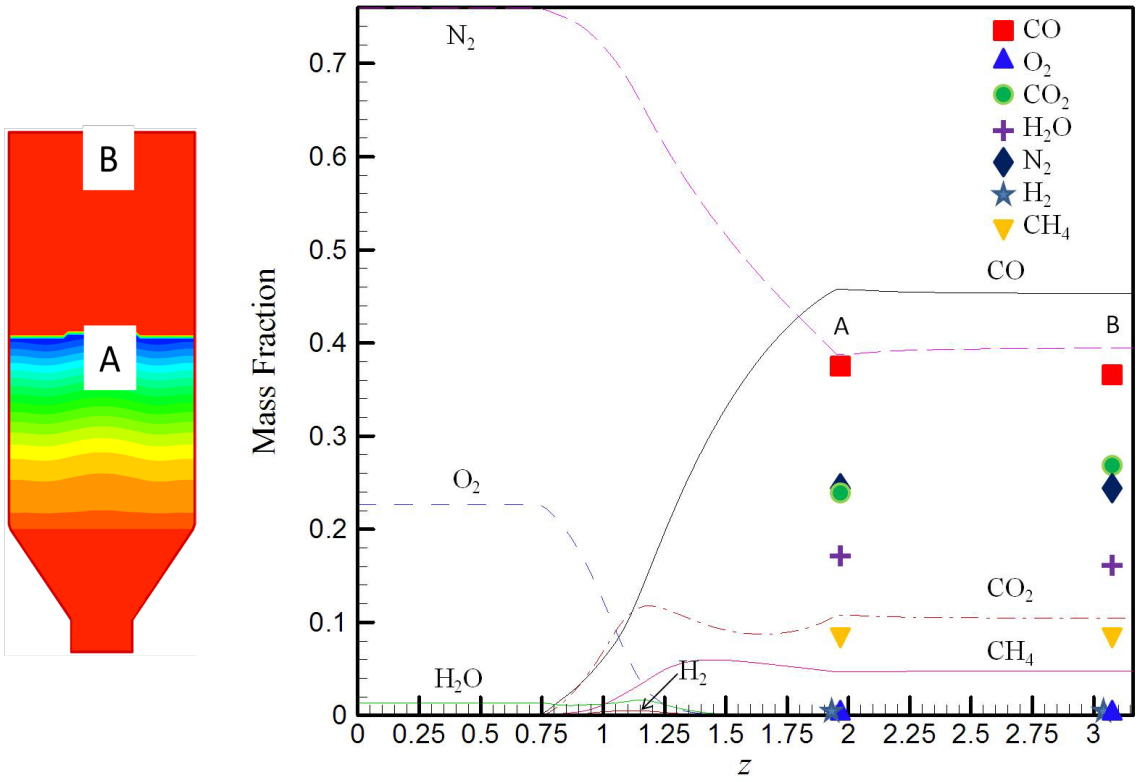

Figure 3-15: Locations of EQUIL tests (left) and the comparisons of synthetic gas composition predicted by MCD pyrolysis model and EQUIL (right).

3.7 Summary

A multi-characteristic diameter (MCD) pyrolysis model was proposed to simulate biomass gasification processes including devolatilization, drying and charring. The model was described based on a phenomemological mass and energy balance between gas phase and a solid biomass sphere. The devolatilization rate is a function of the solid phase pyrolysis temperature and moisture drying rate depends on the effective size of the characteristic sphere formed by the moisture. Heterogeneous reactions are gas film diffusion controlled which depend on neighboring gas temperature.

The simulation results successfully reproduce the structure formed by different reaction zones commonly seen in experiment: a combustion zone at the lower one-third of the stack overlapping with the gasification zone which extended to the two-third of the stack and followed by the drying/devolatilization zone. At the combustion zone, heterogeneous Char+O_2 and homogeneous CO oxidation are the dominant reactions which are both exothermic. These reactions provide sufficient amount of heat to sustain the gasification in the gasification zone and the dyring/devolatilization zone. There is no significant difference in devolatilization rates between softwoods and hardwood and a constant devolatilization rate is therefore solely determined by the pyrolysis temperature of the wood.

The model successfully predicts the concentrations of CO and CO_2 which agrees with experiment results showing that they are the major species in the synthetic gas produced by biomass gasification. Test simulations also show that synthetic gas is not under equilibrium due to the facts that (1)

heterogeneous reactions are not considered in EQUIL and (2) the species residence times in the gasifier are limited and the system has not reached a fully equilibrium state. Although the H_2 and CH_4 concentrations predicted by MCD model are slightly off, this may caused by the fact that, in the experiments, the preheated air contains moisture and triggered the heterogeneous Char+H_2O reaction which further generate H_2 and CH_4 from water gas shift and methanation reactions.

The model is capable for reproducing experiment results and it demonstrated that the MCD model can be used for predicting the synthetic gas composition of the gasifier at a given design conditions.

Chapter 4
Conclusion and Future Work

4.1 Summary

In this dissertation, a three-dimensional numerical multiphase model for solid waste gasification in a fixed-bed gasifier has been developed. The model is capable for reproducing phenomenological physics inside the gasifier including solid phase pyrolysis, interfacial heat transfer, gas phase reaction and gasification. The results of this work are applicable to (1) gasifier design, (2) biomass utilization and (3) synthetic gas prediction. A summary of this work and major conclusions are presented which are followed by suggestions of future work in this chapter.

4.2 Conclusions

A Computational Model for Non-Charring Solid Pyrolysis in a Fixed-Bed RDF Gasifier

A three-dimensional computational model was developed to simulate flow, heat transfer, pyrolysis and gasification processes inside a fixed-bed waste gasifier for industrial waste recycling applications. The solid-phase waste materials were described by a porous medium incorporated in a single-phase equation. The equations were solved based on SIMPLE algorithm with momentum extrapolation. The Lagrangian pyrolysis model was proposed,

which was described based on a phenomemological vaporization model following the energy balance between gas phase and a solid waste pellet, in which the rate of pyrolysis depends on the effective size of the characteristic waste sphere and the neighboring gas temperature.

Test simulations with different inlet temperature and feeding rate at steady state were studied. The simulation results suggest that, at a higher inlet temperature and lower feeding rate, the stack height decreases and the stack surface becomes more uniform. This reduces the tunneling effect and prevents local oxidation. However, a higher inlet temperature increases the consumption rate of the gaseous fuel from solid pyrolysis and reduces the yield. Nevertheless, with a lower feeding rate, gaseous fuel is nearly fully consumed immediately after it is generated from to solid pyrolysis, leading to a lower yield. These results demonstrated that the model can be used for identifying optimal operating conditions of the gasifier, thereby serving as a valuable tool for the gasifier design and development.

Theoretical Investigation of Charring Solid Gasification in a Fixed-Bed Gasifier

A multi-characteristic diameter (MCD) pyrolysis model was proposed to simulate biomass gasification processes including devolatilization, evaporation and charring. The model was described based on a phenomemological mass and energy balance between gas phase and solid phase biomass spheres. The devolatilization and evaporation rates are considered proportional to the heterogeneous heat transfer rate while devolatilization rate also depends on the volatile content inside the solid.

The devolatilization rate increases as the external heat transfer rate increases and decreases as the volatile content inside the solid reduces. The model predictions were validated with KIER experiments and good agreements are shown.

The model also successfully reproduced the experiment results in that combustion zone, gasification zone and drying/devolatilization zone were captured in a correct order. The major gas composition was also correctly predicted. Test simulations at steady state were compared with equilibrium state, and the results demonstrated that the synthetic gas generated from a finite size gasifier do not reach full equilibrium. Therefore, it is concluded that a sophisticated predictive model as developed in this study is indeed necessary for accurate quantitative prediction of the gasifier performance.

4.3 Contributions

The major contributions of this study are identified as follows:

1. Multiphase flow modeling: the proposed work combines the advantages of conventional Euler-Euler and Euler-Lagrange models by the phenomenological Lagrangian multiple-characteristic pyrolysis model to describe the pyrolysis process of complex multi-component solid materials. The solid phase is represented as a porous continuum (Eulerian) and it is solved together with gas phase (Eulerian). Due to the fact that traditional Euler-Euler schemes are not able to determine local porosity variation inherently, the porosity field is usually specified as an input which remains unchanged throughout the calculation. As an improvement, the proposed model resolves necessary solid phase

information in a Lagrangian scheme and local porosity field can be determined accordingly as a variable. This eliminates the need to solve the solid phase conservation equations for mass and momentum by specifying the velocity field (i.e., the characteristic feeding velocity) externally, considering the slow and simple motion in solid phase. The solid phase energy equation is solved by the energy balance at the solid-gas interface. The proposed model extends the modeling capability to predict the local porosity and pyrolysis field and it is demonstrated as a viable design tool for industrial scale fixed-bed gasifiers.

2. RDF and biomass gasification modeling: most current models rely on empirical relations to determine the solid pyrolysis rate, thus lacking in their capability as a predictive tool. The Lagrangian multiple-characteristic pyrolysis model provides a simple phenomenological approach toward a better quantitative prediction without relying on extensive empirical model constants. In the present model, the pyrolysis rate is directly determined provided the thermodynamics properties of the solid material are known.

3. Charring and noncharring solid pyrolysis: the composition of the material is prescribed and the corresponding characteristic spheres are formed. As the solid material sinks down slowly in the gasifier against the gas oxidizer flow, the solid material experiences pyrolysis processes and three reaction zones are formed inside the gasifier from top to bottom: drying/devolatilization, gasification and combustion. The solid particles leave the gasifier as char if it is a charring material. Otherwise, the solid phase is fully converted into gas phase as synthetic gas. The proposed

model solves both types of materials by specifying their weight percentages and different characteristic spheres to represent the distinct volatility among the charring and non-charring materials. Hence the model is applicable to studying a blend of charring and non-charring material.

4. Bed surface morphology and tunneling effect reduction: Tunneling effect (local oxidization) is one of the major reasons causing a low yield. The thesis investigated the surface morphology under different operation conditions, the causes of tunneling effect and suggested potential means to achieve a uniform bed surface and alleviate the tunneling effect.

5. Heterogeneous and homogeneous reactions: gasification involves a series of important heterogeneous and homogeneous reactions. The Char+O_2 reaction and CO oxidation are the key major exothermic heterogeneous and homogeneous reactions, respectively, providing heat to sustain the system. The thesis adopted semi-global reactions and investigated the role of various species in gasification in order to optimize the synthetic gas composition.

4.4 Future work

Further studies regarding this work can be divided into two categories inclduding (1) new model capabilities and (2) important parametric studies. They are recommended as follows:

New model capabilities:

1. Effects of air injection nozzles inside the gasifier need to be further investigated. The tunneling effect is one of the major causes for a low yield and operation failure of a gasifier. As air injection penetrates further into the stack, a uniform bed surface may be achieved even under high waste feeding rate.

2. Effects of solid particle cracking and fusion need to be further investigated. In this study the solid particles were assumed to be independent and maintain their spherical nature throughout their gasification processes. Solid particles, however, may be subject to crack as the interior pressure builds up due to heating. Further, the solid particles are also possible to agglomerate to form a larger structure, which were neglected in the proposed work.

3. The current model cannot accurately describe another important process called filtration combustion. As shown in the present study, the exothermic reactions occur inside the porous media can store a significant amount of heat on the porous structure and form a self-sustained combustion system without providing significant amount of additional energy. This situation is relevant to low calorific value gases treatments such as the removal of residue fuel in the exhaust pipe or methane in the ventilation air from mines. In the filtration combustion mode, the length scale of the chemical reaction zone (flames) may become comparable to that of the solid pellets, such that the continuous porous medium representation of the solid stack adopted in the present study needs to be modified.

4. The model needs to be improved to describe the gas mixing in porous media. Eddy breakup model is adopted for the homogeneous reactions and the reactions are limited by the mixing rate and this underestimates the CO_2 production rate. The proposed model assumes the mixing inside the porous media is same as the mixing in free flow. The complex structure inside the porous media, however, can increase the mixing rate by promoting transverse dispersion across adjacent streamlines. More study on the gas mixing in porous media is necessary.

Important parametric studies:

1. The model needs to be improved to describe anisotropic permeability. In the thesis, the permeability, *K*, was assumed to be isotropic. However, in a wide range of materials especially biomass, the permeability is anisotropic and this may affect the flow structure significantly. Parametric studies of how tunnels are developed in solids with different anisotropic permeabilities are desired and the study can be applied for pellet designs to minimize the tunnel effects.

2. The model needs to incorporate the description of secondary tar decomposition. The secondary tar decomposition will be less efficient if it is not a downdraft gasifier and certain amount of tar will exist in the synthetic gas. The tar content greatly reduces the quality of the synthetic gas and it will not be able to operate in an internal combustion engine properly and a parametric study on secondary tar decomposition is necessary.

Appendix A

Generalized Conservation Equations

Brackets for all volume-averaged variables have been removed for simplicity. The governing equations are listed as follows

Macroscopic steady gas phase continuity equation in a porous media

$$\frac{\partial}{\partial x_i}\left(\rho u_{Di}\right) = \sum_j \dot{\omega}_{j,pyro} \tag{2-1}$$

Macroscopic steady gas phase momentum equation in a porous media

$$\begin{aligned}\frac{\partial}{\partial x_i}\left(\frac{\rho}{\varphi}u_{Di}u_{Dj}\right) &= -\frac{\partial \varphi p}{\partial x_j} - \frac{2}{3}\frac{\partial}{\partial x_j}\left(\mu\frac{\partial u_{Dk}}{\partial x_k}\right) \\ &+ \frac{\partial}{\partial x_k}\left[\mu\left(\frac{\partial u_{Dj}}{\partial x_k} + \frac{\partial u_{Dk}}{\partial x_j}\right)\right] - \varphi\left(\frac{\mu}{K} + \frac{\rho C_F\sqrt{u_{Dk}u_{Dk}}}{\sqrt{K}}\right)u_{Dj}\end{aligned} \tag{2-2}$$

Macroscopic steady gas phase energy equation

$$\frac{\partial}{\partial x_i}\left(\rho C_p u_{Di} T\right) = \frac{\partial}{\partial x_i}\left(\lambda_{eff}\frac{\partial T}{\partial x_i}\right) + \varphi\dot{q}''' - \frac{hA_s}{V}(T - T_s) + \dot{\omega}_{F,pyro}h_{fg} \tag{2-3}$$

where

$$\lambda_{eff} = \begin{cases}\varphi\lambda & \text{if } T \geq T_{pyro} \\ \varphi\lambda + (1-\varphi)\lambda_s & \text{if } T < T_{pyro}\end{cases}$$

Macroscopic steady species equation

$$\frac{\partial}{\partial x_i}\left(\rho u_{Di} Y_m\right) = \frac{\partial}{\partial x_i}\left(\varphi\rho D \frac{\partial Y_m}{\partial x_i}\right) + \sum\left(\varphi\dot{\omega}_m''' + \dot{\omega}_{m,pyro}\right) \tag{2-4}$$

In order to extend the simulation capability to gasifiers with arbitrary geometries, a linear transformation from the physical domain (x_1, x_2, x_3) into a gemeralized domain (ξ_1, ξ_2, ξ_3) is required for the governing equations.

A steady generalized transport equation in physical domain can be expressed as

$$\frac{\partial}{\partial x_k}\left(\rho u_k \phi\right) = \frac{\partial}{\partial x_j}\left(\Gamma_\phi \frac{\partial \phi}{\partial x_j}\right) + S_\phi \tag{A-1}$$

where ϕ, Γ_ϕ and S_ϕ are general variable, diffusion coefficient and source term, respectively. The general variable can be either a vector or a scalar. For (2-1) – (2-5), their corresponding ϕ, Γ_ϕ and S_ϕ are listed in Table A-1.

Table A-1: Values of ϕ, Γ_ϕ and S_ϕ in the generalized transport equations.

Equation	ϕ	Γ_ϕ	S_ϕ
Continuity (2-1)	1	0	$\sum_j \dot{\omega}_{j,pyro}$
Momentum (2-2)	u_i/φ	μ	$-\frac{\partial \varphi p}{\partial x_j} - \frac{2}{3}\frac{\partial}{\partial x_j}\left(\mu\frac{\partial u_{Dk}}{\partial x_k}\right) + \frac{\partial}{\partial x_k}\left(\mu\frac{\partial u_{Dk}}{\partial x_j}\right)$ $-\varphi\left(\frac{\mu}{K} + \frac{\rho C_F\sqrt{u_{Dk}u_{Dk}}}{\sqrt{K}}\right)u_{Dj}$
Energy (2-3)	C_pT	λ_{eff}	$\varphi\dot{q}''' - \frac{hA_s}{V}(T - T_s) + \dot{\omega}_{F,pyro}h_{fg}$
Species (2-4)	Y_m	$\varphi\rho D$	$S_{Y_\alpha} = \sum_m\left(\varphi\dot{\omega}_m''' + \dot{\omega}_{m,pyro}\right)$

LHS can be transformed as

$$\begin{aligned}\frac{\partial}{\partial x_k}\left(\rho u_k \phi\right) &= \xi_{l,x_k}\frac{\partial}{\partial \xi_l}\left(\rho u_k \phi\right)\\ &= \frac{1}{J}\left[\frac{\partial}{\partial \xi_l}\left(J\xi_{l,x_k}\rho u_k \phi\right) - \rho u_k \phi \frac{\partial}{\partial \xi_l}\left(J\xi_{l,x_k}\right)\right]\\ &= \frac{1}{J}\frac{\partial}{\partial \xi_l}\left(J\xi_{l,x_k}\rho u_k \phi\right)\end{aligned} \tag{A-2}$$

where ξ_{i,x_j} is an abbreviation form for $\frac{\partial \xi_i}{\partial x_j}$ and J is Jacobian matrix and it is defined as

$$J = \frac{\partial\left(x_1, x_2, x_3\right)}{\partial\left(\xi_1, \xi_2, \xi_3\right)} \tag{A-3}$$

Introducing coefficient $\beta_{ij} = J\xi_{i,x_j}$, (A-2) can be expressed as

$$\begin{aligned}\frac{\partial}{\partial x_k}\left(\rho u_k \phi\right) &= \frac{1}{J}\frac{\partial}{\partial \xi_l}\left[\rho\left(J\xi_{l,x_k}u_k\right)\phi\right]\\ &= \frac{1}{J}\frac{\partial}{\partial \xi_l}\left(\rho U_l \phi\right)\end{aligned} \tag{A-4}$$

where U_i is the contravariant velocity $U_i = \beta_{ij}u_j$.
The first term of RHS can also be derived as

$$\begin{aligned}\frac{\partial}{\partial x_j}\left(\Gamma_\phi \frac{\partial \phi}{\partial x_j}\right) &= \xi_{m,x_j}\frac{\partial}{\partial \xi_m}\left(\xi_{n,x_j}\Gamma_\phi \frac{\partial \phi}{\partial \xi_n}\right)\\ &= \frac{1}{J}\left[\frac{\partial}{\partial \xi_m}\left(J\xi_{m,x_j}\xi_{n,x_j}\Gamma_\phi \frac{\partial \phi}{\partial \xi_n}\right) - \xi_{n,x_j}\Gamma_\phi \frac{\partial \phi}{\partial \xi_n}\frac{\partial}{\partial \xi_m}\left(J\xi_{m,x_j}\right)\right]\\ &= \frac{1}{J}\frac{\partial}{\partial \xi_m}\left(J\xi_{m,x_j}\xi_{n,x_j}\Gamma_\phi \frac{\partial \phi}{\partial \xi_n}\right)\end{aligned} \tag{A-5}$$

Introducing C_{ij} as an abbreviation form where $C_{ij} \equiv J\,\xi_{i,x_k}\xi_{j,x_k} = \frac{1}{J}\beta_{ik}\beta_{jk}$, (A-5)

can be further simplified as

$$\begin{aligned}\frac{\partial}{\partial x_j}\left(\Gamma_\phi \frac{\partial \phi}{\partial x_j}\right) &= \frac{1}{J}\frac{\partial}{\partial \xi_m}\left(J\xi_{m,x_j}\xi_{n,x_j}\Gamma_\phi \frac{\partial \phi}{\partial \xi_n}\right) \\ &= \frac{1}{J}\frac{\partial}{\partial \xi_m}\left(C_{mn}\Gamma_\phi \frac{\partial \phi}{\partial \xi_n}\right) \\ &= \frac{1}{J}\frac{\partial}{\partial \xi_m}\left[C_{mm}\Gamma_\phi \frac{\partial \phi}{\partial \xi_m} + (1-\delta_{mn})C_{mn}\Gamma_\phi \frac{\partial \phi}{\partial \xi_n}\right] \\ &= \frac{1}{J}\frac{\partial}{\partial \xi_m}\left(C_{mm}\Gamma_\phi \frac{\partial \phi}{\partial \xi_m}\right) + \frac{1}{J}\frac{\partial}{\partial \xi_m}\left[(1-\delta_{mn})C_{mn}\Gamma_\phi \frac{\partial \phi}{\partial \xi_n}\right]\end{aligned} \tag{A-6}$$

where δ_{mn} is the Kronecker delta function. Combining (A-2)-(A-6), the generalized steady transport equation can be expressed as

$$\frac{1}{J}\frac{\partial}{\partial \xi_l}(\rho U_l \phi) = \frac{1}{J}\frac{\partial}{\partial \xi_m}\left(C_{mm}\Gamma_\phi \frac{\partial \phi}{\partial \xi_m}\right) + \hat{S}_\phi \tag{A-7}$$

where $\hat{S}_\phi \equiv \frac{1}{J}\frac{\partial}{\partial \xi_m}\left[(1-\delta_{mn})C_{mn}\Gamma_\phi \frac{\partial \phi}{\partial \xi_n}\right] + S_\phi$

All source terms are transformed into the generalized coordinate. For continuity equation, there is no spatial derivative term involved and the generalized source term remains unchanged

$$S_\rho = \hat{S}_\rho = \sum_j \dot{\omega}_{j,pyro} \tag{A-8}$$

The source term of momentum equation is

$$\begin{aligned}S_{u_i} = &-\frac{\partial \varphi p}{\partial x_i} - \frac{2}{3}\frac{\partial}{\partial x_i}\left(\mu \frac{\partial u_k}{\partial x_k}\right) + \frac{\partial}{\partial x_j}\left(\mu \frac{\partial u_j}{\partial x_i}\right) \\ &-\delta_\varphi \varphi\left(\frac{\mu}{K} + \frac{\rho C_F}{\sqrt{K}}\sqrt{u_k u_k}\right)u_i\end{aligned} \tag{A-9}$$

The first term of RHS can be generalized as

$$
\begin{aligned}
-\frac{\partial \varphi p}{\partial x_i} &= -\xi_{l,x_i}\frac{\partial \varphi p}{\partial \xi_l} \\
&= -\frac{J\xi_{l,x_i}}{J}\frac{\partial \varphi p}{\partial \xi_l} \\
&= -\frac{\beta_{li}}{J}\frac{\partial \varphi p}{\partial \xi_l}
\end{aligned}
\tag{A-10}
$$

The second term of RHS can be generalized as

$$
\begin{aligned}
-\frac{2}{3}\frac{\partial}{\partial x_i}\left(\mu\frac{\partial u_k}{\partial x_k}\right) &= -\frac{2}{3}\xi_{l,x_i}\frac{\partial}{\partial \xi_l}\left(\mu\frac{\partial u_k}{\partial x_k}\right) \\
&= -\frac{2}{3}\frac{J\xi_{l,x_i}}{J}\frac{\partial}{\partial \xi_l}\left(\mu\frac{\partial u_k}{\partial x_k}\right) \\
&= -\frac{2}{3}\frac{\beta_{li}}{J}\frac{\partial}{\partial \xi_l}\left(\mu\frac{\partial u_k}{\partial x_k}\right)
\end{aligned}
\tag{A-11}
$$

The third term of RHS can be generalized as

$$
\begin{aligned}
\frac{\partial}{\partial x_j}\left(\mu\frac{\partial u_j}{\partial x_i}\right) &= \xi_{m,x_j}\frac{\partial}{\partial \xi_m}\left(\mu\frac{\partial u_j}{\partial x_i}\right) \\
&= \frac{J\xi_{m,x_j}}{J}\frac{\partial}{\partial \xi_m}\left(\mu\frac{\partial u_j}{\partial x_i}\right) \\
&= \frac{\beta_{mj}}{J}\frac{\partial}{\partial \xi_m}\left(\mu\frac{\partial u_j}{\partial x_i}\right)
\end{aligned}
\tag{A-12}
$$

Combining (A-10) to (A-12), the generalized source term for momentum equations can be expressed as

$$
\begin{aligned}
\hat{S}_{u_i} &= \frac{1}{J}\frac{\partial}{\partial \xi_m}\left[\left(1-\delta_{mn}\right)C_{mn}\mu_{eff}\frac{\partial u_i}{\partial \xi_n}\right] + S_{u_i} \\
&= \frac{1}{J}\frac{\partial}{\partial \xi_m}\left[\left(1-\delta_{mn}\right)C_{mn}\mu\frac{\partial u_i}{\partial \xi_n}\right] - \frac{\beta_{li}}{J}\frac{\partial \varphi p}{\partial \xi_l} - \frac{2}{3}\frac{\beta_{li}}{J}\frac{\partial}{\partial \xi_l}\left(\mu\frac{\partial u_k}{\partial x_k}\right) \\
&+ \frac{\beta_{mj}}{J}\frac{\partial}{\partial \xi_m}\left(\mu\frac{\partial u_j}{\partial x_i}\right) - \delta_\varphi\varphi\left(\frac{\mu}{K} + \frac{\rho C_F}{\sqrt{K}}\sqrt{u_k u_k}\right)u_i
\end{aligned}
\tag{A-13}
$$

Energy equation and Species equation, like continuity, there is no spatial derivative term involved and the generalized source terms can be expressed as follows

Energy equation:

$$S_T = \varphi \dot{q}''' - \frac{hA_s}{V}(T - T_s) + \dot{\omega}_{F,pyro} h_{fg} \tag{A-14}$$

$$\begin{aligned} \hat{S}_T &= \frac{1}{J}\frac{\partial}{\partial \xi_m}\left[\left(1 - \delta_{mn}\right) C_{mn} \lambda_{eff} \frac{\partial T}{\partial \xi_n} \right] + S_T \\ &= \frac{1}{J}\frac{\partial}{\partial \xi_m}\left[\left(1 - \delta_{mn}\right) C_{mn} \lambda_{eff} \frac{\partial T}{\partial \xi_n} \right] + \varphi \dot{q}''' - \frac{hA_s}{V}(T - T_s) + \dot{\omega}_{F,pyro} h_{fg} \end{aligned} \tag{A-15}$$

Species equation:

$$S_{Y_\alpha} = \sum_m \left(\varphi \dot{\omega}_m''' + \dot{\omega}_{m,pyro} \right) \tag{A-16}$$

$$\begin{aligned} \therefore \quad \hat{S}_{Y_\alpha} &= \frac{1}{J}\frac{\partial}{\partial \xi_m}\left[\left(1 - \delta_{mn}\right) C_{mn} \left(\rho D_{eff} \right) \frac{\partial Y_\alpha}{\partial \xi_n} \right] + S_{Y_\alpha} \\ &= \frac{1}{J}\frac{\partial}{\partial \xi_m}\left[\left(1 - \delta_{mn}\right) C_{mn} \left(\rho D_{eff} \right) \frac{\partial Y_\alpha}{\partial \xi_n} \right] + \sum_m \left(\varphi \dot{\omega}_m''' + \dot{\omega}_{m,pyro} \right) \end{aligned} \tag{A-17}$$

Appendix B

Discretizations of Conservation Equations

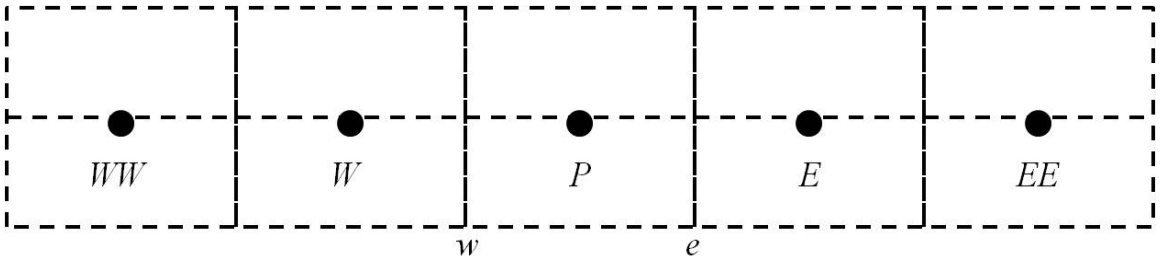

Figure B-1: Discrtization stencil.

Figure B-1 shows the stencil used for discritizations on cell *P*. For illustration purposes, only one-dimension is discussed. *WW*, *W*, *E* and *EE* represent values of the neighboring cells at cell centers. *w* and *e* represent values at the cell surfaces between *W* and *P*, and *P* and *E*, respectively.

In this thesis, control volume method is applied and any property ϕ (either a vector or a scalar) on a generalized control surface is determined by the neighboring cells depending on the direction of the flow:

$$\phi_w = \begin{cases} \phi_w^+ = c_{WW}^{w+}\phi_{WW} + c_W^{w+}\phi_W + c_P^{w+}\phi_P & \text{for } u_w \geq 0 \\ \phi_w^- = c_W^{w-}\phi_W + c_P^{w-}\phi_P + c_E^{w-}\phi_E & \text{for } u_w < 0 \end{cases} \tag{B-1a}$$

$$\phi_e = \begin{cases} \phi_e^+ = c_W^{e+}\phi_W + c_P^{e+}\phi_P + c_E^{e+}\phi_E & \text{for } u_e \geq 0 \\ \phi_e^- = c_P^{e-}\phi_P + c_E^{e-}\phi_E + c_{EE}^{e-}\phi_{EE} & \text{for } u_e < 0 \end{cases} \tag{B-1b}$$

where *C*'s are the weighting coefficients for the values on the cells specified by the subscripts. Superscripts *w* and *e*, specify the weighting coefficient is for the value at the surfaces between cell *W* and *P*, and surfaces between cell *P* and *E*, respectively. + and – refer to the flow direction, + is positive and – is negative.

(B-1) can be rearranged as follows for formulation optimization (Patankar,1980; Hayase *et al.*, 1992).

$$\phi_e = \begin{cases} \phi_e^+ = a_1\phi_W + a_2\phi_P + a_3\phi_E + S_e^+ & \text{for } u_e \geq 0 \\ \phi_e^- = b_3\phi_W + b_2\phi_P + b_1\phi_E + S_e^- & \text{for } u_e < 0 \end{cases} \tag{B-2a}$$

where $\begin{cases} S_e^+ = \left(c_W^{e+} - a_1\right)\phi_W + \left(c_P^{e+} - a_2\right)\phi_P + \left(c_E^{e+} - a_3\right)\phi_E \\ S_e^- = -b_3\phi_W + \left(c_P^{e-} - b_2\right)\phi_P + \left(c_E^{e-} - b_1\right)\phi_E + c_{EE}^{e-}\phi_{EE} \end{cases}$

$$\phi_w = \begin{cases} \phi_w^+ = b_1\phi_W + b_2\phi_P + b_3\phi_E + S_w^+ & \text{for } u_w \geq 0 \\ \phi_w^- = a_3\phi_W + a_2\phi_P + a_1\phi_E + S_w^- & \text{for } u_w < 0 \end{cases} \tag{B-2b}$$

where $\begin{cases} S_w^+ = c_{WW}^{w+}\phi_{WW} + \left(c_W^{w+} - b_1\right)\phi_W + \left(c_P^{w+} - b_2\right)\phi_P - b_3\phi_E \\ S_w^- = \left(c_W^{w-} - a_3\right)\phi_W + \left(c_P^{w-} - a_2\right)\phi_P + \left(c_E^{w-} - a_1\right)\phi_E \end{cases}$

Discretized the general conservation equation yield

$$\left(F_e^+\phi_e^+ + F_e^-\phi_e^-\right) - \left(F_w^+\phi_w^+ + F_w^-\phi_w^-\right) = D_e\left(\phi_E - \phi_P\right) - D_w\left(\phi_P - \phi_W\right) + S \tag{B-3}$$

where *F* and *D* are flux term due to advection and diffusion, respectively. *S* is the source term. F and D, based on different flow direction, can be expressed as

$$F_w^+ = \begin{cases} \rho_w u_w & \left(u_w > 0\right) \\ 0 & \left(u_w \leq 0\right) \end{cases};\ F_w^- = \begin{cases} 0 & \left(u_e \geq 0\right) \\ \rho_w u_w & \left(u_e < 0\right) \end{cases} \tag{B-4a}$$

$$F_e^+ = \begin{cases} \rho_e u_e & (u_e > 0) \\ 0 & (u_e \le 0) \end{cases};\ F_e^- = \begin{cases} 0 & (u_e \ge 0) \\ \rho_e u_e & (u_e < 0) \end{cases} \tag{B-4b}$$

$$D_e = \Gamma_{\phi,e};\ D_e = \Gamma_{\phi,e} \tag{B-4c}$$

For example, a discretized continuity equation without mass generation/destruction can be expressed as

$$\left(F_e^+ + F_e^-\right) - \left(F_w^+ + F_w^-\right) = 0 \tag{B-5}$$

Substituting values at control surfaces into conservation equation yields

$$A_P \phi_P = A_E \phi_E + A_W \phi_W + B \tag{B-6}$$

where

$$A_P = a_2 F_e^+ + b_2 F_e^- - b_2 F_w^+ - a_2 F_w^- + \left(D_e + D_w\right)$$

$$A_E = -a_3 F_e^+ - b_1 F_e^- + b_3 F_w^+ + a_1 F_w^- + D_e$$

$$A_W = -a_1 F_e^+ - b_3 F_e^- + b_1 F_w^+ + a_3 F_w^- + D_w$$

$$B = -S_e^+ F_e^+ - S_e^- F_e^- + S_w^+ F_w^+ + S_w^- F_w^-$$

In the thesis, hybrid scheme is adopted. Hybrid scheme was developed by Spalding (Spalding, 1972), which is a Péclet-number-weighted scheme between central difference and the upwind schemes. Compared with upwind scheme, which only introduces information at upstream, the major advantage of the hybrid scheme is that it can adequately introduce information at the downstream if there is a diffusion flux passing against the advection

direction when the diffusion effects are significant. For hybrid scheme, the values at the control surfaces can be expressed as

$$\phi_e = \begin{cases} \phi_e^+ = \phi_P + \dfrac{\| 0,\ (1-|Pe_e|/2) \|}{1-|Pe_e|/2} \dfrac{\phi_E - \phi_P}{2} & \text{for } u_e \geq 0 \\ \phi_e^- = \phi_E + \dfrac{\| 0,\ (1-|Pe_e|/2) \|}{1-|Pe_e|/2} \dfrac{\phi_P - \phi_E}{2} & \text{for } u_e < 0 \end{cases} \tag{B-7a}$$

$$\phi_w = \begin{cases} \phi_w^+ = \phi_W + \dfrac{\| 0,\ (1-|Pe_w|/2) \|}{1-|Pe_w|/2} \dfrac{\phi_P - \phi_W}{2} & \text{for } u_w \geq 0 \\ \phi_w^- = \phi_P + \dfrac{\| 0,\ (1-|Pe_w|/2) \|}{1-|Pe_w|/2} \dfrac{\phi_W - \phi_P}{2} & \text{for } u_w < 0 \end{cases} \tag{B-7b}$$

where $\| a\ ,\ b \|$ represents the greater value among a and b. For formula optimization purpose, (B-7a) and (B-7d) can be rewritten as

$$\phi_e = \begin{cases} \phi_e^+ = \phi_P + S_e^+ & \text{for } u_e \geq 0 \\ \phi_e^- = \phi_E + S_e^- & \text{for } u_e < 0 \end{cases} \tag{B-8a}$$

where $\begin{cases} S_e^+ = \dfrac{\| 0,\ (1-|Pe_e|/2) \|}{1-|Pe_e|/2} \dfrac{\phi_E - \phi_P}{2} \\ S_e^- = \dfrac{\| 0,\ (1-|Pe_e|/2) \|}{1-|Pe_e|/2} \dfrac{\phi_P - \phi_E}{2} \end{cases}$

$$\phi_w = \begin{cases} \phi_w^+ = \phi_W + S_w^+ & \text{for } u_w \geq 0 \\ \phi_w^- = \phi_P + S_w^- & \text{for } u_w < 0 \end{cases} \tag{B-8b}$$

$$\text{where} \begin{cases} S_w^+ = \dfrac{\left\| 0,\ \left(1-\left|Pe_w\right|/2\right)\right\|}{1-\left|Pe_w\right|/2}\ \dfrac{\phi_P-\phi_W}{2} \\ S_w^- = \dfrac{\left\| 0,\ \left(1-\left|Pe_w\right|/2\right)\right\|}{1-\left|Pe_w\right|/2}\ \dfrac{\phi_W-\phi_P}{2} \end{cases}$$

In a three-dimensional space in the physical domain, the volume of a cell spanned by vector $d\vec{x}_1$, $d\vec{x}_2$ and $d\vec{x}_3$ can be calculated by their determinant

$$\begin{aligned} d\mathscr{V} &= d\vec{x}_1 \cdot \left(d\vec{x}_2 \times d\vec{x}_3\right) \\ &= \varepsilon_{ijk} x_{i,\xi_1} d\xi_1 \cdot x_{j,\xi_2} d\xi_2 \cdot x_{k,\xi_3} d\xi_3 \\ &= \left(\varepsilon_{ijk} x_{i,\xi_1} x_{j,\xi_2} x_{k,\xi_3}\right)\ d\xi_1 d\xi_2 d\xi_3 \\ &= J\ d\xi_1 d\xi_2 d\xi_3 \\ &= J \end{aligned} \tag{B-9}$$

where $\Delta\xi_i = 1$ in the generalized coordinate.

Recall (A-7), the generalized governing equation is

$$\frac{1}{J}\frac{\partial}{\partial\xi_l}\left(\rho U_l \phi\right) - \frac{1}{J}\frac{\partial}{\partial\xi_m}\left(C_{mm}\Gamma_\phi \frac{\partial\phi}{\partial\xi_m}\right) = \hat{S}_\phi \tag{A-7}$$

Integrating over the cell and applying (B-9) yield

$$\begin{aligned} &\left(F_e\phi_e - F_w\phi_w\right) + \left(F_n\phi_n - F_s\phi_s\right) + \left(F_t\phi_t - F_b\phi_b\right) \\ &-D_{11,e}\left(\phi_E - \phi_P\right) + D_{11,w}\left(\phi_P - \phi_W\right) \\ &-D_{22,n}\left(\phi_N - \phi_P\right) + D_{22,s}\left(\phi_P - \phi_S\right) \\ &-D_{33,t}\left(\phi_T - \phi_P\right) + D_{33,b}\left(\phi_P - \phi_B\right) = \bar{S}_\phi \end{aligned} \tag{B-10}$$

where

$$F = \rho U$$

$$D_{ij} = C_{ij}\Gamma_{\phi}$$

$$\overline{S}_{\phi} \equiv \int \hat{S}_{\phi} d\mathscr{V}$$

Substituting (B-8a) and (B-8b) into (B-10) yield

$$\begin{aligned}
&F_e^+\left(\phi_P + S_e^+\right) + F_e^-\left(\phi_E + S_e^-\right) - F_w^+\left(\phi_W + S_w^+\right) - F_w^-\left(\phi_P + S_w^-\right) + \\
&F_n^+\left(\phi_P + S_n^+\right) + F_n^-\left(\phi_N + S_n^-\right) - F_s^+\left(\phi_S + S_s^+\right) - F_s^-\left(\phi_P + S_s^-\right) + \\
&F_t^+\left(\phi_P + S_t^+\right) + F_t^-\left(\phi_T + S_t^-\right) - F_b^+ - \left(\phi_B + S_b^+\right) - F_b^-\left(\phi_P + S_b^-\right) - \\
&D_{11,e}\left(\phi_E - \phi_P\right) + D_{11,w}\left(\phi_P - \phi_W\right) - \\
&D_{22,n}\left(\phi_N - \phi_P\right) + D_{22,s}\left(\phi_P - \phi_S\right) - \\
&D_{33,t}\left(\phi_T - \phi_P\right) + D_{33,b}\left(\phi_P - \phi_B\right) \\
&= \overline{S}_{\phi}
\end{aligned} \tag{B-11}$$

From (B-11), steady continuity equation can be rewritten as

$$\begin{aligned}
&\left(F_e^+ + F_e^- - F_w^+ - F_w^-\right) + \\
&\left(F_n^+ + F_n^- - F_s^+ - F_s^-\right) + \\
&\left(F_t^+ + F_t^- - F_b^+ - F_b^-\right) \\
&= \overline{S}_{\rho}
\end{aligned} \tag{B-12}$$

where $\overline{S}_{\rho} = \int \hat{S}_{\rho} d\mathscr{V}$.

Multiply ϕ_P to (B-12) and subtract from (B-11), it yields

$$
\begin{aligned}
&F_e^+\left(S_e^+\right)+F_e^-\left(\phi_E+S_e^--\phi_p\right)-F_w^+\left(\phi_W+S_w^+-\phi_P\right)-F_w^-\left(S_w^-\right)+\\
&F_n^+\left(S_n^+\right)+F_n^-\left(\phi_N+S_n^--\phi_P\right)-F_s^+\left(\phi_S+S_s^+-\phi_P\right)-F_s^-\left(S_s^-\right)+\\
&F_t^+\left(S_t^+\right)+F_t^-\left(\phi_T+S_t^--\phi_P\right)-F_b^+-\left(\phi_B+S_b^+-\phi_P\right)-F_b^-\left(S_b^-\right)-\\
&D_{11,e}\left(\phi_E-\phi_P\right)+D_{11,w}\left(\phi_P-\phi_W\right)-\\
&D_{22,n}\left(\phi_N-\phi_P\right)+D_{22,s}\left(\phi_P-\phi_S\right)-\\
&D_{33,t}\left(\phi_T-\phi_P\right)+D_{33,b}\left(\phi_P-\phi_B\right)\\
&=\overline{S}_\phi-\phi_P\overline{S}_\rho
\end{aligned}
\tag{B-13}
$$

(B-13) can be rewritten as

$$
\begin{aligned}
&\phi_p\left(-F_e^-+F_w^+-F_n^-+F_s^+-F_t^-+F_b^+-D_{11,e}+D_{11,w}-D_{22,n}+D_{22,s}-D_{33,t}+D_{33,b}\right)+\\
&\phi_E\left(F_e^--D_{11,e}\right)+\phi_W\left(-F_w^+-D_{11,w}\right)+\phi_N\left(F_n^--D_{22,n}\right)+\phi_S\left(-F_s^+-D_{22,s}\right)+\\
&\phi_T\left(F_t^--D_{33,t}\right)+\phi_B\left(-F_b^+-D_{33,b}\right)+F_e^+S_e^++F_e^-S_e^--F_w^+S_w^+-F_w^-S_w^-+\\
&F_n^+S_n^++F_n^-S_n^--F_s^+S_s^+-F_s^-S_s^-+F_t^+S_t^++F_t^-S_t^--F_b^+S_b^+-F_b^-S_b^-\\
&=\overline{S}_\phi-\phi_P\overline{S}_\rho
\end{aligned}
\tag{B-14}
$$

Rearrange (B-14) and the discretized general conservation equation can be expressed in the form of

$$
a_P\phi_P=\sum a_{nb}\phi_{nb}+b_P \tag{B-15}
$$

where

$$
a_W=F_w^++D_{11,w}
$$

$$
a_E=-F_e^-+D_{11,e}
$$

$$
a_S=F_s^++D_{22,s}
$$

$$
a_N=-F_n^-+D_{22,n}
$$

$$
a_B=F_b^++D_{33,b}
$$

$$a_T = -F_t^- + D_{33,t}$$

$$a_P = a_W + a_E + a_S + a_N + a_B + a_T$$

and source term b_p can be expressed as

$$b_P = S_{scheme} + \overline{S}_\phi \tag{B-16}$$

where S_{scheme} is the additional source term resulting from distritization and

$$\begin{aligned} S_{scheme} = & -F_e^+ S_e^+ - F_e^- S_e^- + F_w^+ S_w^+ + F_w^- S_w^- \\ & - F_n^+ S_n^+ - F_n^- S_n^- + F_s^+ S_s^+ + F_s^- S_s^- \\ & - F_t^+ S_t^+ - F_t^- S_t^- + F_b^+ S_b^+ + F_b^- S_b^- \end{aligned} \tag{B-17}$$

Appendix C

Apply Low-Reynolds Number Turbulent *k*-ε Model onto the Generalized Coordinate System

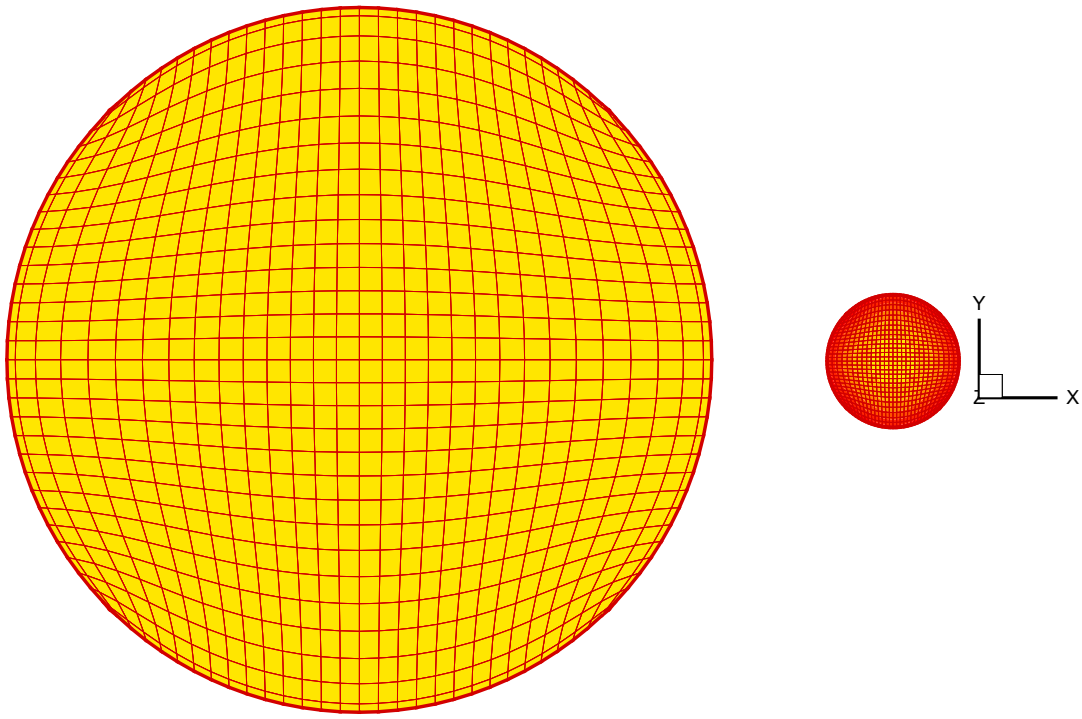

Figure C-1: The cross sectional views of the top surface (left) and bottom surface (right).

When the stack height decreases, the flow will experience less drag exerted by the porous media and result in higher momentum. The flow therefore is subject to become turbulent and, to extend the simulation capability, turbulent model is necessary. Figure C-1 shows the cross sections views of

the grid at the top and bottom surfaces in a real ratio. The grid distribution in the inlet duck is more condensed than the one in the main chamber and, as a result, the wall function become inappropriate because

1. Wall function requires the first grid from the wall locates between $30 > y^+ > 200$ and the discrepancy among these two regions generally won't satisfy this condition.
2. Grid independent test becomes difficult under the constrain $30 > y^+ > 200$.

A better choice will be, instead of applying the standard wall function, applying low-Reynolds number k-ε turbulent model since it doesn't require any near wall treatment.

Turbulence models which are valid throughout the laminar, semi-laminar, and fully turbulent regions have been studied intensively in the near fifty years. Glushko (1965) and Wolfshtein (1969) worked with one-equation turbulence models. Jones and Launder (1972, 1973) extended the k-ε model to low-Reynolds-number flows and the corresponding k-ε equation sets are

$$\frac{\partial}{\partial x_k}\left(\rho u_k k\right) = \frac{\partial}{\partial x_j}\left[\left(\mu + \mu_t\right)\frac{\partial k}{\partial x_j}\right] + \mu_t \frac{\partial u_i}{\partial x_j}\left(\frac{\partial u_i}{\partial x_j} + \frac{\partial u_j}{\partial x_i}\right) - \rho\varepsilon - 2\mu\left(\frac{\partial \sqrt{k}}{\partial x_j}\right)\left(\frac{\partial \sqrt{k}}{\partial x_j}\right) \quad (3\text{-}2)$$

where k, ε are the turbulent kinetic energy and turbulent dissipation [m^2/s^3] rate [m^2/s^2]. μ_t is the turbulent viscosity defined as

$$\mu_t = C_\mu \rho \frac{k^2}{\varepsilon} \quad (3\text{-}3)$$

where $C_\mu = C_{\mu\infty}\exp\left[-2.5/(1.0 + \mathrm{Re}_t/50)\right]$ and constant $C_{\mu\infty} = 0.09$. Re_t is the turbulent Reynolds number and it is defined as

$$\mathrm{Re}_t = \frac{k^2}{\nu\varepsilon} \tag{3-4}$$

where ν is the dynamics viscosity. The turbulent kinetic energy equation is similar to the standard high Reynolds number once except the last term on the RHS. There is no physical argument but it serves as a correction source which accords the model prediction to the experiment (Jones *et al*., 1972).

Macroscopic steady turbulent dissipation rate equation

$$\begin{aligned}\frac{\partial}{\partial x_k}\left(\rho u_k \varepsilon\right) = \frac{\partial}{\partial x_j}\left[\left(\frac{\mu_t}{\sigma_\varepsilon}+\mu\right)\frac{\partial \varepsilon}{\partial x_j}\right] + \frac{\varepsilon}{k}\left[C_{\varepsilon 1}\mu_t \frac{\partial u_i}{\partial x_j}\left(\frac{\partial u_i}{\partial x_j}+\frac{\partial u_j}{\partial x_i}\right) - C_{\varepsilon 2}\rho\varepsilon\right] \\ + 2\frac{\mu\mu_t}{\rho}\left(\frac{\partial^2 u_i}{\partial x_j \partial x_l}\right)\left(\frac{\partial^2 u_i}{\partial x_j \partial x_l}\right)\end{aligned} \tag{3-5}$$

where

$$\begin{aligned}\sigma_\varepsilon &= 1.3 \\ C_{\varepsilon 1} &= 1.44 \\ C_{\varepsilon 2} &= C_{\varepsilon 2\infty}\left[1.0 - 0.3\exp(-\mathrm{Re}_t^2)\right] \\ C_{\varepsilon 2\infty} &= 1.92\end{aligned} \tag{3-6}$$

The additional source term in (3-2) has been introduced for computational rather than physical reasons. By introducing this additional term, the dissipation rate, ε, may therefore be interrupted as the isotropic part instead of the total dissipation rate. This enables the possibility of defining the boundary condition for ε as zero at the wall since the isotropic part of the dissipation rate vanishes and the additional term reduces to the non-isotropic dissipation rate at the wall. For the additional term in (3-5), however, no physical reason was provided. Its inclusion is simply due to the fact that without it the peak level of turbulence kinetic energy at $y^+ \approx 20$ did not

accord with experiment (Jones *et al.*, 1971). By introducing the two additional source term in (C-1) and (C-2), the turbulent model can be applied in all laminar, semi-laminar, and fully turbulent regions and the wall function, therefore, is no longer required.

$2\mu\left(\frac{\partial\sqrt{k}}{\partial x_j}\right)\left(\frac{\partial\sqrt{k}}{\partial x_j}\right)$ can be transformed into generalized coordinate as

$$\begin{aligned} & 2\mu\left(\frac{\partial\sqrt{k}}{\partial x_j}\right)\left(\frac{\partial\sqrt{k}}{\partial x_j}\right) \\ &= 2\mu\xi_{i,x_j}\frac{\partial\sqrt{k}}{\partial\xi_i}\xi_{l,x_j}\frac{\partial\sqrt{k}}{\partial\xi_l} \\ &= \frac{2\mu}{J}\left(J\xi_{i,x_j}\xi_{l,x_j}\right)\frac{\partial\sqrt{k}}{\partial\xi_i}\frac{\partial\sqrt{k}}{\partial\xi_l} \\ &= \frac{2\mu C_{il}}{J}\frac{\partial\sqrt{k}}{\partial\xi_i}\frac{\partial\sqrt{k}}{\partial\xi_l} \end{aligned} \tag{C-1a}$$

Unfolding the tensor term yields

$$\begin{aligned} & 2\mu\left(\frac{\partial\sqrt{k}}{\partial x_j}\right)\left(\frac{\partial\sqrt{k}}{\partial x_j}\right) \\ &= \frac{2\mu}{J}\left[C_{11}\frac{\partial\sqrt{k}}{\partial\xi_1}\frac{\partial\sqrt{k}}{\partial\xi_1}+C_{21}\frac{\partial\sqrt{k}}{\partial\xi_2}\frac{\partial\sqrt{k}}{\partial\xi_1}+C_{31}\frac{\partial\sqrt{k}}{\partial\xi_3}\frac{\partial\sqrt{k}}{\partial\xi_1}\right. \\ &\quad + C_{12}\frac{\partial\sqrt{k}}{\partial\xi_1}\frac{\partial\sqrt{k}}{\partial\xi_2}+C_{22}\frac{\partial\sqrt{k}}{\partial\xi_2}\frac{\partial\sqrt{k}}{\partial\xi_2}+C_{32}\frac{\partial\sqrt{k}}{\partial\xi_3}\frac{\partial\sqrt{k}}{\partial\xi_2} \\ &\quad \left.+C_{13}\frac{\partial\sqrt{k}}{\partial\xi_1}\frac{\partial\sqrt{k}}{\partial\xi_3}+C_{23}\frac{\partial\sqrt{k}}{\partial\xi_2}\frac{\partial\sqrt{k}}{\partial\xi_3}+C_{33}\frac{\partial\sqrt{k}}{\partial\xi_3}\frac{\partial\sqrt{k}}{\partial\xi_3}\right] \end{aligned} \tag{C-1b}$$

and (C-1b) can be rewritten as

$$
\begin{aligned}
&= \frac{2\mu}{J}\left[C_{11}\left(\frac{\partial\sqrt{k}}{\partial\xi_1}\right)^2 + C_{22}\left(\frac{\partial\sqrt{k}}{\partial\xi_2}\right)^2 + C_{33}\left(\frac{\partial\sqrt{k}}{\partial\xi_3}\right)^2 \right. \\
&\left. + \left(C_{12}+C_{21}\right)\frac{\partial\sqrt{k}}{\partial\xi_1}\frac{\partial\sqrt{k}}{\partial\xi_2} + \left(C_{23}+C_{32}\right)\frac{\partial\sqrt{k}}{\partial\xi_3}\frac{\partial\sqrt{k}}{\partial\xi_2} + \left(C_{13}+C_{31}\right)\frac{\partial\sqrt{k}}{\partial\xi_1}\frac{\partial\sqrt{k}}{\partial\xi_3} \right] \\
&= \frac{2\mu}{J}\left[C_{11}\left(\sqrt{k}_e - \sqrt{k}_w\right)^2 + C_{22}\left(\sqrt{k}_n - \sqrt{k}_s\right)^2 + C_{33}\left(\sqrt{k}_t - \sqrt{k}_b\right)^2 \right. \\
&+ \left(C_{12}+C_{21}\right)\left(\sqrt{k}_e - \sqrt{k}_w\right)\left(\sqrt{k}_n - \sqrt{k}_s\right) \\
&+ \left(C_{23}+C_{32}\right)\left(\sqrt{k}_n - \sqrt{k}_s\right)\left(\sqrt{k}_t - \sqrt{k}_b\right) \\
&\left. + \left(C_{13}+C_{31}\right)\left(\sqrt{k}_e - \sqrt{k}_w\right)\left(\sqrt{k}_t - \sqrt{k}_b\right) \right]
\end{aligned}
\qquad \text{(C-1c)}
$$

Likewise, $2\frac{\mu\mu_t}{\rho}\left(\frac{\partial u_i}{\partial x_j \partial x_l}\right)\left(\frac{\partial u_i}{\partial x_j \partial x_l}\right)$ can be transformed into generalized coordinate as

$$
\begin{aligned}
\left(\frac{\partial^2 u_i}{\partial x_j \partial x_l}\right)\left(\frac{\partial^2 u_i}{\partial x_j \partial x_l}\right) &= \frac{\partial}{\partial x_j}\left(\frac{\partial u_i}{\partial x_l}\right)\frac{\partial}{\partial x_j}\left(\frac{\partial u_i}{\partial x_l}\right) \\
&= \xi_{m,x_j}\frac{\partial}{\partial \xi_m}\left(\frac{\partial u_i}{\partial x_l}\right)\xi_{n,x_j}\frac{\partial}{\partial \xi_n}\left(\frac{\partial u_i}{\partial x_l}\right) \\
&= \frac{C_{mn}}{J}\frac{\partial}{\partial \xi_m}\left(\frac{\partial u_i}{\partial x_l}\right)\frac{\partial}{\partial \xi_n}\left(\frac{\partial u_i}{\partial x_l}\right)
\end{aligned}
\qquad \text{(C-2a)}
$$

Unfolding the tensor term yields

$$
\begin{aligned}
&2\frac{\mu\mu_t}{\rho}\left(\frac{\partial u_i}{\partial x_j \partial x_l}\right)\left(\frac{\partial u_i}{\partial x_j \partial x_l}\right) \\
&= \frac{1}{J}\left\{ C_{11}\left[\frac{\partial}{\partial\xi_1}\left(\frac{\partial u_1}{\partial x_1}\right)\frac{\partial}{\partial\xi_1}\left(\frac{\partial u_1}{\partial x_1}\right) + \frac{\partial}{\partial\xi_1}\left(\frac{\partial u_2}{\partial x_1}\right)\frac{\partial}{\partial\xi_1}\left(\frac{\partial u_2}{\partial x_1}\right) + \frac{\partial}{\partial\xi_1}\left(\frac{\partial u_3}{\partial x_1}\right)\frac{\partial}{\partial\xi_1}\left(\frac{\partial u_3}{\partial x_1}\right) \right. \right. \\
&\quad + \frac{\partial}{\partial\xi_1}\left(\frac{\partial u_1}{\partial x_2}\right)\frac{\partial}{\partial\xi_1}\left(\frac{\partial u_1}{\partial x_2}\right) + \frac{\partial}{\partial\xi_1}\left(\frac{\partial u_2}{\partial x_2}\right)\frac{\partial}{\partial\xi_1}\left(\frac{\partial u_2}{\partial x_2}\right) + \frac{\partial}{\partial\xi_1}\left(\frac{\partial u_3}{\partial x_2}\right)\frac{\partial}{\partial\xi_1}\left(\frac{\partial u_3}{\partial x_2}\right) \\
&\quad \left. \left. + \frac{\partial}{\partial\xi_1}\left(\frac{\partial u_1}{\partial x_3}\right)\frac{\partial}{\partial\xi_1}\left(\frac{\partial u_1}{\partial x_3}\right) + \frac{\partial}{\partial\xi_1}\left(\frac{\partial u_2}{\partial x_3}\right)\frac{\partial}{\partial\xi_1}\left(\frac{\partial u_2}{\partial x_3}\right) + \frac{\partial}{\partial\xi_1}\left(\frac{\partial u_3}{\partial x_3}\right)\frac{\partial}{\partial\xi_1}\left(\frac{\partial u_3}{\partial x_3}\right) \right] \right.
\end{aligned}
\qquad \text{(C-2b)}
$$

$$
\begin{aligned}
&+C_{21}\left[\frac{\partial}{\partial\xi_2}\left(\frac{\partial u_1}{\partial x_1}\right)\frac{\partial}{\partial\xi_1}\left(\frac{\partial u_1}{\partial x_1}\right)+\frac{\partial}{\partial\xi_2}\left(\frac{\partial u_2}{\partial x_1}\right)\frac{\partial}{\partial\xi_1}\left(\frac{\partial u_2}{\partial x_1}\right)+\frac{\partial}{\partial\xi_2}\left(\frac{\partial u_3}{\partial x_1}\right)\frac{\partial}{\partial\xi_1}\left(\frac{\partial u_3}{\partial x_1}\right)\right.\\
&\quad+\frac{\partial}{\partial\xi_2}\left(\frac{\partial u_1}{\partial x_2}\right)\frac{\partial}{\partial\xi_1}\left(\frac{\partial u_1}{\partial x_2}\right)+\frac{\partial}{\partial\xi_2}\left(\frac{\partial u_2}{\partial x_2}\right)\frac{\partial}{\partial\xi_1}\left(\frac{\partial u_2}{\partial x_2}\right)+\frac{\partial}{\partial\xi_2}\left(\frac{\partial u_3}{\partial x_2}\right)\frac{\partial}{\partial\xi_1}\left(\frac{\partial u_3}{\partial x_2}\right)\\
&\quad\left.+\frac{\partial}{\partial\xi_2}\left(\frac{\partial u_1}{\partial x_3}\right)\frac{\partial}{\partial\xi_1}\left(\frac{\partial u_1}{\partial x_3}\right)+\frac{\partial}{\partial\xi_2}\left(\frac{\partial u_2}{\partial x_3}\right)\frac{\partial}{\partial\xi_1}\left(\frac{\partial u_2}{\partial x_3}\right)+\frac{\partial}{\partial\xi_2}\left(\frac{\partial u_3}{\partial x_3}\right)\frac{\partial}{\partial\xi_1}\left(\frac{\partial u_3}{\partial x_3}\right)\right]\\
&+C_{31}\left[\frac{\partial}{\partial\xi_3}\left(\frac{\partial u_1}{\partial x_1}\right)\frac{\partial}{\partial\xi_1}\left(\frac{\partial u_1}{\partial x_1}\right)+\frac{\partial}{\partial\xi_3}\left(\frac{\partial u_2}{\partial x_1}\right)\frac{\partial}{\partial\xi_1}\left(\frac{\partial u_2}{\partial x_1}\right)+\frac{\partial}{\partial\xi_3}\left(\frac{\partial u_3}{\partial x_1}\right)\frac{\partial}{\partial\xi_1}\left(\frac{\partial u_3}{\partial x_1}\right)\right.\\
&\quad+\frac{\partial}{\partial\xi_3}\left(\frac{\partial u_1}{\partial x_2}\right)\frac{\partial}{\partial\xi_1}\left(\frac{\partial u_1}{\partial x_2}\right)+\frac{\partial}{\partial\xi_3}\left(\frac{\partial u_2}{\partial x_2}\right)\frac{\partial}{\partial\xi_1}\left(\frac{\partial u_2}{\partial x_2}\right)+\frac{\partial}{\partial\xi_3}\left(\frac{\partial u_3}{\partial x_2}\right)\frac{\partial}{\partial\xi_1}\left(\frac{\partial u_3}{\partial x_2}\right)\\
&\quad\left.+\frac{\partial}{\partial\xi_3}\left(\frac{\partial u_1}{\partial x_3}\right)\frac{\partial}{\partial\xi_1}\left(\frac{\partial u_1}{\partial x_3}\right)+\frac{\partial}{\partial\xi_3}\left(\frac{\partial u_2}{\partial x_3}\right)\frac{\partial}{\partial\xi_1}\left(\frac{\partial u_2}{\partial x_3}\right)+\frac{\partial}{\partial\xi_3}\left(\frac{\partial u_3}{\partial x_3}\right)\frac{\partial}{\partial\xi_1}\left(\frac{\partial u_3}{\partial x_3}\right)\right]\\
&+C_{12}\left[\frac{\partial}{\partial\xi_1}\left(\frac{\partial u_1}{\partial x_1}\right)\frac{\partial}{\partial\xi_2}\left(\frac{\partial u_1}{\partial x_1}\right)+\frac{\partial}{\partial\xi_1}\left(\frac{\partial u_2}{\partial x_1}\right)\frac{\partial}{\partial\xi_2}\left(\frac{\partial u_2}{\partial x_1}\right)+\frac{\partial}{\partial\xi_1}\left(\frac{\partial u_3}{\partial x_1}\right)\frac{\partial}{\partial\xi_2}\left(\frac{\partial u_3}{\partial x_1}\right)\right.\\
&\quad+\frac{\partial}{\partial\xi_1}\left(\frac{\partial u_1}{\partial x_2}\right)\frac{\partial}{\partial\xi_2}\left(\frac{\partial u_1}{\partial x_2}\right)+\frac{\partial}{\partial\xi_1}\left(\frac{\partial u_2}{\partial x_2}\right)\frac{\partial}{\partial\xi_2}\left(\frac{\partial u_2}{\partial x_2}\right)+\frac{\partial}{\partial\xi_1}\left(\frac{\partial u_3}{\partial x_2}\right)\frac{\partial}{\partial\xi_2}\left(\frac{\partial u_3}{\partial x_2}\right)\\
&\quad\left.+\frac{\partial}{\partial\xi_1}\left(\frac{\partial u_1}{\partial x_3}\right)\frac{\partial}{\partial\xi_2}\left(\frac{\partial u_1}{\partial x_3}\right)+\frac{\partial}{\partial\xi_1}\left(\frac{\partial u_2}{\partial x_3}\right)\frac{\partial}{\partial\xi_2}\left(\frac{\partial u_2}{\partial x_3}\right)+\frac{\partial}{\partial\xi_1}\left(\frac{\partial u_3}{\partial x_3}\right)\frac{\partial}{\partial\xi_2}\left(\frac{\partial u_3}{\partial x_3}\right)\right]\\
&+C_{22}\left[\frac{\partial}{\partial\xi_2}\left(\frac{\partial u_1}{\partial x_1}\right)\frac{\partial}{\partial\xi_2}\left(\frac{\partial u_1}{\partial x_1}\right)+\frac{\partial}{\partial\xi_2}\left(\frac{\partial u_2}{\partial x_1}\right)\frac{\partial}{\partial\xi_2}\left(\frac{\partial u_2}{\partial x_1}\right)+\frac{\partial}{\partial\xi_2}\left(\frac{\partial u_3}{\partial x_1}\right)\frac{\partial}{\partial\xi_2}\left(\frac{\partial u_3}{\partial x_1}\right)\right.\\
&\quad+\frac{\partial}{\partial\xi_2}\left(\frac{\partial u_1}{\partial x_2}\right)\frac{\partial}{\partial\xi_2}\left(\frac{\partial u_1}{\partial x_2}\right)+\frac{\partial}{\partial\xi_2}\left(\frac{\partial u_2}{\partial x_2}\right)\frac{\partial}{\partial\xi_2}\left(\frac{\partial u_2}{\partial x_2}\right)+\frac{\partial}{\partial\xi_2}\left(\frac{\partial u_3}{\partial x_2}\right)\frac{\partial}{\partial\xi_2}\left(\frac{\partial u_3}{\partial x_2}\right)\\
&\quad\left.+\frac{\partial}{\partial\xi_2}\left(\frac{\partial u_1}{\partial x_3}\right)\frac{\partial}{\partial\xi_2}\left(\frac{\partial u_1}{\partial x_3}\right)+\frac{\partial}{\partial\xi_2}\left(\frac{\partial u_2}{\partial x_3}\right)\frac{\partial}{\partial\xi_2}\left(\frac{\partial u_2}{\partial x_3}\right)+\frac{\partial}{\partial\xi_2}\left(\frac{\partial u_3}{\partial x_3}\right)\frac{\partial}{\partial\xi_2}\left(\frac{\partial u_3}{\partial x_3}\right)\right]\\
&+C_{32}\left[\frac{\partial}{\partial\xi_3}\left(\frac{\partial u_1}{\partial x_1}\right)\frac{\partial}{\partial\xi_2}\left(\frac{\partial u_1}{\partial x_1}\right)+\frac{\partial}{\partial\xi_3}\left(\frac{\partial u_2}{\partial x_1}\right)\frac{\partial}{\partial\xi_2}\left(\frac{\partial u_2}{\partial x_1}\right)+\frac{\partial}{\partial\xi_3}\left(\frac{\partial u_3}{\partial x_1}\right)\frac{\partial}{\partial\xi_2}\left(\frac{\partial u_3}{\partial x_1}\right)\right.\\
&\quad+\frac{\partial}{\partial\xi_3}\left(\frac{\partial u_1}{\partial x_2}\right)\frac{\partial}{\partial\xi_2}\left(\frac{\partial u_1}{\partial x_2}\right)+\frac{\partial}{\partial\xi_3}\left(\frac{\partial u_2}{\partial x_2}\right)\frac{\partial}{\partial\xi_2}\left(\frac{\partial u_2}{\partial x_2}\right)+\frac{\partial}{\partial\xi_3}\left(\frac{\partial u_3}{\partial x_2}\right)\frac{\partial}{\partial\xi_2}\left(\frac{\partial u_3}{\partial x_2}\right)\\
&\quad\left.+\frac{\partial}{\partial\xi_3}\left(\frac{\partial u_1}{\partial x_3}\right)\frac{\partial}{\partial\xi_2}\left(\frac{\partial u_1}{\partial x_3}\right)+\frac{\partial}{\partial\xi_3}\left(\frac{\partial u_2}{\partial x_3}\right)\frac{\partial}{\partial\xi_2}\left(\frac{\partial u_2}{\partial x_3}\right)+\frac{\partial}{\partial\xi_3}\left(\frac{\partial u_3}{\partial x_3}\right)\frac{\partial}{\partial\xi_2}\left(\frac{\partial u_3}{\partial x_3}\right)\right]
\end{aligned}
\tag{C-2b}
$$

$$
\begin{aligned}
&+C_{13}\left[\frac{\partial}{\partial\xi_1}\left(\frac{\partial u_1}{\partial x_1}\right)\frac{\partial}{\partial\xi_3}\left(\frac{\partial u_1}{\partial x_1}\right)+\frac{\partial}{\partial\xi_1}\left(\frac{\partial u_2}{\partial x_1}\right)\frac{\partial}{\partial\xi_3}\left(\frac{\partial u_2}{\partial x_1}\right)+\frac{\partial}{\partial\xi_1}\left(\frac{\partial u_3}{\partial x_1}\right)\frac{\partial}{\partial\xi_3}\left(\frac{\partial u_3}{\partial x_1}\right)\right.\\
&\quad+\frac{\partial}{\partial\xi_1}\left(\frac{\partial u_1}{\partial x_2}\right)\frac{\partial}{\partial\xi_3}\left(\frac{\partial u_1}{\partial x_2}\right)+\frac{\partial}{\partial\xi_1}\left(\frac{\partial u_2}{\partial x_2}\right)\frac{\partial}{\partial\xi_3}\left(\frac{\partial u_2}{\partial x_2}\right)+\frac{\partial}{\partial\xi_1}\left(\frac{\partial u_3}{\partial x_2}\right)\frac{\partial}{\partial\xi_3}\left(\frac{\partial u_3}{\partial x_2}\right)\\
&\quad\left.+\frac{\partial}{\partial\xi_1}\left(\frac{\partial u_1}{\partial x_3}\right)\frac{\partial}{\partial\xi_3}\left(\frac{\partial u_1}{\partial x_3}\right)+\frac{\partial}{\partial\xi_1}\left(\frac{\partial u_2}{\partial x_3}\right)\frac{\partial}{\partial\xi_3}\left(\frac{\partial u_2}{\partial x_3}\right)+\frac{\partial}{\partial\xi_1}\left(\frac{\partial u_3}{\partial x_3}\right)\frac{\partial}{\partial\xi_3}\left(\frac{\partial u_3}{\partial x_3}\right)\right]\\
&+C_{23}\left[\frac{\partial}{\partial\xi_2}\left(\frac{\partial u_1}{\partial x_1}\right)\frac{\partial}{\partial\xi_3}\left(\frac{\partial u_1}{\partial x_1}\right)+\frac{\partial}{\partial\xi_2}\left(\frac{\partial u_2}{\partial x_1}\right)\frac{\partial}{\partial\xi_3}\left(\frac{\partial u_2}{\partial x_1}\right)+\frac{\partial}{\partial\xi_2}\left(\frac{\partial u_3}{\partial x_1}\right)\frac{\partial}{\partial\xi_3}\left(\frac{\partial u_3}{\partial x_1}\right)\right.\\
&\quad+\frac{\partial}{\partial\xi_2}\left(\frac{\partial u_1}{\partial x_2}\right)\frac{\partial}{\partial\xi_3}\left(\frac{\partial u_1}{\partial x_2}\right)+\frac{\partial}{\partial\xi_2}\left(\frac{\partial u_2}{\partial x_2}\right)\frac{\partial}{\partial\xi_3}\left(\frac{\partial u_2}{\partial x_2}\right)+\frac{\partial}{\partial\xi_2}\left(\frac{\partial u_3}{\partial x_2}\right)\frac{\partial}{\partial\xi_3}\left(\frac{\partial u_3}{\partial x_2}\right)\\
&\quad\left.+\frac{\partial}{\partial\xi_2}\left(\frac{\partial u_1}{\partial x_3}\right)\frac{\partial}{\partial\xi_3}\left(\frac{\partial u_1}{\partial x_3}\right)+\frac{\partial}{\partial\xi_2}\left(\frac{\partial u_2}{\partial x_3}\right)\frac{\partial}{\partial\xi_3}\left(\frac{\partial u_2}{\partial x_3}\right)+\frac{\partial}{\partial\xi_2}\left(\frac{\partial u_3}{\partial x_3}\right)\frac{\partial}{\partial\xi_3}\left(\frac{\partial u_3}{\partial x_3}\right)\right]\\
&+C_{33}\left[\frac{\partial}{\partial\xi_3}\left(\frac{\partial u_1}{\partial x_1}\right)\frac{\partial}{\partial\xi_3}\left(\frac{\partial u_1}{\partial x_1}\right)+\frac{\partial}{\partial\xi_3}\left(\frac{\partial u_2}{\partial x_1}\right)\frac{\partial}{\partial\xi_3}\left(\frac{\partial u_2}{\partial x_1}\right)+\frac{\partial}{\partial\xi_3}\left(\frac{\partial u_3}{\partial x_1}\right)\frac{\partial}{\partial\xi_3}\left(\frac{\partial u_3}{\partial x_1}\right)\right.\\
&\quad+\frac{\partial}{\partial\xi_3}\left(\frac{\partial u_1}{\partial x_2}\right)\frac{\partial}{\partial\xi_3}\left(\frac{\partial u_1}{\partial x_2}\right)+\frac{\partial}{\partial\xi_3}\left(\frac{\partial u_2}{\partial x_2}\right)\frac{\partial}{\partial\xi_3}\left(\frac{\partial u_2}{\partial x_2}\right)+\frac{\partial}{\partial\xi_3}\left(\frac{\partial u_3}{\partial x_2}\right)\frac{\partial}{\partial\xi_3}\left(\frac{\partial u_3}{\partial x_2}\right)\\
&\quad\left.\left.+\frac{\partial}{\partial\xi_3}\left(\frac{\partial u_1}{\partial x_3}\right)\frac{\partial}{\partial\xi_3}\left(\frac{\partial u_1}{\partial x_3}\right)+\frac{\partial}{\partial\xi_3}\left(\frac{\partial u_2}{\partial x_3}\right)\frac{\partial}{\partial\xi_3}\left(\frac{\partial u_2}{\partial x_3}\right)+\frac{\partial}{\partial\xi_3}\left(\frac{\partial u_3}{\partial x_3}\right)\frac{\partial}{\partial\xi_3}\left(\frac{\partial u_3}{\partial x_3}\right)\right]\right\} \qquad \text{(C-2b)}\\
&=\frac{1}{J}\Big[C_{11}\left(A_{11}\right)+C_{22}\left(A_{22}\right)+C_{33}\left(A_{33}\right)\\
&+\left(C_{12}+C_{21}\right)\left(A_{12}\right)+\left(C_{13}+C_{31}\right)\left(A_{13}\right)+\left(C_{23}+C_{32}\right)\left(A_{23}\right)\Big]
\end{aligned}
$$

where

$$
\begin{aligned}
A_{11}=&\left[\frac{\partial}{\partial\xi_1}\left(\frac{\partial u_1}{\partial x_1}\right)\frac{\partial}{\partial\xi_1}\left(\frac{\partial u_1}{\partial x_1}\right)+\frac{\partial}{\partial\xi_1}\left(\frac{\partial u_2}{\partial x_1}\right)\frac{\partial}{\partial\xi_1}\left(\frac{\partial u_2}{\partial x_1}\right)+\frac{\partial}{\partial\xi_1}\left(\frac{\partial u_3}{\partial x_1}\right)\frac{\partial}{\partial\xi_1}\left(\frac{\partial u_3}{\partial x_1}\right)\right.\\
&+\frac{\partial}{\partial\xi_1}\left(\frac{\partial u_1}{\partial x_2}\right)\frac{\partial}{\partial\xi_1}\left(\frac{\partial u_1}{\partial x_2}\right)+\frac{\partial}{\partial\xi_1}\left(\frac{\partial u_2}{\partial x_2}\right)\frac{\partial}{\partial\xi_1}\left(\frac{\partial u_2}{\partial x_2}\right)+\frac{\partial}{\partial\xi_1}\left(\frac{\partial u_3}{\partial x_2}\right)\frac{\partial}{\partial\xi_1}\left(\frac{\partial u_3}{\partial x_2}\right) \qquad \text{(C-3a)}\\
&\left.+\frac{\partial}{\partial\xi_1}\left(\frac{\partial u_1}{\partial x_3}\right)\frac{\partial}{\partial\xi_1}\left(\frac{\partial u_1}{\partial x_3}\right)+\frac{\partial}{\partial\xi_1}\left(\frac{\partial u_2}{\partial x_3}\right)\frac{\partial}{\partial\xi_1}\left(\frac{\partial u_2}{\partial x_3}\right)+\frac{\partial}{\partial\xi_1}\left(\frac{\partial u_3}{\partial x_3}\right)\frac{\partial}{\partial\xi_1}\left(\frac{\partial u_3}{\partial x_3}\right)\right]
\end{aligned}
$$

$$A_{22}=\left[\frac{\partial}{\partial\xi_2}\left(\frac{\partial u_1}{\partial x_1}\right)\frac{\partial}{\partial\xi_2}\left(\frac{\partial u_1}{\partial x_1}\right)+\frac{\partial}{\partial\xi_2}\left(\frac{\partial u_2}{\partial x_1}\right)\frac{\partial}{\partial\xi_2}\left(\frac{\partial u_2}{\partial x_1}\right)+\frac{\partial}{\partial\xi_2}\left(\frac{\partial u_3}{\partial x_1}\right)\frac{\partial}{\partial\xi_2}\left(\frac{\partial u_3}{\partial x_1}\right)\right.$$
$$+\frac{\partial}{\partial\xi_2}\left(\frac{\partial u_1}{\partial x_2}\right)\frac{\partial}{\partial\xi_2}\left(\frac{\partial u_1}{\partial x_2}\right)+\frac{\partial}{\partial\xi_2}\left(\frac{\partial u_2}{\partial x_2}\right)\frac{\partial}{\partial\xi_2}\left(\frac{\partial u_2}{\partial x_2}\right)+\frac{\partial}{\partial\xi_2}\left(\frac{\partial u_3}{\partial x_2}\right)\frac{\partial}{\partial\xi_2}\left(\frac{\partial u_3}{\partial x_2}\right) \qquad \text{(C-3b)}$$
$$\left.+\frac{\partial}{\partial\xi_2}\left(\frac{\partial u_1}{\partial x_3}\right)\frac{\partial}{\partial\xi_2}\left(\frac{\partial u_1}{\partial x_3}\right)+\frac{\partial}{\partial\xi_2}\left(\frac{\partial u_2}{\partial x_3}\right)\frac{\partial}{\partial\xi_2}\left(\frac{\partial u_2}{\partial x_3}\right)+\frac{\partial}{\partial\xi_2}\left(\frac{\partial u_3}{\partial x_3}\right)\frac{\partial}{\partial\xi_2}\left(\frac{\partial u_3}{\partial x_3}\right)\right]$$

$$A_{33}=\left[\frac{\partial}{\partial\xi_3}\left(\frac{\partial u_1}{\partial x_1}\right)\frac{\partial}{\partial\xi_3}\left(\frac{\partial u_1}{\partial x_1}\right)+\frac{\partial}{\partial\xi_3}\left(\frac{\partial u_2}{\partial x_1}\right)\frac{\partial}{\partial\xi_3}\left(\frac{\partial u_2}{\partial x_1}\right)+\frac{\partial}{\partial\xi_3}\left(\frac{\partial u_3}{\partial x_1}\right)\frac{\partial}{\partial\xi_3}\left(\frac{\partial u_3}{\partial x_1}\right)\right.$$
$$+\frac{\partial}{\partial\xi_3}\left(\frac{\partial u_1}{\partial x_2}\right)\frac{\partial}{\partial\xi_3}\left(\frac{\partial u_1}{\partial x_2}\right)+\frac{\partial}{\partial\xi_3}\left(\frac{\partial u_2}{\partial x_2}\right)\frac{\partial}{\partial\xi_3}\left(\frac{\partial u_2}{\partial x_2}\right)+\frac{\partial}{\partial\xi_3}\left(\frac{\partial u_3}{\partial x_2}\right)\frac{\partial}{\partial\xi_3}\left(\frac{\partial u_3}{\partial x_2}\right) \qquad \text{(C-3c)}$$
$$\left.+\frac{\partial}{\partial\xi_3}\left(\frac{\partial u_1}{\partial x_3}\right)\frac{\partial}{\partial\xi_3}\left(\frac{\partial u_1}{\partial x_3}\right)+\frac{\partial}{\partial\xi_3}\left(\frac{\partial u_2}{\partial x_3}\right)\frac{\partial}{\partial\xi_3}\left(\frac{\partial u_2}{\partial x_3}\right)+\frac{\partial}{\partial\xi_3}\left(\frac{\partial u_3}{\partial x_3}\right)\frac{\partial}{\partial\xi_3}\left(\frac{\partial u_3}{\partial x_3}\right)\right]$$

$$A_{12}=\left[\frac{\partial}{\partial\xi_1}\left(\frac{\partial u_1}{\partial x_1}\right)\frac{\partial}{\partial\xi_2}\left(\frac{\partial u_1}{\partial x_1}\right)+\frac{\partial}{\partial\xi_1}\left(\frac{\partial u_2}{\partial x_1}\right)\frac{\partial}{\partial\xi_2}\left(\frac{\partial u_2}{\partial x_1}\right)+\frac{\partial}{\partial\xi_1}\left(\frac{\partial u_3}{\partial x_1}\right)\frac{\partial}{\partial\xi_2}\left(\frac{\partial u_3}{\partial x_1}\right)\right.$$
$$+\frac{\partial}{\partial\xi_1}\left(\frac{\partial u_1}{\partial x_2}\right)\frac{\partial}{\partial\xi_2}\left(\frac{\partial u_1}{\partial x_2}\right)+\frac{\partial}{\partial\xi_1}\left(\frac{\partial u_2}{\partial x_2}\right)\frac{\partial}{\partial\xi_2}\left(\frac{\partial u_2}{\partial x_2}\right)+\frac{\partial}{\partial\xi_1}\left(\frac{\partial u_3}{\partial x_2}\right)\frac{\partial}{\partial\xi_2}\left(\frac{\partial u_3}{\partial x_2}\right) \qquad \text{(C-3d)}$$
$$\left.+\frac{\partial}{\partial\xi_1}\left(\frac{\partial u_1}{\partial x_3}\right)\frac{\partial}{\partial\xi_2}\left(\frac{\partial u_1}{\partial x_3}\right)+\frac{\partial}{\partial\xi_1}\left(\frac{\partial u_2}{\partial x_3}\right)\frac{\partial}{\partial\xi_2}\left(\frac{\partial u_2}{\partial x_3}\right)+\frac{\partial}{\partial\xi_1}\left(\frac{\partial u_3}{\partial x_3}\right)\frac{\partial}{\partial\xi_2}\left(\frac{\partial u_3}{\partial x_3}\right)\right]$$

$$A_{13}=\left[\frac{\partial}{\partial\xi_1}\left(\frac{\partial u_1}{\partial x_1}\right)\frac{\partial}{\partial\xi_3}\left(\frac{\partial u_1}{\partial x_1}\right)+\frac{\partial}{\partial\xi_1}\left(\frac{\partial u_2}{\partial x_1}\right)\frac{\partial}{\partial\xi_3}\left(\frac{\partial u_2}{\partial x_1}\right)+\frac{\partial}{\partial\xi_1}\left(\frac{\partial u_3}{\partial x_1}\right)\frac{\partial}{\partial\xi_3}\left(\frac{\partial u_3}{\partial x_1}\right)\right.$$
$$+\frac{\partial}{\partial\xi_1}\left(\frac{\partial u_1}{\partial x_2}\right)\frac{\partial}{\partial\xi_3}\left(\frac{\partial u_1}{\partial x_2}\right)+\frac{\partial}{\partial\xi_1}\left(\frac{\partial u_2}{\partial x_2}\right)\frac{\partial}{\partial\xi_3}\left(\frac{\partial u_2}{\partial x_2}\right)+\frac{\partial}{\partial\xi_1}\left(\frac{\partial u_3}{\partial x_2}\right)\frac{\partial}{\partial\xi_3}\left(\frac{\partial u_3}{\partial x_2}\right) \qquad \text{(C-3e)}$$
$$\left.+\frac{\partial}{\partial\xi_1}\left(\frac{\partial u_1}{\partial x_3}\right)\frac{\partial}{\partial\xi_3}\left(\frac{\partial u_1}{\partial x_3}\right)+\frac{\partial}{\partial\xi_1}\left(\frac{\partial u_2}{\partial x_3}\right)\frac{\partial}{\partial\xi_3}\left(\frac{\partial u_2}{\partial x_3}\right)+\frac{\partial}{\partial\xi_1}\left(\frac{\partial u_3}{\partial x_3}\right)\frac{\partial}{\partial\xi_3}\left(\frac{\partial u_3}{\partial x_3}\right)\right]$$

$$A_{23}=\left[\frac{\partial}{\partial\xi_2}\left(\frac{\partial u_1}{\partial x_1}\right)\frac{\partial}{\partial\xi_3}\left(\frac{\partial u_1}{\partial x_1}\right)+\frac{\partial}{\partial\xi_2}\left(\frac{\partial u_2}{\partial x_1}\right)\frac{\partial}{\partial\xi_3}\left(\frac{\partial u_2}{\partial x_1}\right)+\frac{\partial}{\partial\xi_2}\left(\frac{\partial u_3}{\partial x_1}\right)\frac{\partial}{\partial\xi_3}\left(\frac{\partial u_3}{\partial x_1}\right)\right.$$
$$+\frac{\partial}{\partial\xi_2}\left(\frac{\partial u_1}{\partial x_2}\right)\frac{\partial}{\partial\xi_3}\left(\frac{\partial u_1}{\partial x_2}\right)+\frac{\partial}{\partial\xi_2}\left(\frac{\partial u_2}{\partial x_2}\right)\frac{\partial}{\partial\xi_3}\left(\frac{\partial u_2}{\partial x_2}\right)+\frac{\partial}{\partial\xi_2}\left(\frac{\partial u_3}{\partial x_2}\right)\frac{\partial}{\partial\xi_3}\left(\frac{\partial u_3}{\partial x_2}\right) \qquad \text{(C-3f)}$$
$$\left.+\frac{\partial}{\partial\xi_2}\left(\frac{\partial u_1}{\partial x_3}\right)\frac{\partial}{\partial\xi_3}\left(\frac{\partial u_1}{\partial x_3}\right)+\frac{\partial}{\partial\xi_2}\left(\frac{\partial u_2}{\partial x_3}\right)\frac{\partial}{\partial\xi_3}\left(\frac{\partial u_2}{\partial x_3}\right)+\frac{\partial}{\partial\xi_2}\left(\frac{\partial u_3}{\partial x_3}\right)\frac{\partial}{\partial\xi_3}\left(\frac{\partial u_3}{\partial x_3}\right)\right]$$

Integrate (C-3a) – (C-3f) over the control volume and apply to (B-9), A_{ij}'s become

$$\iiint A_{11}d\xi d\eta d\zeta$$
$$=\left[\left(\frac{\partial u_1}{\partial x_1}\right)_e-\left(\frac{\partial u_1}{\partial x_1}\right)_w\right]^2+\left[\left(\frac{\partial u_2}{\partial x_1}\right)_e-\left(\frac{\partial u_2}{\partial x_1}\right)_w\right]^2+\left[\left(\frac{\partial u_3}{\partial x_1}\right)_e-\left(\frac{\partial u_3}{\partial x_1}\right)_w\right]^2$$
$$+\left[\left(\frac{\partial u_1}{\partial x_2}\right)_e-\left(\frac{\partial u_1}{\partial x_2}\right)_w\right]^2+\left[\left(\frac{\partial u_2}{\partial x_2}\right)_e-\left(\frac{\partial u_2}{\partial x_2}\right)_w\right]^2+\left[\left(\frac{\partial u_3}{\partial x_2}\right)_e-\left(\frac{\partial u_3}{\partial x_2}\right)_w\right]^2 \qquad \text{(C-4a)}$$
$$+\left[\left(\frac{\partial u_1}{\partial x_3}\right)_e-\left(\frac{\partial u_1}{\partial x_3}\right)_w\right]^2+\left[\left(\frac{\partial u_2}{\partial x_3}\right)_e-\left(\frac{\partial u_2}{\partial x_3}\right)_w\right]^2+\left[\left(\frac{\partial u_3}{\partial x_3}\right)_e-\left(\frac{\partial u_3}{\partial x_3}\right)_w\right]^2$$

$$\iiint A_{22}d\xi d\eta d\zeta$$
$$=\left[\left(\frac{\partial u_1}{\partial x_1}\right)_n-\left(\frac{\partial u_1}{\partial x_1}\right)_s\right]^2+\left[\left(\frac{\partial u_2}{\partial x_1}\right)_n-\left(\frac{\partial u_2}{\partial x_1}\right)_s\right]^2+\left[\left(\frac{\partial u_3}{\partial x_1}\right)_n-\left(\frac{\partial u_3}{\partial x_1}\right)_s\right]^2$$
$$+\left[\left(\frac{\partial u_1}{\partial x_2}\right)_n-\left(\frac{\partial u_1}{\partial x_2}\right)_s\right]^2+\left[\left(\frac{\partial u_2}{\partial x_2}\right)_n-\left(\frac{\partial u_2}{\partial x_2}\right)_s\right]^2+\left[\left(\frac{\partial u_3}{\partial x_2}\right)_n-\left(\frac{\partial u_3}{\partial x_2}\right)_s\right]^2 \qquad \text{(C-4b)}$$
$$+\left[\left(\frac{\partial u_1}{\partial x_3}\right)_n-\left(\frac{\partial u_1}{\partial x_3}\right)_s\right]^2+\left[\left(\frac{\partial u_2}{\partial x_3}\right)_n-\left(\frac{\partial u_2}{\partial x_3}\right)_s\right]^2+\left[\left(\frac{\partial u_3}{\partial x_3}\right)_n-\left(\frac{\partial u_3}{\partial x_3}\right)_s\right]^2$$

$$\iiint A_{33}\,d\xi d\eta d\zeta$$

$$\begin{aligned}
&= \left[\left(\frac{\partial u_1}{\partial x_1}\right)_t - \left(\frac{\partial u_1}{\partial x_1}\right)_b\right]^2 + \left[\left(\frac{\partial u_2}{\partial x_1}\right)_t - \left(\frac{\partial u_2}{\partial x_1}\right)_b\right]^2 + \left[\left(\frac{\partial u_3}{\partial x_1}\right)_t - \left(\frac{\partial u_3}{\partial x_1}\right)_b\right]^2 \\
&+ \left[\left(\frac{\partial u_1}{\partial x_2}\right)_t - \left(\frac{\partial u_1}{\partial x_2}\right)_b\right]^2 + \left[\left(\frac{\partial u_2}{\partial x_2}\right)_t - \left(\frac{\partial u_2}{\partial x_2}\right)_b\right]^2 + \left[\left(\frac{\partial u_3}{\partial x_2}\right)_t - \left(\frac{\partial u_3}{\partial x_2}\right)_b\right]^2 \\
&+ \left[\left(\frac{\partial u_1}{\partial x_3}\right)_t - \left(\frac{\partial u_1}{\partial x_3}\right)_b\right]^2 + \left[\left(\frac{\partial u_2}{\partial x_3}\right)_t - \left(\frac{\partial u_2}{\partial x_3}\right)_b\right]^2 + \left[\left(\frac{\partial u_3}{\partial x_3}\right)_t - \left(\frac{\partial u_3}{\partial x_3}\right)_b\right]^2
\end{aligned} \tag{C-4c}$$

$$\iiint A_{12}\,d\xi d\eta d\zeta$$

$$\begin{aligned}
&= \left[\left(\frac{\partial u_1}{\partial x_1}\right)_e - \left(\frac{\partial u_1}{\partial x_1}\right)_w\right]\left[\left(\frac{\partial u_1}{\partial x_1}\right)_n - \left(\frac{\partial u_1}{\partial x_1}\right)_s\right] + \left[\left(\frac{\partial u_2}{\partial x_1}\right)_e - \left(\frac{\partial u_2}{\partial x_1}\right)_w\right]\left[\left(\frac{\partial u_2}{\partial x_1}\right)_n - \left(\frac{\partial u_2}{\partial x_1}\right)_s\right] \\
&+ \left[\left(\frac{\partial u_3}{\partial x_1}\right)_e - \left(\frac{\partial u_3}{\partial x_1}\right)_w\right]\left[\left(\frac{\partial u_3}{\partial x_1}\right)_n - \left(\frac{\partial u_3}{\partial x_1}\right)_s\right] \\
&+ \left[\left(\frac{\partial u_1}{\partial x_2}\right)_e - \left(\frac{\partial u_1}{\partial x_2}\right)_w\right]\left[\left(\frac{\partial u_1}{\partial x_2}\right)_n - \left(\frac{\partial u_1}{\partial x_2}\right)_s\right] + \left[\left(\frac{\partial u_2}{\partial x_2}\right)_e - \left(\frac{\partial u_2}{\partial x_2}\right)_w\right]\left[\left(\frac{\partial u_2}{\partial x_2}\right)_n - \left(\frac{\partial u_2}{\partial x_2}\right)_s\right] \\
&+ \left[\left(\frac{\partial u_3}{\partial x_2}\right)_e - \left(\frac{\partial u_3}{\partial x_2}\right)_w\right]\left[\left(\frac{\partial u_3}{\partial x_2}\right)_n - \left(\frac{\partial u_3}{\partial x_2}\right)_s\right] \\
&+ \left[\left(\frac{\partial u_1}{\partial x_3}\right)_e - \left(\frac{\partial u_1}{\partial x_3}\right)_w\right]\left[\left(\frac{\partial u_1}{\partial x_3}\right)_n - \left(\frac{\partial u_1}{\partial x_3}\right)_s\right] + \left[\left(\frac{\partial u_2}{\partial x_3}\right)_e - \left(\frac{\partial u_2}{\partial x_3}\right)_w\right]\left[\left(\frac{\partial u_2}{\partial x_3}\right)_n - \left(\frac{\partial u_2}{\partial x_3}\right)_s\right] \\
&+ \left[\left(\frac{\partial u_3}{\partial x_3}\right)_e - \left(\frac{\partial u_3}{\partial x_3}\right)_w\right]\left[\left(\frac{\partial u_3}{\partial x_3}\right)_n - \left(\frac{\partial u_3}{\partial x_3}\right)_s\right]
\end{aligned} \tag{C-4d}$$

$$
\begin{aligned}
&\iiint A_{13}\,d\xi\,d\eta\,d\zeta \\
&= \left[\left(\frac{\partial u_1}{\partial x_1}\right)_e - \left(\frac{\partial u_1}{\partial x_1}\right)_w\right]\left[\left(\frac{\partial u_1}{\partial x_1}\right)_t - \left(\frac{\partial u_1}{\partial x_1}\right)_b\right] + \left[\left(\frac{\partial u_2}{\partial x_1}\right)_e - \left(\frac{\partial u_2}{\partial x_1}\right)_w\right]\left[\left(\frac{\partial u_2}{\partial x_1}\right)_t - \left(\frac{\partial u_2}{\partial x_1}\right)_b\right] \\
&+ \left[\left(\frac{\partial u_3}{\partial x_1}\right)_e - \left(\frac{\partial u_3}{\partial x_1}\right)_w\right]\left[\left(\frac{\partial u_3}{\partial x_1}\right)_t - \left(\frac{\partial u_3}{\partial x_1}\right)_b\right] \\
&+ \left[\left(\frac{\partial u_1}{\partial x_2}\right)_e - \left(\frac{\partial u_1}{\partial x_2}\right)_w\right]\left[\left(\frac{\partial u_1}{\partial x_2}\right)_t - \left(\frac{\partial u_1}{\partial x_2}\right)_b\right] + \left[\left(\frac{\partial u_2}{\partial x_2}\right)_e - \left(\frac{\partial u_2}{\partial x_2}\right)_w\right]\left[\left(\frac{\partial u_2}{\partial x_2}\right)_t - \left(\frac{\partial u_2}{\partial x_2}\right)_b\right] \\
&+ \left[\left(\frac{\partial u_3}{\partial x_2}\right)_e - \left(\frac{\partial u_3}{\partial x_2}\right)_w\right]\left[\left(\frac{\partial u_3}{\partial x_2}\right)_t - \left(\frac{\partial u_3}{\partial x_2}\right)_b\right] \\
&+ \left[\left(\frac{\partial u_1}{\partial x_3}\right)_e - \left(\frac{\partial u_1}{\partial x_3}\right)_w\right]\left[\left(\frac{\partial u_1}{\partial x_3}\right)_t - \left(\frac{\partial u_1}{\partial x_3}\right)_b\right] + \left[\left(\frac{\partial u_2}{\partial x_3}\right)_e - \left(\frac{\partial u_2}{\partial x_3}\right)_w\right]\left[\left(\frac{\partial u_2}{\partial x_3}\right)_t - \left(\frac{\partial u_2}{\partial x_3}\right)_b\right] \\
&+ \left[\left(\frac{\partial u_3}{\partial x_3}\right)_e - \left(\frac{\partial u_3}{\partial x_3}\right)_w\right]\left[\left(\frac{\partial u_3}{\partial x_3}\right)_t - \left(\frac{\partial u_3}{\partial x_3}\right)_b\right]
\end{aligned}
\tag{C-4e}
$$

$$
\begin{aligned}
&\iiint A_{23}\,d\xi\,d\eta\,d\zeta \\
&= \left[\left(\frac{\partial u_1}{\partial x_1}\right)_n - \left(\frac{\partial u_1}{\partial x_1}\right)_s\right]\left[\left(\frac{\partial u_1}{\partial x_1}\right)_t - \left(\frac{\partial u_1}{\partial x_1}\right)_b\right] + \left[\left(\frac{\partial u_2}{\partial x_1}\right)_n - \left(\frac{\partial u_2}{\partial x_1}\right)_s\right]\left[\left(\frac{\partial u_2}{\partial x_1}\right)_t - \left(\frac{\partial u_2}{\partial x_1}\right)_b\right] \\
&+ \left[\left(\frac{\partial u_3}{\partial x_1}\right)_n - \left(\frac{\partial u_3}{\partial x_1}\right)_s\right]\left[\left(\frac{\partial u_3}{\partial x_1}\right)_t - \left(\frac{\partial u_3}{\partial x_1}\right)_b\right] \\
&+ \left[\left(\frac{\partial u_1}{\partial x_2}\right)_n - \left(\frac{\partial u_1}{\partial x_2}\right)_s\right]\left[\left(\frac{\partial u_1}{\partial x_2}\right)_t - \left(\frac{\partial u_1}{\partial x_2}\right)_b\right] + \left[\left(\frac{\partial u_2}{\partial x_2}\right)_n - \left(\frac{\partial u_2}{\partial x_2}\right)_s\right]\left[\left(\frac{\partial u_2}{\partial x_2}\right)_t - \left(\frac{\partial u_2}{\partial x_2}\right)_b\right] \\
&+ \left[\left(\frac{\partial u_3}{\partial x_2}\right)_n - \left(\frac{\partial u_3}{\partial x_2}\right)_s\right]\left[\left(\frac{\partial u_3}{\partial x_2}\right)_t - \left(\frac{\partial u_3}{\partial x_2}\right)_b\right] \\
&+ \left[\left(\frac{\partial u_1}{\partial x_3}\right)_n - \left(\frac{\partial u_1}{\partial x_3}\right)_s\right]\left[\left(\frac{\partial u_1}{\partial x_3}\right)_t - \left(\frac{\partial u_1}{\partial x_3}\right)_b\right] + \left[\left(\frac{\partial u_2}{\partial x_3}\right)_n - \left(\frac{\partial u_2}{\partial x_3}\right)_s\right]\left[\left(\frac{\partial u_2}{\partial x_3}\right)_t - \left(\frac{\partial u_2}{\partial x_3}\right)_b\right] \\
&+ \left[\left(\frac{\partial u_3}{\partial x_3}\right)_n - \left(\frac{\partial u_3}{\partial x_3}\right)_s\right]\left[\left(\frac{\partial u_3}{\partial x_3}\right)_t - \left(\frac{\partial u_3}{\partial x_3}\right)_b\right]
\end{aligned}
\tag{C-4f}
$$

(C-1c) and (C-2b) are the generalized forms for the additional source terms in the low-Reynolds number k-ε turbulent model.

References

Amos, B., Kodama, H., Fernandez-Pello, A.C., "An Analysis of the Ignition by Vapor Radiation Absorption of a Vaporizing Fuel at Zero Gravity", *Combust. Sci. Tech*. (62) (1988) 331-343.

Arthur, J.A., "Reactions between Carbon and Oxygen", *Trans. Faraday Soc*., (47) (1951) 164-178.

ASME The Engineering Index (1922) 283.

Atreya, A., "Pyrolysis, Ignition and Flame Spread on Horizontal Surfaces of Wood", *Ph.D. thesis, Harvard University, Cambridge, MA* (1983).

Atreya, A., Baum, H.R., "A Model of Opposed-Flow Flame Spread Over Charring Materials", *Proceeding of the Combustion Institute* (29) (2003) 227-236.

Baker, E., Mudge, L., "Mechanisms of Catalytic Biomass Gasification", *Journal of Analytical and Applied Pyrolysis* (6) (1984) 285-297.

Baum, H., Atreya, A., "A Model of Transport of Fuel Gases in a Charring Solid and Its Application to Opposed-Flow Flame Spread", *Proceeding of the Combustion Institute* (31) (2007) 2633-2641.

Beenackers, A.A.C.M., ""Biomass Gasification in Moving Beds, A Review of European Technologies", *Renerable Energy* (16) (1999) 1180-1186.

Bellais, M., Davidsson, K.O., Liliedahl, T., Sjostrom, K., Petersson, J.B.C., "Pyrolysis of Large Wood Particles: A Study of Shrinkage Importance in Simulations", *Fuel*, (82) (12) (2003)1541-1548.

Bilodeau, J.F., Therien, N., Proulx, P., Czernik, S., Chornet, E., "A Mathematical-Model of Fluidized-Bed Biomass Gasification", *Canadian Journal of Chemical Engineering* (71) (1993) 549-557.

Biomass as Feedstock for a Bioenergy and Bioproducts Industry: The Technical Feasibility of Billion-Ton Annual Supply, *U.S. Department of AgriculturalsForestry Service Technical Report* (2005).

Breakman-Danheux, C., D'haeyere, A., Fontana, A., Laurent, P., "Upgrading of Waste Derived Solid Fuel by Steam Gasification", *Fuel* (77) (1-2) (1998) 55-59.

Broido, A., "Kinetics of Solid-Phase Cellulose Pyrolysis. In: Shafizadeh, F., Sarkanen, K. and Tillman, D., editors, Thermal Uses and Properties of Carbohydrates and Lignins", *Academic Press* (1976) 19-35.

Bryden, K.M., Ragland, K.W., Rutland, C.J., "Modeling Thermally Thick Pyrolysis of Wood", *Biomass & Bioenergy* (22) (2002) 41-53.

Davis, Transportation Energy Data Book 18, Technical Report ORNL-6941, *Oak Ridge National Laboratory, Oak Ridge, TN* (1998).

Demirbas, A. "Pyrolysis of Ground Beech Wood in Irregular Heating Rate Conditions", *J. Anal. Appl. Pyrolysis* (73) (2005) 39-43.

Di Blasi, C., Branca, C., Santoro, A., Hernandez, E.G., "Pyrolytic Behavior and Products of Some Wood Varieties", *Combustion and Flame* (124) (2001) 165-177.

Dobner S., "Modeling of Entrained Bed Gasification: The Issues", *Electric Power Research Institute Memo, Palo Alto, California* (1976).

Donath, E.E., Glenn, R. A., "Computer Study of Stage Two Reactions in BCR Two-Stage Super-Pressure Coal Gasification Process", *American Chemical Society - Division of Fuel Chemistry Preprints* (11) (1967) 333-347.

Dutta, S., Wen, C.Y., "Reactivity of Coal and Char. 1. In Carbon Dioxide Atmosphere", *Ind. Eng. Chem., Process Design and Development* (16) (1) (1977) 20-30.

Galgano, A., Di Blasi, C., "Modeling the Propagation of Drying and Decomposition Front in Wood", *Combustion and Flame* (139) (2004) 16-27.

Glushko, G.S., "Turbulent Boundary Layer on a Flat Plate in an Incompressible Fluid", *Izv. Acad. Nauk SSSR Mekh* (4) (1965) 13.

Goring, G.E., Curran, G.P., Tarbox, R.P., Gorin, E., "Kinetics of Carbon Gasification by Steam - Effect of High Temperature Pretreatment on Reactivity of Low Temperature Char to Steam and Carbon Dioxide", *Industrial and Engineering Chemistry* (44) (1952) 1051-1057.

Groveneveld, M.J., Van Swaaij, W.P.M., "Gasification of Solid Waste - Potential and Application of Co-current Moving Bed Gasifiers", *Applied Energy* (5) (3) (1979) 165-178.

GrØnli, M.G., Várhegyi, G., Di Blasi, C., "Thermogravimetric Analysis and Devolatilization Kinetics of Wood", *Ind. Eng. Chem. Res*. (41) (2002) 4201-4208.

Gupta A.K., Cinchonski, W., "Ultrahigh Temperature Steam Gasification of Biomass and Solid Waste", *Environmental Engineering Science* (24) (8) (2007) 1179-1189.

Hamel, S., Krumm, W., “Mathematical Modeling and Simulation of Bubbling Fluidized Bed Gasifier”, *Poweder Technol* (120) (1-2) (2001) 105-112.

Han, J., Kim, H., “The Reductiaon and Control Technology of Tar During Biomass Gasification/Pyrolysis: An Overview”, Renewable and Sustainable Energy Reviews (12) (2008) 397-416.

Hayase, T., Humphrey, J.A.C., Greif, R., “A Consistently Formulated QUICK Scheme for Fast and Stable Convergence Using Finite-Volume Iterative Calculation Procedures”, *J. Comput. Phy.* (98) (1992) 108-118.

Hobbs, M.L., Radulovic, P.T., Smoot D., “Modeling Fixed-Bed Coal Gasifier”, *AIChE Journal* (38) (5) (1992) 681 – 702.

Hsu, C.T., Cheng, P., “Thermal Dispersion in a Porous Medium”, *Int. J. Heat Mass Transfer* (33) (8) (1990) 1587-1597.

Im, H.G., Kim, T.Y., “Computational Modeling of Combustion and Heat Transfer in Partial Oxidation of the Waste Gasification Process”, *Proceedings of the International Symposium on Green Technology for Resources and Minerals Recycling*, *South Korea* (2004) 24-27.

Jennen, T., Hiller, R., Kneke, D., Weinspach, P.M., “Modeling of Gasification of Wood in a Circulating Fluidized Bed”, *Chem. Eng. Technol*. (22) (10) (1999) 822-826.

Jones, W.P., Launder, B.E., “The Prediction of Laminarization with a 2-Equation Model of Turbulence”, *Int. J. Heat & Mass Transfer* (15) (2) (1972) 301-314.

Jones, W.P. and Launder, B.E., "The calculation of of Low-Reynolds-Number Phenomena with a 2-Equation Model of Turbulence", *Int. J. Heat & Mass Transfer* (16) (6) (1973) 1119-1130.

Koufopanos, C. A., Papayannakos, N., Maschio, G., Lucchesi, A., "Modeling of the Pyrolysis of Biomass Particles. Studies on Kinetics, Thermal and Heat Transfer Effects", *Canadian Journal of Chemical Engineering* (69) (4) (1991) 907-915.

Kutzbach, K. "Die Vergasung der Brennstoffe in Generatoren, Insbesondere fur Kraftgasbetriebe (The Gasification of Fuels in Producers, Especially for the Production of Power Gas)." *Zeitschrift des Vereines Deutscher Ingenieure* (49) (1905) 233-241.

Kwak, T., Maken, S., Lee, S., Park, J., Min, B., Yoo, Y.D., "Environmental Aspects of Gasification of Korean Municipal Solid Waste in a Pilot Plant", *Fuel* (85) (14-15) (2006) 2012-2017.

Law, C.K., Combustion Physics, *Cambridge University Press* (2006).

Lewis, W.K., Gilliland, E.R., McBride, G.T., "Gasification of Carbon by Carbon Dioxide in Fluidized Powder Bed" *Industrial and Engineering Chemistry* (41) (1949) 1213-1226.

Lee, S.H., Son, Y.I., Ko, C.B. Choi, K.B., Kim, J.H., "The Study of Energy Conversion in a 2Ton/Day Waste-Wood Fixed Bed Gasifier", *J. Korean Ind. Eng. Chem.*(20) (4) (2009) 391-395.

Li, X.T., Grace, J.R., Lim, C.J., Watkinson, A.P., Chen, H.P., Kim, J.R., "Biomass Gasification in a Circulating Fluidized Bed", *Biomass and Bioenergy* (26) (2004) 171-193.

Liao, Y.F, Wang, S.R., Ma, X.Q, "Study of Reaction Mechanisms in Cellulose Pyrolysis", Prepr. Pap.-Am. Chem. Soc., Div. Fuel Chem. (49) (1) (2004) 407-411.

Liu, X.J., Zhang, W.R., Park, T.J., "Modelling Coal Gasification in an Entrained Flow Gasifier", *Combustion Theory and Modeling* (5) (4) (2001) 595-608.

Mohan D., Pittman Jr, C.U., Steele, P.H., "Pyrolysis of Wood/Biomass for Bio-oil", *Energy & Fuels* (20) (2006) 848-889.

Moore, J.A., "Pyrolysis.", *McGraw-Hill Encyclopedia of Science and Technology* 9th ed. (2002).

Na, J.I., Park, J.S., Kim, Y.K., Lee, J.G., Kim, J.H., "Characteristics of Oxygen-Blown Gasification for Combustible Waste in a Fixed-Bed Gasifier", *Applied Energy* (75) (3-4) (2003) 275-285.

Nield, D.A., Bejan, A., Convection in Porous Media, 2nd ed., *Springer* (1998).

Nimz, H. H., " Chemistry of Potential Chromophoric Groups in Beech Lignin", *Tappi J.* (56) (1973) 124.

Ould-Amer, Y., Chikh, S., Bouhadef, K., Lauriat, G., "Forced Convection Cooling Enhancement by Use of Porous Materials", Int. *J. Heat and Fluid Flow* (19) (1998) 251-258.

Pan, W.P., Richards, G.N., "Volatile Products of Oxidative Pyrolysis of Wood: Influence of Metal Ions", *J. of Analytical and Applied Pyrolysis* (17) (1990) 261-273.

Park, W.C., Atreya, A., Baum, H.R., "Determination of Pyrolysis Temperature for Charring Materials", *Proceeding of the Combustion Institute* (32) (2009) 2471-2479.

Patankar, S.V., Numerical Heat Transfer and Fluid Flow, *Hemisphere /McGraw-Hill, Washington, DC* (1980).

Raman, P., Walawender, W., Fan, L.T., Chang, C.C., "Mathematical Model for the Fluid-Bed Gasification of Biomass Materials. Application to Feedlot Manure" *Industrial and Engineering Chemistry - Process Design and Development* (20) (1981) 686-692.

Raizada, N., Sonakya, V., Anand, V., "Waste Management and Production of Future Fuels", Journal of scientific & industrial research (61) (3) (2002) 184-207.

Ranzi, E., Cuoci, A., Faravelli, T., Frassoldati, A., Migliavacca, G., Pierucci, S., Sommariva, S., "Chemical Kinetics of Biomass Pyrolysis", *Energy & Fuels* (22) (2008) 4292-4300.

Rensfelt, E., Blomkvist, G., Ekstrom, C., Enstrom, S., Espenas, B.G., Linanki, L., "Basic Gasification Studies for Development of Biomass Medium-BTU Gasification Processes", *Energy from Biomass and Wastes* Symposium Paper (1978).

Rhie, C.M., Chow, W.L., "Numerical Study of the Turbulent Flow Past an Airfoil with Trailing Edge Separation", *AIAA J*. (21) (11) (1983) 1525-1532.

Ross, D.P., Yan, H., Zhong, Z., Zhang, D., "A Non-Isothermal Model of a Bubbling Fluidized-Bed Coal Gasifier", *Fuel* (84) (2005) 1469-1481.

Ruggiero, M. Manfrida, G., "An Equilibrium Model for Biomass Gasification Processes", *Renewable Energy* (16) (1999) 1106-1109.

Shin, Donghoon, Choi, Sangmin, "The Combustion of Simulated Waste Particles in a Fixed Bed", *Combustion and Flame* (121) (2000) 167-180.

Shires, G.L., "Recent Developments in Gas Producers", *Chemical Engineering and Mining Review* (50) (1958) 41-47.

Siminski, V.J., Wright, F.J., Edelman, R.B., Economos, C., Fortune, O.F., "Research on Methods of Improving the Combustion Characteristics of Liquid Hydrocarbon Fuels", *Report AFAPLTR* (1-2) (1972).

Singh, C.P.P., Saraf, D.N., "Simulation of High-Temperature Water-Gas Shift Reactors", *Ind. Eng. Chem., Process Design and Development* (16) (3) (1977) 313-319.

Soltes, E.J. "Problems and Opportunities in the Use of Wood and Related Residues for Energy in Texas", *A report to the Texas House subcommittee on alternate sources of Energy for Agriculture* (1978)13-14.

Spalding, D.B., "Mixing and Chemical Reaction in Steady Confined Turbulent Flames", *13th Int. Symp. on Combustion* (13) (1) (1971) 649-657.

Spalding, D.B., "A Novel Finite-Difference Formulation for Differential Expressions Involving Both First and Second Derivatives", *Int. J. Num. Methods Eng*. (4) (4) (1972) 551-559.

Spearpoint, M.J., Quintiere, J.G., "Predicting the Burning of Wood Using an Integral Model", *Combustion and Flame* (123) (3) (2000) 308-325.

Spurr, S.H., Vaux, H.J., "Timber: biological and economic potential", *Science* (191) (1976) 752-756.

Sreekanth, M., Kolar, A.K., "Mass Loss and Apparent Kinetics of a Thermally Thick Wood Particle Devolatilizing in a Bubbling Fludized Bed Combsutor", *Fuel* (89) (2010) 1050-1055.

Staggs, J. E. J., "A Simple Model of Polymer Pyrolysis Including Transport of Volatiles", *Fire Safety Journal* (34) (2000) 69-80.

Staggs, J. E. J., "Heat and Mass Tranport in Developing Chars", *Polymer Degradation and Stability* (82) (2003) 297-307.

Stern, E.W,, Logiudice, A.S., Heinemann, H., "Approach to Direct Gasification of Cellulosics", *Industrial And Engineering Chemistry - Process Design and Development* (4) (1965) 171-173.

Tewfik, S. R., "Biomass Utilization Facilities and Biomass Processing Technologies", *Energy Education Science and Technology* (14) (1/2) (2004) 1-19.

Traustel, S., "Calculation of Gasification Equilibria by Solution of Two Equations with Two Unknown Quantities" *Verein Deutscher Ingenieure* (88) (1944) 688-690.

Tsai, C.Y., Im, H. G., "A Computational Model for Pyrolysis, Gasification and Heat Transfer in an RDF Fixed-Bed Gasifier", *2007 ASME International Mechanical Engineering Congress and Exposition*, *Seattle, Washington*, (2007) 11-15.

Tsai, C.Y., Im, H.G., Kim, T.Y., Kim, J. H., "Numerical Studies for Pyrolysis, Gasification and Heat Transfer in an RDF Fixed-Beded Gasifier under Non-Premixed Conditions", 2008 *International Symposium on Advances in Computational Heat Transfer*, *Marrakech, Morocco*, (2008) 11-16.

Tsai, C.Y., Im, H.G., Kim, T.Y., Kim, J.H., "Computational Modeling of Pyrolysis and Combustion in a Fixed-Bed Waste Gasifier", *Int. J. of Numerical Methods for Heat Fluid Flows in progress* (2010).

U.S. Energy Information Administration, Office of Coal, Nuclear, Electric and Alternate Fuels, U.S. Department of Energy, "Renewable Energy Trends in Consumption and Electricity 2008", August 2010

Van Swaaij, W.P.M., "Gasification - The Process and the Technology", *Resources and Conversion* (7) (1981) 337-349.

Voigt, J. "Influence of Moisture upon the Working of Gas Producers", *Elektrotechnik und Maschinenbau* (1909) 1019-1020.

Wakao, N., Tanaka, K., Nagai, H., "Measurements of particle-to-gas mass transfer coefficients from chromatographic adsorption experiments", *Chem. Engng. Sci.* (31) (1976) 1109-1113.

Wakao, N., Kaguei, S., Heat and Mass Transfer in Packed Beds, *Gordon and Breach Science* (1982).

Wen, C.Y., "Non-Catalytic Heterogeneous Solid Fluid Reaction Models", *Ind. Eng. Chem.* (60) (1968) 9-34.

Wen, C.Y., Chaung T.Z., "Entrainment Coal Gasification Modeling", *Ind. Eng. Chem. Process Design and Development* (18) (1979) 684-695.

Whitaker, S., "Diffusion and Dispersion in Porous Media", *AICh. J.* (13) (1967) 420-427.

Wolff, "Gasification of Low Calorific Combustibles." *American Gas Journal* (118) (1923) 246-250.

Wolfshtein, M.W., "The Velocity and Temperature Distribution in One Dimensional Flow with Turbulence Augmentation and Pressure Gradient", *Int. J. Heat & Mass Transfer* (12) (3) (1969) 301-318.

Zahradnik, R.L., Grace, R.J., Chemistry and Physics of Entrained Coal Gasification, *Advances in Chemistry, American Chemical Society* (1974) 126-144.

Zeng, W.R., Li, S.F., Chow, W.K., “Review on Chemical Reactions of Burning Poly(methyl methacrylate) PMMA”, *J. Fire Science* (20) (2002) 401-433.